

UNIVERSIDADE FEDERAL DE JUIZ DE FORA  
FACULDADE DE ENGENHARIA  
PROGRAMA DE PÓS-GRADUAÇÃO EM MODELAGEM  
COMPUTACIONAL

Gustavo Montes Novaes

Multiscale Modelling for the Calcium Dynamics in Cardiac Electrophysiology

Juiz de Fora  
2023

**Gustavo Montes Novaes**

**Multiscale Modelling for the Calcium Dynamics in Cardiac Electrophysiology**

Tese apresentada ao Programa de Pós-Graduação em Modelagem Computacional da Universidade Federal de Juiz de Fora como requisito parcial à obtenção do título de Doutor em Modelagem Computacional. Área de concentração: Modelagem Computacional.

Orientador: Prof D.Sc. Rodrigo Weber dos Santos

Coorientador: Prof Ph.D Enric Alvarez-Lacalle

Coorientador: Prof Ph.D Sergio Alonso Muñoz

Juiz de Fora

2023

Ficha catalográfica elaborada através do Modelo Latex do CDC da UFJF  
com os dados fornecidos pelo(a) autor(a)

Novaes, Gustavo Montes.

Multiscale Modelling for the Calcium Dynamics in Cardiac Electrophysiology / Gustavo Montes Novaes. – 2023.

141 f. : il.

Orientador: Rodrigo Weber dos Santos

Coorientador: Enric Alvarez-Lacalle

Coorientador: Sergio Alonso Muñoz

Tese (Doutorado) – Universidade Federal de Juiz de Fora, Faculdade de Engenharia. Programa de Pós-Graduação em Modelagem Computacional, 2023.

1. Cardiac Modeling.
  2. Calcium Dynamics .
  3. Multiscale.
- I. Santos, Rodrigo Weber dos Santos, orient.  
II. Alvarez-Lacalle, Enric, coorient., III.  
Muñoz, Sergio Alonso, coorient.  
IV, Título.

**Gustavo Montes Novaes**

**Multiscale Modelling for the Calcium Dynamics in Cardiac Electrophysiology**

Tese apresentada ao Programa de Pós-Graduação em Modelagem Computacional da Universidade Federal de Juiz de Fora como requisito parcial à obtenção do título de Doutor em Modelagem Computacional. Área de concentração: Modelagem Computacional.

Aprovada em 11 de setembro de 2023

**BANCA EXAMINADORA**

---

Prof D.Sc. Rodrigo Weber dos Santos - Orientador  
Universidade Federal de Juiz de Fora

---

Prof Ph.D Enric Alvarez-Lacalle - Coorientador  
Universitat Politècnica de Catalunya

---

Prof Ph.D Sergio Alonso Muñoz - Coorientador  
Universitat Politècnica de Catalunya

---

Prof D.Sc. Bernardo Martins Rocha  
Universidade Federal de Juiz de Fora

---

Prof D.Sc. Marcelo Lobosco  
Universidade Federal de Juiz de Fora

---

Prof Ph.D Blas Echebarría Domínguez  
Universitat Politècnica de Catalunya

---

Prof Ph.D Fernando Otaviano Campos  
King's College London

## AGRADECIMENTOS

Em primeiro lugar, eu agradeço a Deus pela oportunidade de passar por esta etapa tão desafiadora, mas igualmente enriquecedora. A ele, agradeço tambem a saúde física e mental que nunca me faltaram durante todo este longo período.

Em seguida, agradeço à minha família. Nesta, agradeço em primeiro lugar a meu filho, Davi. Depois de seu nascimento você me ensinou na prática o real valor de cada coisa. Desde então, eu te agradeço por me receber do trabalho, todos os dias, de braços abertos em busca de um abraço. Estes momentos são os melhores do meu dia. Agradeço também à minha esposa Carla. Obrigado por ser, desde sempre, o alicerce da nossa família. Obrigado por cuidar da casa, do filho, e até de mim quando eu não conseguia eu mesmo o fazer. Meu muito obrigado à minha mãe, Bernadete. Muito obrigado por ainda hoje ser meu porto seguro. Obrigado pelo apoio enquanto eu estava fora, obrigado pelas incontáveis vezes em que cuidou do Davi para que pudesse me dedicar a este estudo.

Muito obrigado aos meus orientadores. Certamente, sem o apoio, dedicação, disponibilidade e paciência de vocês ao longo de todos esses anos, eu não conseguiria concluir esta etapa. Um muito obrigado aos professores Enric e Sergio por me receberem de forma tão gentil em sua instituição. Aliás, obrigado à Universitat Politècnica de Catalunya (UPC), em especial à Escola Politècnica Superior d'Edificació de Barcelona (EPSEB), por abrir suas portas e me receber como um de seus alunos pelo período que lá estive. Um muito obrigado ao professor Rodrigo pelos 13 anos de parceria. Obrigado pelo ensinamento e amizade por todos estes anos. Certamente você fez eu chegar a lugares que não sabia que conseguiria. Um muito obrigado à Universidade Federal de Juiz de Fora e, em especial, ao Programa de Pós-Graduação em Modelagem Computacional. Foram grandes momentos vividos dentro deste prédio azul. Muito obrigado à Coordenação de Aperfeiçoamento de Pessoal de Nível Superior (CAPES) por fomentar o período em que passei desenvolvendo parte deste estudo na UPC. Obrigado ao Centro Federal de Educação Tecnológica de Minas Gerais (CEFET-MG) por me liberar de minhas atividades acadêmicas para que eu pudesse me dedicar exclusivamente a este estudo.

Por fim, mas não menos importante, muito obrigado à minha *coach* de doutorado, prof. Evelyn Aparecida de Oliveira. Amiga, muito obrigado por estar presente mesmo distante. Você sabe como a nossa amizade é especial para mim. Muito obrigado por estar ao meu lado nesta etapa tão desafiadora, principalmente nos últimos dias rsrs.

“The important thing is not to stop questioning.” - Albert Einstein

## RESUMO

Segundo a Organização Mundial da Saúde, as duas principais causas de morte no mundo estão relacionadas a doenças cardíacas. Um componente crítico para que as células cardíacas desempenhem sua função primária, bombear o sangue, é a regulação da concentração intracelular de cálcio. O íon cálcio é o elemento chave na contratilidade das células cardíacas e sua dinâmica intracelular envolve diversas atividades físico-química. Todo o processo é denominado processo de Liberação de Cálcio Induzida por Cálcio (CICR). As atividades que compõem o processo CICR são de alta complexidade e envolvem fenômenos espaciais e temporais em multiescala. Dessa forma, um modelo computacional capaz de reproduzir esse processo crucial para o correto funcionamento do coração nessas diferentes escalas poderá contribuir para a compreensão da relação entre as atividades em microescala e os efeitos que elas causam no comportamento de todo o órgão. Assim, esta tese propõe um novo modelo computacional espaço-temporal para o miócito do ventrículo esquerdo humano capaz de reproduzir a estocasticidade presente na natureza microescala da célula e determinar os efeitos desses fenômenos locais no comportamento celular em macroescala. O desenvolvimento deste modelo multiescala foi baseado em um modelo celular consolidado. Este modelo base foi modificado incorporando Variáveis Aleatórias em sua formulação. Isso permitiu que a versão atualizada do modelo replicasse fenômenos que ocorrem em nível subcelular, como o comportamento estocástico de canais iônicos e liberações espontâneas de cálcio. Além disso, a característica multiescala do modelo foi implementado através da introdução de dois parâmetros nas formulações do CICR que permitem a utilização do modelo para reproduzir os resultados em escalas subcelulares e celulares. O modelo proposto apresentou resultados satisfatórios. Simulados sob a condição de microescala, o modelo foi capaz de reproduzir as liberações espontâneas de cálcio enquanto que, sob uma visão de macroescala, reproduziu também os resultados determinísticos esperados. Além disso, este novo modelo poderá possibilitar novos estudos na compreensão de patologias cardíacas e sua associação com as estruturas subcelulares.

Palavras-chave: Modelagem Cardíaca. Dinâmica de Cálcio. Multiescala.

## ABSTRACT

According to the World Health Organization, the top two death causes worldwide are related to cardiac diseases. A critical component for the cardiac cells to perform its primary function, to pump the blood, is regulating the intracellular calcium concentration. The calcium ion is the key element in the cardiac cells' contractility, and its intracellular dynamics involve several physical and chemical activities. The whole process is named the Calcium-Induced Calcium Release (CICR) process. The activities composing the CICR process are of high-order complexity and involve spatial and temporal multiscale phenomena. In this way, a computational model capable of reproducing this crucial process for the correct cardiac function in these scales might contribute to understanding the relation between the micro scale activities and the effects they cause on a whole organ behavior. So, this thesis proposes a novel spatial-temporal computational model for the human left ventricle myocyte capable of reproducing the stochasticity present in the micro scale nature of the cell and determining the effects of these local phenomena in the macro scale cellular behavior. The development of this multiscale model was based on a well-accepted cellular model. This base model was modified by incorporating Random Variables in its formulation. It enabled the updated version of the model to replicate phenomena occurring at a subcellular level, such as the stochastic behavior of ionic channels and spontaneous calcium sparks. Besides, the multiscale feature was implemented by introducing two parameters in the CICR formulations that allow the usage of the model to reproduce the outputs in both subcellular and cellular scales. The proposed model presented satisfactory results. Simulated under the micro scale condition, the model were capable of reproducing the spontaneous calcium sparks while that, under a macro scale viewing, it reproduced the deterministic expected outputs. Furthermore, this new proposition might enable further studies in understanding heart pathologies and their association with the subcellular structure.

Keywords: Cardiac Modeling. Calcium Dynamics. Multiscale.

## LIST OF ILLUSTRATIONS

Figure 1 – Illustration of the human blood circulation system. . . . .	21
Figure 2 – Illustration of the different parts that compound the heart wall. . . . .	22
Figure 3 – Representative illustration of the cells specialized in the conductivity of the electrical pulse through the cardiac organ; these cells compose the Purkinje System. . . . .	23
Figure 4 – Schematic illustration of the different phases of an AP measured on the membrane of a cardiac cell. . . . .	24
Figure 5 – Ion channels function as pores to permit the flux of ions down their electrochemical potential gradient. . . . .	25
Figure 6 – Ion Channel composition and disposition. Illustration of the ion channels subunits $S_{\bullet}$ under a resting, or closed, condition (A) and under voltage-activated, or opened, condition (B). . . . .	26
Figure 7 – Structural composition of a skeletal or cardiac muscle. . . . .	29
Figure 8 – Two extreme states that a sarcomere can assume: relaxed (top) and contracted (bottom). . . . .	30
Figure 9 – Combination of many myosin molecules to form a myosin filament. Also shown are myosin cross-bridges and interaction between the heads of the cross-bridges with adjacent actin filaments. . . . .	30
Figure 10 – Actin Myofilament in detail to the tropomyosin filaments, active locals and the complex of troponin. . . . .	31
Figure 11 – The “walk-along” mechanism for contraction of the muscle. . . . .	31
Figure 12 – Calcium-Induced Calcium Release process. As soon as an Action Potential reaches the cell causing an depolarization, the L-Type Calcium Channels open and allow an influx on calcium ions inside the cell. These calcium ions interact with the Ryanodine Receptors changing their conformation and, thus, opening these structures. This opening allows a massive influx of calcium ions from the Sarcoplasmic Reticulum inside the cytoplasm, thus, generating cellular contraction. After that, the SERCA pump reuptake these calcium ions from the cytoplasm to the Sarcoplasmic Reticulum reestablishing the resting condition. . . . .	32
Figure 13 – Line scan confocal image of an Evoked Spark (ES) triggered by an Action Potention (AP) depolarization. . . . .	33
Figure 14 – Line scan confocal image of an Spontaneous Spark (SS). . . . .	34
Figure 15 – Simulation output generated by the Hodgkin and Huxley (29) model. In the left pane, the transmembrane potential (AP) is presented; in the right pane, it is presented the conductivities of the transmembrane ion currents $I_{Na}$ and $I_K$ . . . . .	35

Figure 16 – Hodgkin and Huxley (29) model representations. Left panel presents a schematic representation of the model (obtained from CellML (14)); right panel presents an equivalent electric circuit. . . . .	36
Figure 17 – Schematic representation for Hodgkin and Huxley (29) Gate model. . .	37
Figure 18 – Schematic representation of the biological structures considered in ten Tusscher et al. (61) model. . . . .	39
Figure 19 – Graphic representation of the results obtained by the ten Tusscher et al. (61) model. . . . .	40
Figure 20 – Schematic representation of the ten Tusscher and Panfilov (62) Model. . .	41
Figure 21 – Schematic representation of the structures that compose the intracellular calcium dynamics implemented by ten Tusscher and Panfilov (62). . . .	42
Figure 22 – Graphic representation of the results obtained by the ten Tusscher and Panfilov (62) model. . . . .	43
Figure 23 – $I_{CaL}$ gates dynamics (left panel) in comparison with $I_{CaL}$ current (right panel) of the ten Tusscher and Panfilov (62) model. . . . .	44
Figure 24 – A schematic representation of the four-state Ryanodine Receptor Markov Chain model of Shannon et al. (54) and Stern et al. (57). . . . .	45
Figure 25 – Output dynamics generated by the simulation of the models Mahajan et al. (36) (MJ), and ten Tusscher and Panfilov (62) (TP). Left panel shows the $I_{CaL}$ Opening Fraction, $O_f$ ; right panel shows the $I_{CaL}$ current. . . . .	49
Figure 26 – Schematic representation of the novel MC-based ten Tusscher and Panfilov (62) Model (DTP) with the insertion of the MC-based $I_{CaL}$ model proposed by Mahajan et al. (36). . . . .	50
Figure 27 – Schematic representations of the three markov chain structures considered in this study. A: The four independent Markov Chains for each gate of the ten Tusscher and Panfilov (62) model considering only two possible states, Open ( $O$ ) and Close ( $C$ ) for each one. B: The original structure of the Markov Chain used by Mahajan et al. (36) to simulate the $I_{CaL}$ phenomenon. C: The DTP Markov Chain created as a combination of the Hodgkin and Huxley (29) formalism rates and the Mahajan et al. (36) topology, to replace the gates in the ten Tusscher and Panfilov (62) model. The MC transitions generated considering the Hodgkin and Huxley (29) gates $d$ , $f$ , and $f_2$ are shown respectively in blue, green, and yellow. The calcium-dependent function $f$ and the rates associated with the calcium concentration are shown in red. The set of parameters $\alpha$ used to fit both calcium-dependent rates (parameters $x_0$ to $x_4$ ) and voltage-dependence rates (parameters $x_5$ to $x_{10}$ ) are shown in black. . . . .	52

Figure 28 – Schematic representation of the novel MC-based ten Tusscher and Panfilov (62) Model highlighting, in red, the structures that compose a single CRU $u$ . . . . .	55
Figure 29 – Four-state Markov Chain used to represent the states that the RyR channels can assume. The state $I$ represents an Inactivated closed state, the state $R$ represents a Resting closed state, the state $RI$ represents a Resting Inactivated closed state, and the state $O$ represents the Open conducting state. . . . .	58
Figure 30 – Schematic representation a single CRU $u$ that compose the STP model. . . . .	61
Figure 31 – Illustrations of different NxN CRUs Grid conformations. . . . .	62
Figure 32 – Comparison between all 256 local $[Ca]_{i\text{ free}}^u$ traces (black lines) alongside the global $[Ca]_{i\text{ free}}$ (red line). . . . .	64
Figure 33 – Illustration of the three different diffusion conditions considered in the NxN CRUs grid simulations. (A) No-Diffusion Condition ( $D_0$ ). Each CRU $u$ has local values for $[Ca]_{i\text{ free}}^u$ and $[Ca]_{SR\text{ free}}^u$ . Furthermore, the local dynamics influence only the local CRU. (B) Realistic Diffusion Condition ( $D_R$ ). Each CRU $u$ has local values for $[Ca]_{i\text{ free}}^u$ and $[Ca]_{SR\text{ free}}^u$ . However, the local dynamics influence the local CRU and its adjacent. (C) Infinite Diffusion Condition ( $D_\infty$ ). Each CRU $u$ share the one single global values for $[Ca]_{i\text{ free}}$ and $[Ca]_{SR\text{ free}}$ . So, the local dynamics influence instantly all the CRU grid. . . . .	69
Figure 34 – Stimulation protocol used in the 16x16 CRUs grid simulations. The protocol is composed by three phases $P_1$ (black area), $P_2$ (blue area) and $P_3$ (red area). . . . .	70
Figure 35 – Outputs generated by the population of solutions $P_{TP}$ . Traces obtained using the best solution of the population $P_{TP}$ , $x_{TP}^b$ (dashed blue line), alongside the traces obtained using the other solutions that compose the population (light blue lines) compared with the original ten Tusscher and Panfilov (62) model (black line). A: Opening fraction, $O_f$ . B: $I_{CaL}$ current. C: Action Potential. D: Intracellular Calcium concentration, $[Ca]_i$ . . . . .	74
Figure 36 – Descriptive Measures of the stochastic metric $S$ . The results present the outputs of STP model varying the $N_{LCC}$ as $N_{LCC} = \{2^i   i \in \mathbb{I} \text{ and } i = 0 - 15\}$ and using $N_{RyR} = 5 \times N_{LCC}$ . For each $N_{LCC}$ and, consequently, $N_{RyR}$ , there were generated $n = 100$ outputs. In contrast, there are presented also the $S$ values for the DTP model. . . . .	76
Figure 37 – Standard Deviation $\sigma(\bar{S})$ obtained from the set of $n = 100$ $S$ values calculated for each respective value assumed by $N_{LCC}$ as $N_{LCC} = \{2^i   i \in \mathbb{I} \text{ and } i = 0 - 15\}$ and using $N_{RyR} = 5 \times N_{LCC}$ . For each $N_{LCC}$ and, consequently, $N_{RyR}$ , they were generated $n = 100$ outputs. . . . .	77

- Figure 38 – Output curves of the AP,  $[Ca]_{i\text{free}}$ ,  $I_{CaL}$  and  $I_{rel}$ . The results present the outputs of the STP model varying the  $N_{LCC}$  as  $N_{LCC} = \{1, 32, 1024, 32768\}$  and using  $N_{RyR} = 5 \times N_{LCC}$ . For each  $N_{LCC}$  and, consequently,  $N_{RyR}$ , there are presented  $n = 100$  samples. In contrast, there are presented also the output values for the DTP model (black line). . . . . 78
- Figure 39 – Output curves of the AP,  $[Ca]_{i\text{free}}$ ,  $I_{CaL}$  and  $I_{rel}$ . The results present the outputs of the NxN CRUs STP model varying the N as  $N = \{1, 2, 4, 8, 16\}$ . For all cases, the global value for the  $N_{LCC}$  and  $N_{RyR}$  were  $N_{LCC} = 1024$  and  $N_{RyR} = 5N_{LCC} = 5120$ . For each N there are presented  $n = 50$  samples. In contrast, there are presented also the output traces from the DTP model (black line). . . . . 81
- Figure 40 – Descriptive Measures of the peak values of the  $I_{rel}$  current obtained by the simulation of the spatial STP model in the five conformations: 1x1, 2x2, 4x4, 8x8, 16x16. For each conformation, there were generated  $n = 50$  samples. 82
- Figure 41 – Descriptive Measures of the peak values of the  $[Ca]_{i\text{free}}$  concentration obtained by the simulation of the spatial STP model in the five conformations: 1x1, 2x2, 4x4, 8x8, 16x16. For each conformation, there were generated  $n = 50$  samples. . . . . 83
- Figure 42 – Total number of Sparks obtained by each realization of the 16x16 STP model stimulated at 1Hz by ten seconds. . . . . 84
- Figure 43 – Distribution of the occurrence of all calcium Sparks encountered by the five realizations of the 16x16 STP model simulated at a 1Hz pacing rate over the whole CRU grid. . . . . 85
- Figure 44 – Traces of the  $[Ca]_{i\text{free}}^u$ ,  $I_{CaL}^u$ , and  $I_{rel}^u$  variables obtained by one CRU  $u$  that compose the 16x16 CRU grid of the STP model simulated under 1Hz stimulation. In this BC sample, it can be seen both the Evoked and the Spontaneous calcium Sparks. The first one is Evoked since it occurs during the active phase of the cell. In this phase, the LCCs may still be active and allow calcium influx inside the cell. As can be noticed in  $I_{CaL}^u$  current, panel B, this first Spark was preliminary triggered due to the LCC opening. The activation of the RyR was not so expressive (panel C). The second calcium Spark was different. As can be seen in panel B, the LCCs remained completely inactive. The occurrence of the Spark was exclusively due to the RyR randomness; hence, it was Spontaneous. . . . . 86
- Figure 45 – Sequence of distinct moments of the dynamics of the local variables  $[Ca]_{i\text{free}}^u (\mu M)$  over 450ms after the stimulation. The Panels were chronologically organized where Panel A represents the moment  $t = 0ms$ , Panel B represents the moment  $t = 50ms$ , Panel C represents the moment  $t = 100ms$ , up to Panel J that represents the moment  $t = 450ms$ . . . . . 87



Figure 56 – Output curves of the AP,  $[Ca]_{i,free}$ ,  $I_{CaL}$  and  $I_{rel}$ . The results present the outputs of the 16x16 STP model with the implementation of the calcium diffusion on the  $\bullet_{ss}$  medium (panels A-D); and considering the implementation of the diffusion in the space (panel E-F). For each N there are presented  $n = 50$  samples. In contrast, there are presented also the output traces from the DTP model (black line) . . . . . 98

Figure 57 – Linescan-type image of an arbitrary row of the 16x16 CRU grid obtained by simulating of the STP model considering the diffusion in the  $\bullet_{ss}$  medium. The outputs were obtained by defining  $D_{ss} = D_i = 0.4\mu m^2/ms$  and a pacing rate of 1Hz . . . . . 99

Figure 58 – Schematic representations of the three markov chain structures considered in this study. A: The four independent Markov Chains for each gate of the models TP considering only two possible states, Open ( $O$ ) and Close ( $C$ ) for each one. B: The original structure of the Markov Chain used by MJ to simulate the  $I_{CaL}$  phenomenon. C: The proposed Markov Chain as a combination of the HH formalism rates and the MJ topology, to replace the gates in the TP model. The MC transitions generated considering the HH gates  $d$ ,  $f$ , and  $f_2$  are shown respectively in blue, green, and yellow. The calcium-dependent function  $f$  and the rates associated with the calcium concentration are shown in red. The set of parameters  $\boldsymbol{x}$  used to fit both calcium-dependent rates (parameters  $x_0$  to  $x_4$ ) and voltage-dependence rates (parameters  $x_5$  to  $x_{10}$ ) are shown in black. . . . . 112

## LIST OF TABLES

Table 1 – Structures of the MC-based version of the ten Tusscher and Panfilov (62) model that compose a single CRU $u$ .	55
Table 2 – Features for the AP and $[Ca]_i$ traces of the best solutions obtained by DE execution.	75
Table 3 – Formulations of the DTP markov-chain rates.	114

## LIST OF ABBREVIATIONS AND ACRONYMS

AP	Action Potential
BC	Basic Cycle
BCL	Basic Cycle Length
CICR	Calcium Induced Calcium Release
CPU	Central Processing Unit
CRU	Calcium Release Unit
DE	Differential Evolution
DTP	Deterministic Version of the novel model proposed in this thesis
ES	Evoked Spark
HH	Hodgkin and Huxley
LCC	L-type Calcium Channel
MC	Markov Chain
MJ	Mahajan et al.
MPI	Message Passing Interface
ODE	Ordinary Differential Equation
PDE	Partial Differential Equation
RAM	Random Access Memory
RyR	Ryonondine Receptor
SERCA	Sarco/Endoplasmic Reticulum Calcium-ATPase
SR	Sarcoplasmic Reticulum
SS	Spontaneous Spark
STP	Stochastic version of the novel model proposed in this thesis
TP	Ten Tusscher and Panfilov
TT	Ten Tusscher et. al
WHO	World Health Organization

## SUMMARY

<b>1</b>	<b>INTRODUCTION</b>	<b>17</b>
1.1	Objectives	18
1.2	Text Organization	19
<b>2</b>	<b>LITERATURE REVIEW</b>	<b>20</b>
2.1	Cardiac Physiology	20
2.2	Cardiac Electrophysiology	22
<b>2.2.1</b>	Action Potential	22
<b>2.2.2</b>	Cellular Membrane	24
<b>2.2.3</b>	Ion Channels	25
<b>2.2.3.1</b>	L-Type Calcium Channels	26
<b>2.2.3.2</b>	Ryanodine Receptors	27
<b>2.2.4</b>	Calcium-Induced Calcium Release Process	28
2.3	Computational Modeling of The Cardiac Electrophysiology	34
<b>2.3.1</b>	Hodgkin and Huxley Model	34
<b>2.3.2</b>	Ten Tusscher et al. Model	39
<b>2.3.3</b>	Ten Tusscher and Panfilov Model	41
<b>2.3.3.1</b>	Ten Tusscher and Panfilov LCC Model	43
<b>2.3.3.2</b>	Ten Tusscher and Panfilov RyR Model	44
<b>2.3.4</b>	Deterministic X Stochastic Modeling	46
<b>3</b>	<b>METHODS</b>	<b>47</b>
3.1	MC-Based $I_{CaL}$ Version	48
<b>3.1.1</b>	DTP $I_{CaL}$ Formulation	50
<b>3.1.2</b>	DTP $I_{CaL}$ Fitting Procedure	53
<b>3.1.3</b>	Definition of a Calcium Release Unit in DTP Model	54
<b>3.1.4</b>	DTP Stochastic Version	57
<b>3.1.5</b>	Spatial Model Version	60
3.2	Simulation Experiments	66
<b>3.2.1</b>	1x1 CRU Computational Experiments	67
<b>3.2.2</b>	NxN CRUs Computational Experiments	68
<b>3.2.3</b>	Computational Implementation	71
<b>4</b>	<b>RESULTS</b>	<b>73</b>
4.1	DTP Model Fitting	73
4.2	Simulation Results	75
<b>4.2.1</b>	1x1 CRU Simulation Results	75
<b>4.2.2</b>	NxN CRUs Simulations Results	79
<b>4.2.2.1</b>	Micro vs Macro Scale Analysis	80
<b>4.2.2.2</b>	Calcium Sparks	83

5	DISCUSSIONS . . . . .	96
6	CONCLUSION . . . . .	102
	REFERENCES . . . . .	104
	APPENDIX A – Mathematical Formulation . . . . .	109
	APPENDIX B – DTP MC-Based $I_{CaL}$ Formulation . . . . .	112
	ANNEX A – DTP MC-Based $I_{CaL}$ - Complete Study . . . . .	115

## 1 INTRODUCTION

In 2020, the World Health Organization (WHO) updated the leading causes of death worldwide. According to the publication (1), the top two causes were ischemic heart disease and stroke. These two diseases were responsible for around 26 million deaths in 2019 and 2020. Also, according to the publication, the leading cause of death globally is responsible for 16% of all deaths. Over the past two decades, this disease has seen the largest increase in fatalities, with over 2 million additional deaths bringing the total to 8.9 million in 2019. So, given these challenging numbers, every study that contributes to understanding cardiac physiology and its different systems have a substantial impact.

Several scientific groups worldwide have contributed to understanding cardiac physiology via computational modeling (39, 27, 60). Computational models are widely used to study the mechanics of the cardiovascular system (50). These models help to understand its dynamics and quantify properties that are challenging or impossible to measure through experiments (58).

A critical component for the cardiac cells to perform its primary function, to pump the blood, is the regulation of the intracellular calcium concentration (28). The intracellular medium is composed of different ions, and each has its role in the correct functioning of the cell. The calcium ion is the key element in the cardiac cells' contractility (16, 5). The minimal presence of calcium ions in the cell's interior can trigger a massive loading of the same ion from the Sarcoplasmic Reticulum. This huge calcium concentration interacts with other cellular structures leading to the cell shortening. The whole process is named as Calcium-Induced Calcium Release (CICR) process (15).

Besides all the electrical and chemical complexities involved in the CICR process, one significant challenge in modeling the role of calcium ions within the process is the non-linear and multi-scale properties in space and time dimensions (18). The structures of L-type Calcium Channels (LCCs) and Ryonondine Receptors (RyR) are the main ones responsible for starting the CICR process. These two sorts of arrangements are at a subcellular level (nanometers) (7). Conversely, the CICR process have an important impact on the electrical (transmembranic potential) and mechanical (contractility) activities of the whole cell scale (micrometers) (17).

Over the last decade, there have been substantial advances in the complexity and sophistication of computational models for intracellular calcium dynamics. The most traditional myocyte models as, for instance Pandit et al. (45), ten Tusscher et al. (61), and O'Hara et al. (43), were created considering a coalescence of the whole spatial distribution of a myocyte into a single shared bulk. This approach is well-consolidated and accepted. Sato et al. (53) has shown that the variability in intracellular calcium cycling is crucial in understanding the occurrence of discordant alternans. So, in this way, this kind of study

cannot be simulated using deterministic models of shared bulk cells. In addition, Colman et al. (18) indicates that computational models that consider the spatial aspects of the cardiomyocyte and the stochastic behavior of RyRs and LCCs are more appropriate for detailed analysis of intracellular calcium dynamics. For more details of an overview of the multi-scale computational modeling of spatial calcium dynamics, see Colman et al. (18).

Given this context: the expressive positions of heart diseases as the leading causes of death in the world, the contribution that computational models can offer to the cardiac physiology field, the significance of the CICR process for the correct cardiac function, and the multi-scale nature of this process; this thesis proposes the development of a novel multi-scale computational model for human ventricular myocytes capable of reproducing experiments of the CICR process in both micro and macro scales.

With the development of this model, it is expected that it can be used especially in studies that investigate the link of the subcellular structures conformations as, for instance, the LCCs and RyRs, with the cellular level pathologies as, for example, cardiac alternans (65).

The development of the multi-scale model is based on the well-accepted model presented by ten Tusscher and Panfilov (62). This model was selected since, despite being formulated to reproduce human ventricle myocytes electrophysiology, it was widely tested and accepted for tissue simulations. In this way, its usage for the cellular and tissue level is already defined. This thesis aims to modify the original model by incorporating subcellular variables. This might enable the updated version of the model to replicate phenomena occurring at a subcellular level, such as the stochastic behavior of ionic channels and spontaneous calcium sparks.

### 1.1 Objectives

The main objective of the thesis is to propose a novel computational model for human ventricular myocytes capable of reproducing simulations of the CICR process at subcellular and cellular levels based on multi-scale parameters definition. For that, a few punctual objectives can be mentioned.

The first is to define a well-accepted computational model that simulates the human ventricle myocyte with explicit formulations for LCC and RyR structures. These specific formulations are suitable since these two structures are the leading actor in the CICR process. In possession of the base model, the next objective is to implement formulations based on Markov Chains in the LCC and RyR terms. This objective is a crucial step in the thesis development since at a subcellular level, these two structures must reproduce a stochastic behavior. Then, the next objective is to implement the stochastic feature into the model by replacing the deterministic Markov Chain formulations with a stochastic version composed of random variables. At last, in possession of the stochastic version of

the model, the next objective is to implement a spatial disposition of the LCCs and RyRs in a two-dimensional grid conformation to enable the analysis of the calcium diffusion on the whole cell.

## 1.2 Text Organization

The thesis is structured as follows: Chapter 2 provides an overview of the key concepts related to the study, including a Literature Review that covers Cardiac Physiology and Computational Modeling in this area. Chapter 3 outlines the Methods that were used to achieve the primary objective of developing a new computational model that can replicate the human ventricle myocyte on a multiscale level. Chapter 4 and Chapter 6 present the Results and Conclusions, respectively. In addition to the main content, there is also an Appendix A that provides detailed information on the new computational model, and Annex A contains a previously published study that discusses some of the methods and findings related to the proposed model.

## 2 LITERATURE REVIEW

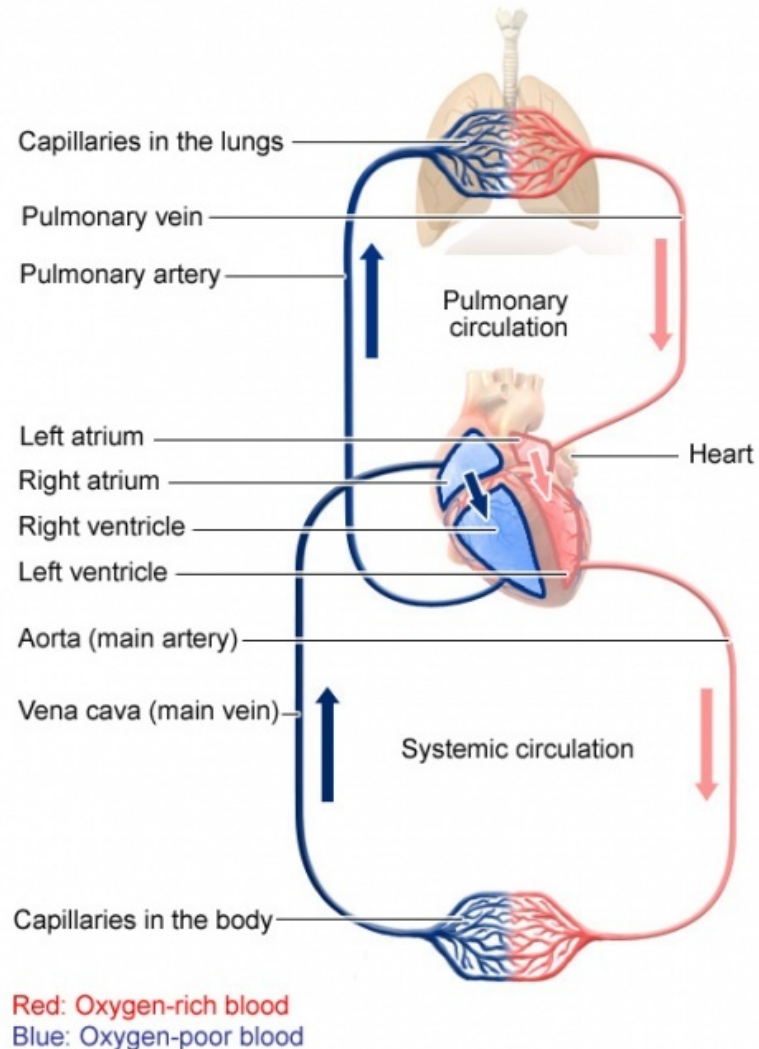
In this Chapter, it is presented the main concepts studied during the development of this thesis. References Hall (26) and Keener and Sneyd (34) were the primary references reviewed to conceive the concepts presented in this section.

### 2.1 Cardiac Physiology

All cells of the body need nutrients to perform their activities properly. The bloodstream is the leading actor in this way since it takes these nutrients to the cells. In this process, the heart is essential for maintaining bodily activities because it pumps blood through the veins and arteries so that it circulates throughout the body.

The human heart can be divided into two halves, left and right, and each has two chambers: the atrium, where the blood enters the organ, and the ventricle, responsible for the ejection of the blood out of the heart. In each cardiac cycle, the blood arriving in the heart from the body (venous blood) is directed to the lungs, where a process named Hematosis occurs (gas exchange between the pulmonary alveolus and the blood). Two critical activities must occur in this process: the release of  $\text{CO}_2$  from the blood and the uptake of  $\text{O}_2$  originating from the inspiring move. Then, this blood, now rich in  $\text{O}_2$ , is directed to the left half of the heart and pumped again to the body. Figure 1 illustrates this activity.

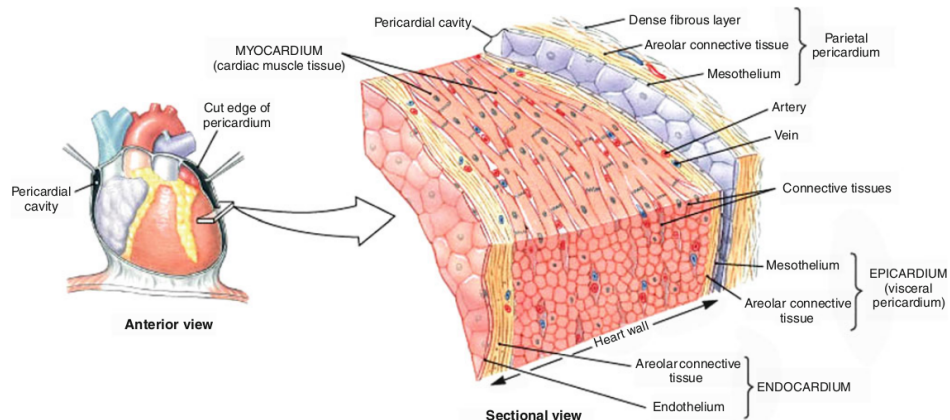
Figure 1 – Illustration of the human blood circulation system.



Source: obtained from Institute for Quality and Efficiency in Health Care (31).

Another important point of cardiac physiology is heart wall heterogeneity. If observed more detail, the heart wall can be divided into three main regions: epicardium, myocardium, and endocardium. Each of these regions has properties regarding, for instance, mechanical and electrical activities. Figure 2 shows an illustration of these regions.

Figure 2 – Illustration of the different parts that compound the heart wall.



Source: obtained from Weinhaus (64).

## 2.2 Cardiac Electrophysiology

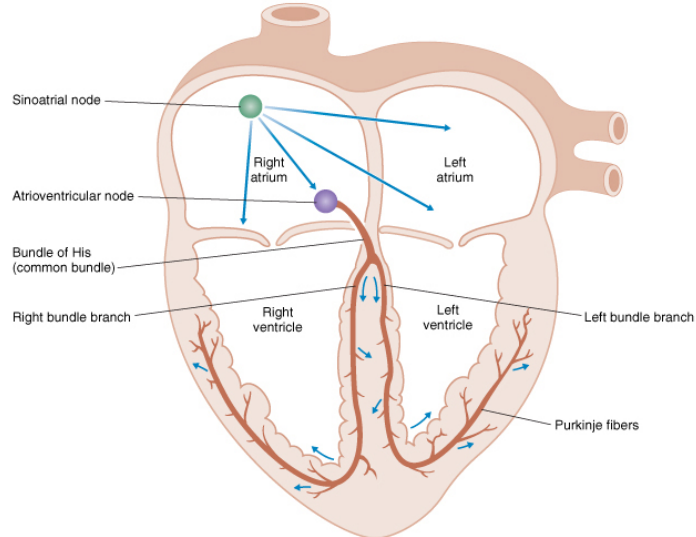
The heart is a complex organ, and several phenomena are involved in a single cardiac beat cycle. Moreover, the cardiac cells, the myocytes, have activities of different natures, such as chemical, mechanical, and electrical activities. As this thesis focuses on a specific part of the electrical activity of the human myocyte, the calcium cycle, this Section presents the main concepts associated with the Cardiac Electrophysiology regarded in this thesis.

### 2.2.1 Action Potential

An electrical discharge in the heart cells precedes each heart muscle contraction. This electric shock causes the contraction of these cells, and as this wave propagates by the organ, it contracts as a whole. This electrical discharge, called Action Potential (AP), is generated in a region known as the Sinoatrial or sinus node. For the AP to be rapidly spread throughout the heart, there are cells specialized in conducting this electrical wave. These cells comprise a rapid propagation pathway called the Purkinje System, which leaves the sinoatrial node passing through the atria and reaching the ventricles. As a result, an AP spreads throughout the organ, functioning as a message, so the cells contract synchronously. This synchronism of the contractions between the atria and ventricles is vital so that the blood pumping occurs correctly. To generate this synchrony, the atria, and ventricles are separated by a particular set of cells known as the Atrioventricular node. Considering the Purkinje System, this node is the only electrical connection between the atria and the ventricles. In this way, it generates an essential delay in the conduction of AP between the atria and the ventricles. This delay is responsible for synchronizing that atria pump blood to the ventricles before ventricular contraction. Figure 3 illustrates the

arrangement of cells specialized in conducting AP.

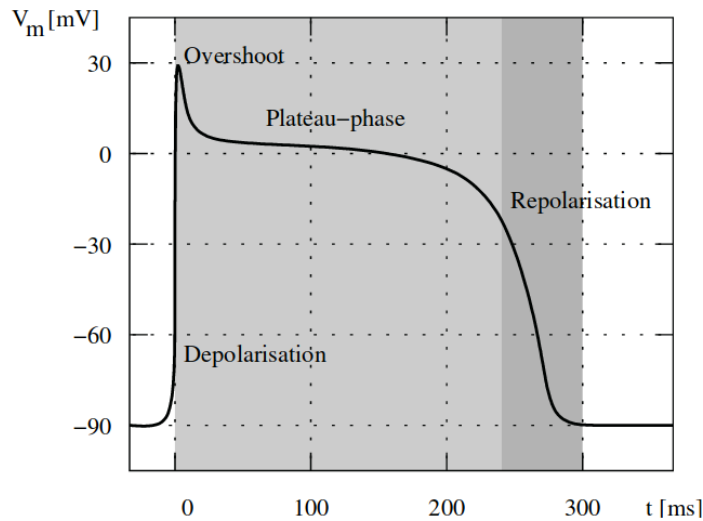
Figure 3 – Representative illustration of the cells specialized in the conductivity of the electrical pulse through the cardiac organ; these cells compose the Purkinje System.



Source: Universidade Federal de Juiz de Fora (2012).

In an AP, it is possible to observe four successive steps. The first is the resting stage, where the cell is relaxed, and the membrane potential is negative due to the significant ion concentration differences between the intracellular and extracellular media. The next phase is depolarization. This step occurs when the membrane suddenly becomes significantly permeable to sodium ions and allows the diffusion of many ions into the cell, thus raising the transmembrane potential. In the repolarization phase, the sodium channels begin to inactivate while the potassium channels open. The rapid diffusion of potassium towards the extracellular environment reestablishes the equilibrium potential of the membrane. However, this potassium flow through the ion channels can decrease the potential for values smaller than the rest, and in these cases, there is also the hyperpolarization phase. Figure 4 shows the graphical representation of an AP.

Figure 4 – Schematic illustration of the different phases of an AP measured on the membrane of a cardiac cell.



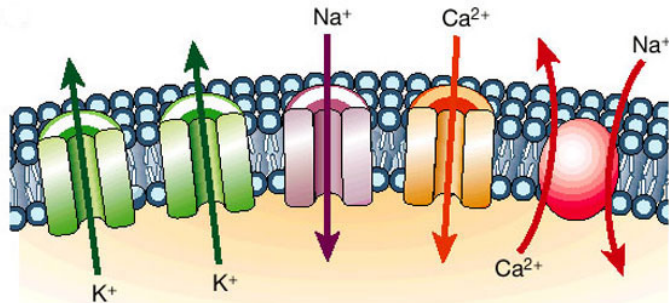
Source: adapted from Sachse (52).

### 2.2.2 Cellular Membrane

All cells have a membrane that operates as a barrier separating the intracellular and extracellular mediums. This membrane is called the cell membrane and is formed by a phospholipid bilayer containing two hydrophobic tails and a hydrophilic head, which, in an aqueous medium, forces the tails to align inward.

The cell membrane comprises some proteins with special arrangements forming a passageway between the intra and extracellular media. These proteins constitute the ion channels. The primary function of the ion channels is to allow the passing of specific ions into or out of the cell. A cardiac myocyte's intracellular and extracellular media are composed of an aqueous solution of salts where ions of  $\text{Na}^+$ ,  $\text{K}^+$ ,  $\text{Cl}^-$ , and  $\text{Ca}^{2+}$  are present. Figure 5 shows the schematic view of a cell membrane and the units that make it up.

Figure 5 – Ion channels function as pores to permit the flux of ions down their electrochemical potential gradient.



Source: obtained from Rasband (51)).

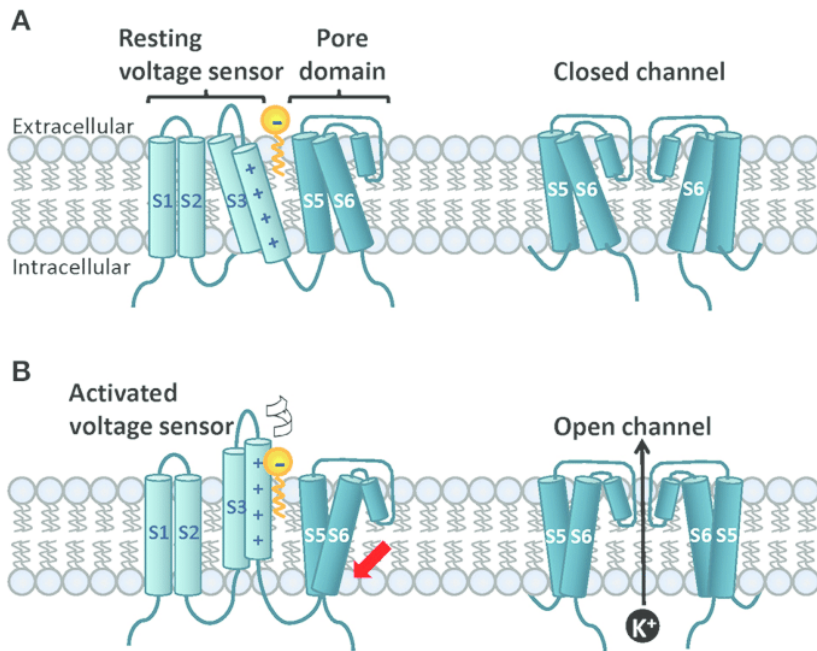
Each ion channel is specialized in allowing the passage of only one or a group of substances. The chemical and electrical composition difference inside and outside the cell generates an electrical differential called the transmembrane differential in the membrane. This differential has a fundamental role in the propagation of an action potential.

### 2.2.3 Ion Channels

As introduced in Section 2.2.2, Ion Channels are membrane proteins that regulate the flow of ions into and out of the cell. Considering the myocyte intracellular and extracellular medium, the ions  $\text{Na}^+$ ,  $\text{K}^+$ ,  $\text{Cl}^-$ , and  $\text{Ca}^{2+}$  are the most relevant ions, each with specific contributions to the correct function of the cardiac cell.

Each Ion Channel comprises one or more subunits that form a pore through the cell membrane. These subunits determine the channel's ion selectivity, gating, and modulation. Sodium channels, for example, are composed of a sizable  $\alpha$  subunit and one or more  $\beta$  subunits. The  $\alpha$  subunit contains the ion pore and the voltage sensor, while the beta subunits modulate channel function and regulate the cell surface expression of the channel. On the other hand, Calcium channels are composed of several subunits, including the  $\alpha_1$  subunit that contains the ion pore and the voltage sensor and accessory subunits that modulate the channel function and cell surface expression. In addition, each ion channel subunit has a unique amino acid sequence and contributes to the overall function of the channel. Therefore, mutations in ion channel subunits can alter channel function and lead to various diseases affecting muscle function. Figure 6 illustrates an ion channel and its subunits.

Figure 6 – Ion Channel composition and disposition. Illustration of the ion channels subunits  $S_{\bullet}$  under a resting, or closed, condition (A) and under voltage-activated, or opened, condition (B).



Source: obtained from Moreno et al. (37).

A remarkable characteristic of an ion channel, especially regarding this thesis purpose, is that an individual channel opening, or closing, is often described as a stochastic process because it is unpredictable and subject to random fluctuations. This stochasticity can result in oscillations in the ion current flowing through the channel, even without changes in membrane potential or other stimuli.

The stochastic nature of ion channel gating can play a role in several physiological processes, including generating action potentials, synaptic transmission, and sensory perception. For example, the stochastic opening and closing of ion channels in nerve cells can lead to fluctuations in the synaptic current, which can contribute to the variability of synaptic transmission and affect the strength of the synaptic connection.

In addition, the stochasticity of ion channel gating can also play a role in disease states. For example, mutations in ion channel subunits can alter the stochasticity of ion channel gating, leading to abnormal ion currents and contributing to the development of various diseases affecting muscle function (49, 21).

#### 2.2.3.1 L-Type Calcium Channels

Among the range of ions that compose the cellular dynamics and cardiac contractility, the calcium ion,  $Ca^{2+}$ , is the actor responsible for modifying the morphological

conformation of the cell structures responsible for muscle contraction: the sarcomeres.

L-Type Calcium Channels (LCCs) are unique among calcium channels in their ability to produce a sustained influx of calcium ions into the cell. This sustained influx is essential for maintaining a solid and prolonged contraction. In addition, LCCs have been the subject of extensive cardiovascular physiology studies. As a result, they are considered important therapeutic targets for treating various cardiovascular disorders, including heart failure, arrhythmias, and hypertension.

The LCCs activation is directly associated with the transmembrane potential. So, the LCCs are voltage-sensitivity. However, besides the inactivation due to the transmembrane potential, the LCCs also inactivate due to their calcium sensitivity. In other words, when the LCCs are activated by transmembrane potential depolarization, they allow the influx of calcium ions into the cell, which increases the intracellular calcium concentration. This increase in intracellular calcium provides feedback to regulate the opening and closing of these channels. For example, an increase in intracellular calcium concentration can cause the channels to inactivate more quickly, limiting the extent of calcium influx and, thus, muscle contraction.

The intracellular calcium dynamic is vital for the correct contraction of the cardiac cells and, thus, the blood pumping. Regarding this process, LCCs are the first structures responsible for triggering these cyclical dynamics and, thus, the cellular contraction.

As previously stated, the LCCs are the structures responsible for starting the cell contraction since the calcium influx passing by these channels initiates the contraction process. Another crucial ion channels present in this process are the Ryanodine Receptors.

#### 2.2.3.2 Ryanodine Receptors

The existence of ion channels also occurs in the membrane of the intracellular organelle. One important example is the Ryanodine Receptors (RyRs), essential ion channels that, besides the LCCs, have a crucial role in myocyte dynamics.

Located in the Sarcoplasmic Reticulum (SR) membrane, the RyRs regulate muscle contraction by controlling the massive release of calcium ions from the SR into the cytoplasm.

When LCCs open, the influx of calcium ions into the cytoplasm causes a slight increase in the calcium concentration in specific regions of the intracellular medium. Located in these typical regions and, as calcium-sensitive ionic channels, the RyRs change their conformation due to this slight concentration increasing to an active or opened conformation. This opening permits the release of a massive quantity of calcium ions from the SR into the cytoplasm. At this moment, with the cytoplasm filled with calcium ions, the sarcomeres, organelles responsible for causing the contraction, alter their configuration, generating the cell compacting.

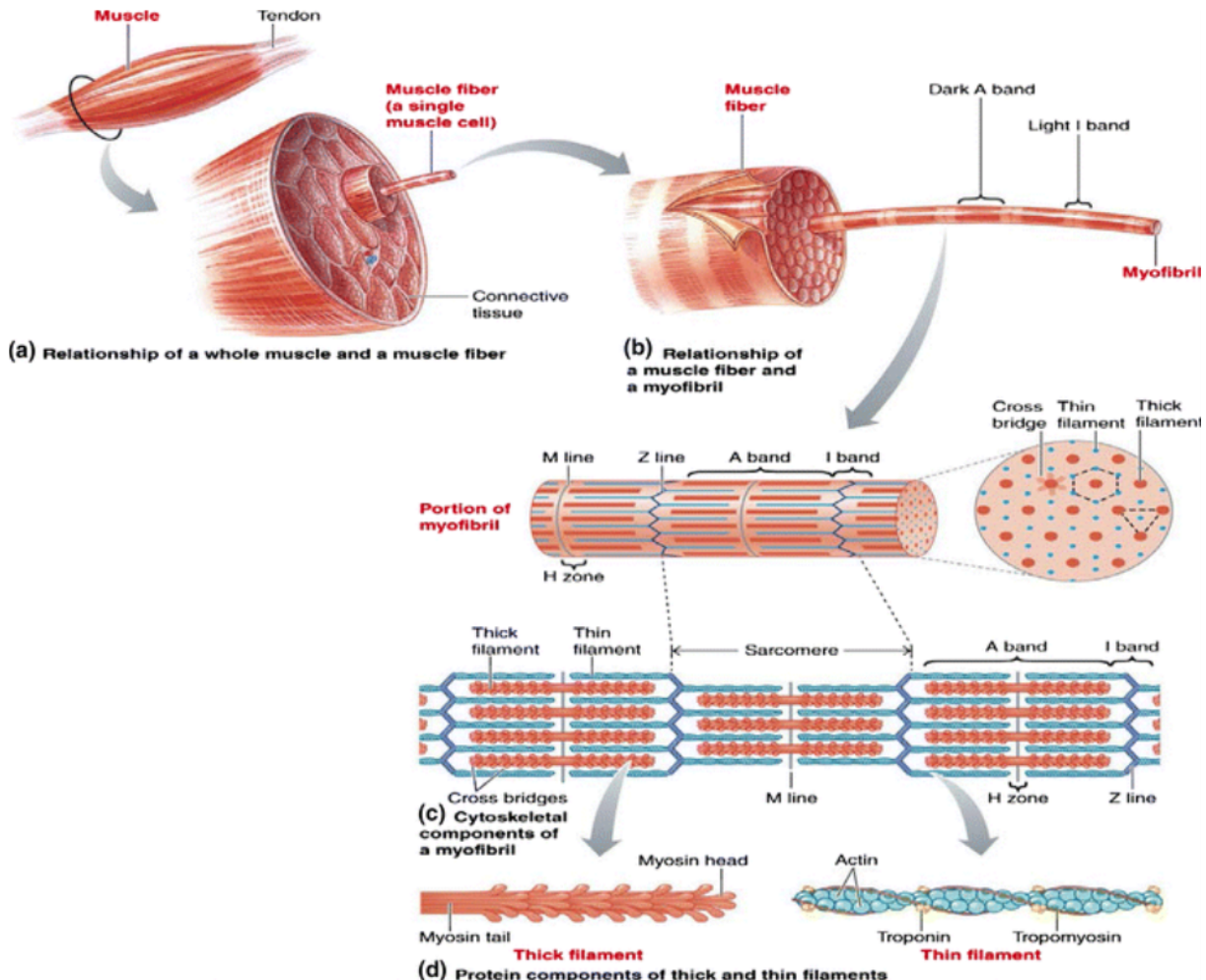
After the contraction, the RyRs rapidly close, contributing to the re-sequestering calcium ions back into the SR. This calcium uptake helps prevent excessive calcium accumulation in the cytoplasm and limits muscle contraction's extent and duration. Dysfunction of RyRs has been implicated in some human diseases, including malignant hyperthermia, a life-threatening reaction to anesthesia, and cardiac arrhythmias.

#### 2.2.4 Calcium-Induced Calcium Release Process

The calcium ions have a complex intracellular dynamic that initiates with an AP, leading to cellular contraction. This complex dynamic is named as Calcium-Induced Calcium Release (CICR) process. Besides the LCCs and the RyRs, described respectively in Sections 2.2.3.1 and 2.2.3.2, the Sarcoplasmic Reticulum (SR) is another crucial organelle for the CICR process.

All the CICR process is highly dependent on the ion Calcium presence. The ion Calcium is the key element that modifies the sarcomere disposition leading to cell contraction. The sarcomeres are the main ones responsible for the shortening movement of the cell and, consequently, for the generation of force by it. Figure 7 shows the composition of structures that form the muscles.

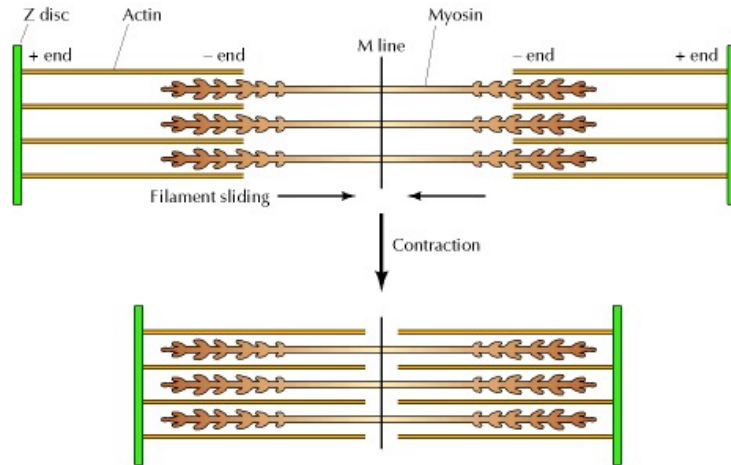
Figure 7 – Structural composition of a skeletal or cardiac muscle.



Source: obtained from Frontera and Ochala (22).

If observed in greater detail, a sarcomere is formed by Myosin and Actin myofilaments. These myofilaments are disposed of in a manner that overlaps to a large extent their extent. It is necessary because when they connect, these myofilaments slide between themselves, shortening the size of the sarcomere. Figure 8 shows the two extreme states where a sarcomere can stay: relaxed and contracted.

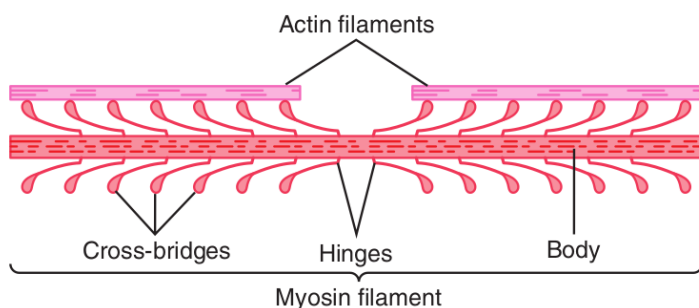
Figure 8 – Two extreme states that a sarcomere can assume: relaxed (top) and contracted (bottom).



Source: obtained from Pollard et al. (46).

This process of shortening in series by the various sarcomeres composing the multiple myofibrils that, in turn, form the myocytes, generates the muscle's strength as a whole. During an AP, calcium ions enter the cell through the LCCs. These ions alone are usually insufficient to initiate the sarcomere's contraction. However, these incoming ions serve as an initial cause of releasing a more significant amount of calcium ions stored by the SR. The RyR, as calcium-sensitive ion channels, have their conformation changed by this initial calcium increase, allowing a massive release of the calcium ions stored in the SR. This LCCs calcium influx and its influence on the RyR calcium release characterize the Calcium-Induced Calcium Release process. In this way, the cardiomyocyte, now with high levels of intracellular calcium concentrations, is induced to contract. Observing the actin and myosin myofilaments in more detail makes it possible to see that the myosin has structures resembling the arms arranged along its length (Figure 9).

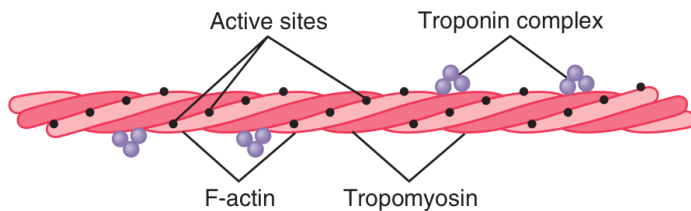
Figure 9 – Combination of many myosin molecules to form a myosin filament. Also shown are myosin cross-bridges and interaction between the heads of the cross-bridges with adjacent actin filaments.



Source: obtained from Hall (26).

These arms have structures called cross-bridges at their extremities. These bridges have an affinity for actin myofilament, where the bond between the two myofilaments is carried out. However, under normal conditions, this connection is prevented by a structure called tropomyosin. Tropomyosin surrounds actin myofilament, so the link between cross-bridges and active actin sites cannot occur. There is where the calcium ion acts. In actin myofilament, troponin structures are distributed along its length (Figure 10).

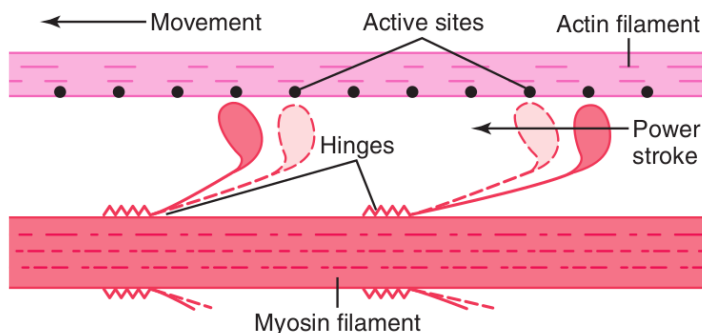
Figure 10 – Actin Myofilament in detail to the tropomyosin filaments, active locals and the complex of troponin.



Source: obtained from Hall (26).

When bound to calcium ions, this structure displaces the tropomyosin so that the active sites of the actin myofilament are exposed and able to bind to the cross-bridges. Once bonded, the sliding of one throughout the other, and thus the shortening of the sarcomere occurs. Figure 11 illustrates the sliding motion between the actin and myosin myofilaments.

Figure 11 – The “walk-along” mechanism for contraction of the muscle.

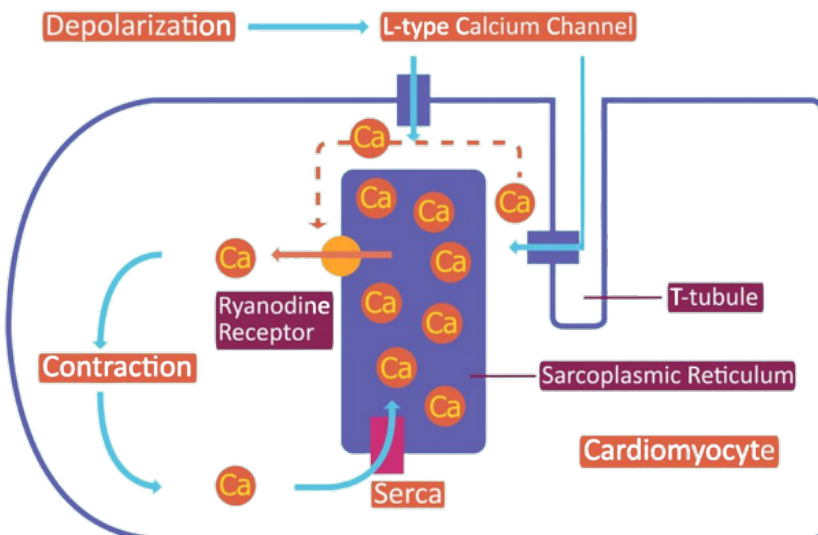


Source: obtained from Hall (26).

Once the intracellular calcium concentration reaches high levels, the calcium pump (SERCA) begins removing the calcium ion from within the cytoplasm by returning them to the sarcoplasmic reticulum. Due to this decrease in intracellular calcium levels, there is no binding between the calcium ions and the troponin. Thus, the active sites become overlapped by the tropomyosin preventing the connection of the myofilaments and causing the muscle to relax.

Figure 12 presents an illustration of the whole CICR cycle.

Figure 12 – Calcium-Induced Calcium Release process. As soon as an Action Potential reaches the cell causing an depolarization, the L-Type Calcium Channels open and allow an influx on calcium ions inside the cell. These calcium ions interact with the Ryanodine Receptors changing their conformation and, thus, opening these structures. This opening allows a massive influx of calcium ions from the Sarcoplasmic Reticulum inside the cytoplasm, thus, generating cellular contraction. After that, the SERCA pump reuptake these calcium ions from the cytoplasm to the Sarcoplasmic Reticulum reestablishing the resting condition.



Source: adapted from Warren (63).

### $\text{Ca}^{2+}$ Sparks\*

As discussed in Section 2.2.4, the calcium ion is crucial for shortening the myocyte and, thus, generating the force necessary to eject the blood from the cardiac chambers. However, despite the significant importance of these elements in the whole contraction process, these ions can not be present in the cellular myoplasm. It is because the calcium ions are responsible for the cellular contraction. Thus, since relaxation is another essential movement (without relaxing, the chamber would not allow the entrance of blood within it), the calcium ions must be removed from the intracellular medium to enable the cells to relax. The SERCA pumps predominantly do this uptake of the calcium ions and store them inside the SR.

Calcium Sparks in myocyte physiology are, by definition, a notable increase of calcium ions at any specific localization of the cytoplasm medium. In other words, it is a local increase in the intracellular calcium concentration. For instance, during the CICR

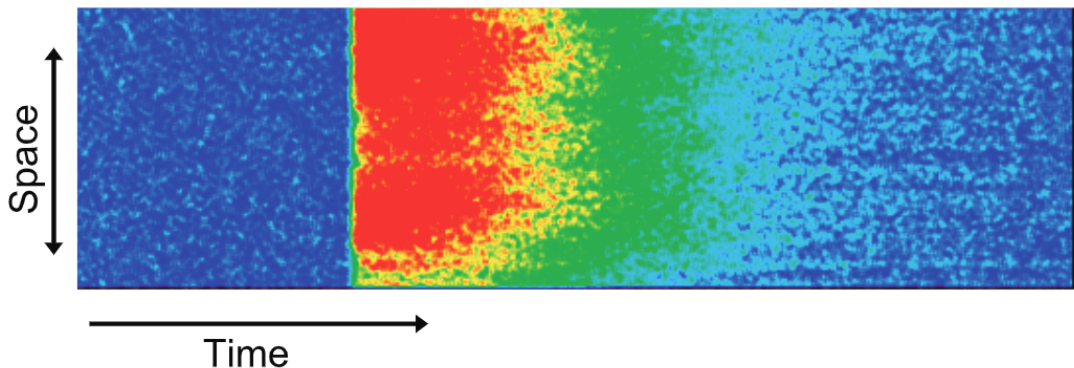
---

\*The concepts presented in this Section were based in the Cheng and Lederer (15) reference.

process, the synchronism of several calcium Sparks due to the whole cell excitation is crucial to fill the entire intracellular medium with calcium leading to cell contraction.

Concerning the calcium Sparks, according to Cheng and Lederer (15), they can be classified into two categories: an Evoked Spark and a Spontaneous Spark. The Evoked Sparks (ES) are calcium Sparks that occur during the active phase of the cell. Once stimulated, a cardiac myocyte performs an activity cycle until it restores the resting condition. An illustration of this cycle can be seen in the AP phases (Figure 4). Another association that can be made between this active cycle and the resting phase is the systole and diastole movements. So, in a particular point of view, an ES is expected, and, in addition, under a physiological pacing stimulation, it is crucial for correct cardiac functioning. Figure 13 presents a line scan image of an ES in response to an AP stimulation.

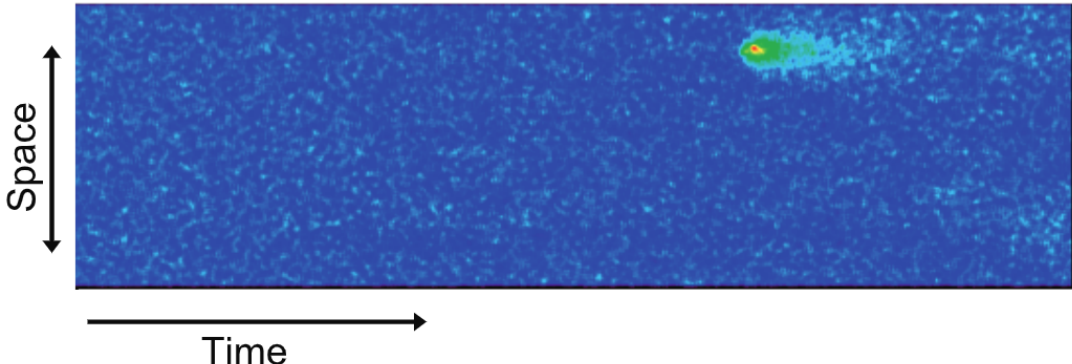
Figure 13 – Line scan confocal image of an Evoked Spark (ES) triggered by an Action Potention (AP) depolarization.



Source: adapted from Cheng et al. (16) apud Cheng and Lederer (15).

Conversely, there are also Spontaneous Sparks (SS). On the contrary to the ES, a SS occurs under an unstimulated condition. In this way, the SS are entirely unpredictable. The occurrence of an SS is not associated with previous signaling by the LCC or other transmembrane currents. Instead, even if the transmembrane potential maintain in resting condition (around -80mV), biological experiments still observe SS within the intracellular medium(4, 10, 11). It has been concluded that a SS is associated with the stochasticity present in RyRs dynamics, which, in turn, is related to the calcium concentrations in the cytosol and the SR. In contrast with Figure 13, Figure 14 presents a line scan image of an occurrence of a SS.

Figure 14 – Line scan confocal image of an Spontaneous Spark (SS).



Source: adapted from Cheng et al. (16) apud Cheng and Lederer (15).

A punctual SS usually remains local and solitary and, in this condition, can be seen as a physiological phenomenon. However, under non-control conditions such as, for instance, an elevated intracellular calcium concentration, a single SS can trigger a neighbor RyRs and initiate a wave propagation of calcium release into the cytosol. This process is named as Spark-Induced Spark Activation. This spontaneous widespread calcium release can lead to an asynchronous cell contraction and, thus, a pathological condition.

### 2.3 Computational Modeling of The Cardiac Electrophysiology

Heart activity involves several complex phenomena of different natures and scales. Due to this complexity, several mathematical/computational models that model an AP have been essential tools for a better understanding and study of these complex phenomena of electrophysiology. This Section presents the computational modeling studies that contributed to this area and were considered in developing this thesis.

#### 2.3.1 Hodgkin and Huxley Model

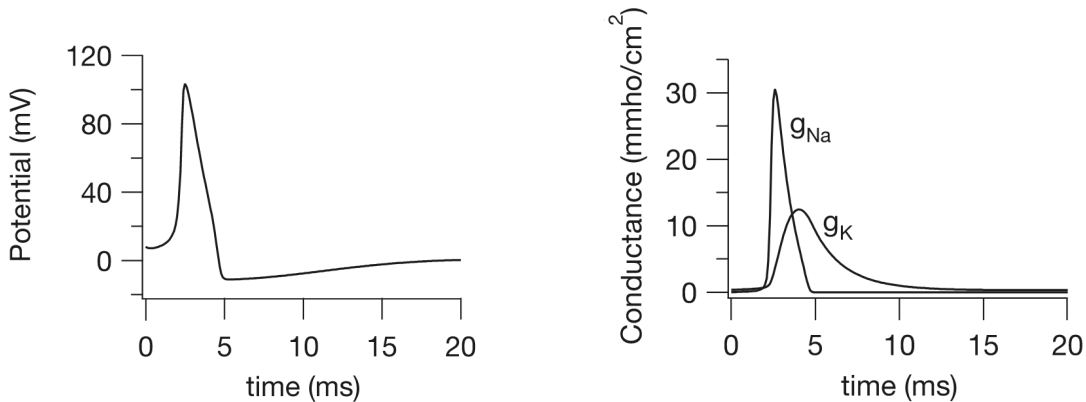
The Hodgkin and Huxley (29) study (HH) presents a quantitative model for the AP of a giant squid axon. Nevertheless, despite not having the original objective of simulating the heart's electrical activity, it is considered a cornerstone in the studies of this area. This original study was so important that in 1963 the authors were awarded the Nobel Prize in Medicine(38).

As presented in Section 2.2.1, an AP has four stages that constitute its cycle. During the depolarization phase, the cell membrane becomes very permeable to sodium due to the ion channel activities. Thus, it allows  $\text{Na}^+$  ions, present in greater concentration in the extracellular medium, to diffuse into the intracellular medium. Due to this high flow of  $\text{Na}^+$  ions into the cell, the transmembrane differential reaches positive values. In the next phase, repolarization, the potassium channels open while the sodium channels

close. In this way, due to the concentration gradient, potassium diffusion rapidly towards the extracellular medium, which restores the balance of the transmembrane differential. This sudden outflow of  $K^+$  ions in the repolarization phase can cause the transmembrane differential to reach values lower than at rest. In this case, the membrane is said to be hyperpolarized.

Figure 15 presents the transmembrane potential, the AP, and the conductivities of the  $I_{Na}$  and  $I_K$  currents over time. It can be noted how each current affects the AP.

Figure 15 – Simulation output generated by the Hodgkin and Huxley (29) model. In the left pane, the transmembrane potential (AP) is presented; in the right pane, it is presented the conductivities of the transmembrane ion currents  $I_{Na}$  and  $I_K$ .



Source: obtained from Keener and Sneyd (34).

In order to present a structure of a simple model, three essential elements were considered in the HH model: the cellular membrane, the sodium, and the potassium ion channels that permeate it. The membrane is electrically represented as a capacitor with capacitance  $C_m$ . Concerning the ion channels, in this model, there were considered three representations and their respective currents: the sodium current  $I_{Na}$ , the potassium current  $I_K$ , and a constant leakage current  $I_L$ .

Thus, the transmembrane potential  $V_m$  evolution over time is mathematically described by

$$\frac{dV_m}{dt} = -\frac{1}{C_m}(I_c + I_{stim}); \quad (2.1)$$

where  $I_{stim}$  is an input stimulus current; and the total transmembrane currents,  $I_c$ , is calculated as

$$I_c = I_{Na} + I_K + I_L. \quad (2.2)$$

The ionic channel currents  $I_{Na}$ ,  $I_K$ , and  $I_L$  are mathematically defined as

$$I_{Na} = g_{Na}(V_m - E_{Na}), \quad (2.3)$$

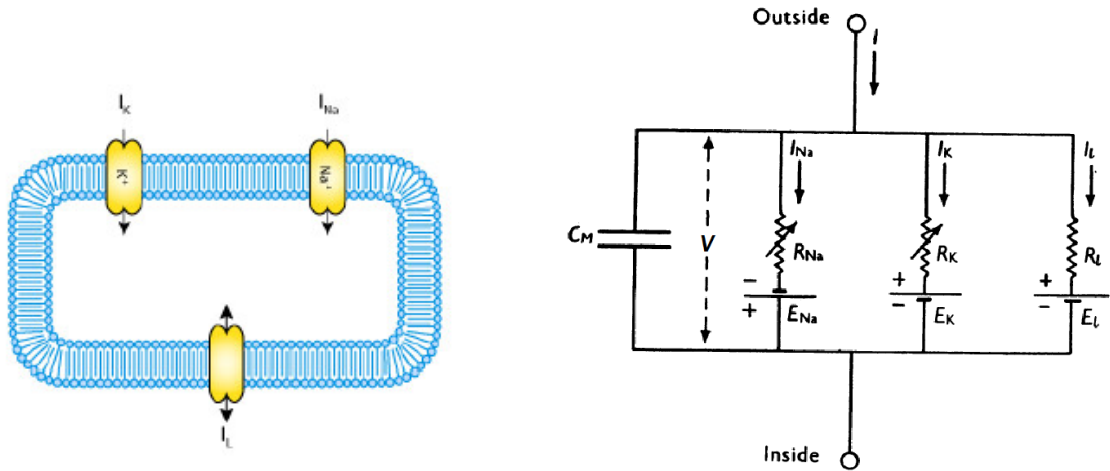
$$I_K = g_K(V_m - E_K), \quad (2.4)$$

and

$$I_L = g_L(V_m - E_L); \quad (2.5)$$

where  $g_{\bullet}$  are the perspectives conductivity parameter and the  $E_{\bullet}$  are the respective reversal potential, also named as Nernst Equilibrium Potential (34, p. 80). Figure 16 shows an illustration of the cell structures modeled by HH alongside an equivalent electric circuit that models these cellular structures.

Figure 16 – Hodgkin and Huxley (29) model representations. Left panel presents a schematic representation of the model (obtained from CellML (14)); right panel presents an equivalent electric circuit.



Source: obtained from Shepardson (56).

The HH model assumes that the  $I_L$  conductivity,  $g_L$ , is constant as well as the Nernst potentials  $E_{Na}$ ,  $E_K$  and  $E_L$ . On the contrary, the conductivity of the sodium channel,  $g_{Na}$ , and the conductivity of the potassium current,  $g_K$ , reads

$$g_{Na} = \bar{g}_{Na} m^3 h, \quad (2.6)$$

and

$$g_K = \bar{g}_K n^4; \quad (2.7)$$

where  $\bar{g}_{Na}$  and  $\bar{g}_K$  are constants that represents, respectively, the maximum conductivity of the  $\text{Na}^+$  and  $\text{K}^+$  channels. The terms  $m$  and  $h$  are, respectively, dimensionless variables of activation and inactivation of the  $I_{Na}$  current; and the term  $n$  is the variable associated with both activation and inactivation of the  $I_K$  current. These variables can be seen as a representation of the subunits of the respective ion channels, as discussed in Section 2.2.3.

To reproduce the biology associated with the subunits represented by the variables  $m$ ,  $h$ , and  $n$ , HH defined their evolution over time as

$$\frac{dm}{dt} = \alpha_m(1 - m) - \beta_m m, \quad (2.8)$$

$$\frac{dh}{dt} = \alpha_h(1 - h) - \beta_h h, \quad (2.9)$$

and

$$\frac{dn}{dt} = \alpha_n(1 - n) - \beta_n n. \quad (2.10)$$

The rates presented in Equations 2.8, 2.9, and 2.10 are voltage-dependent rates and is mathematically described as

$$\begin{aligned} \alpha_m &= 0.1 \frac{25-V_m}{\exp(\frac{25-V_m}{10})-1}, & \alpha_h &= 0.07 \exp\left(-\frac{V_m}{20}\right), & \alpha_n &= 0.01 \frac{10-V_m}{\exp(\frac{10-V_m}{10})-1}, \\ \beta_m &= 4 \exp\left(\frac{-V_m}{18}\right), & \beta_h &= \frac{1}{\exp(\frac{30-V_m}{10})+1}, & \beta_n &= 0.125 \exp\left(\frac{-V_m}{80}\right). \end{aligned}$$

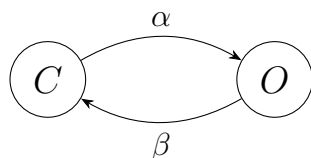
The voltage-dependence presented in the rates equation follows the voltage-sensitivity nature of the ionic channels considered by the HH model.

Based on the original HH model, the successor's studies referenced these mathematics models of the dimensionless variables  $m$ ,  $h$ , and  $n$  as the Hodgkin and Huxley Gates model. It is associated with these variables acting as gates that open and close themselves, controlling the ion fluxes over the membrane. For a more detailed description and analysis of the HH model, see Keener and Sneyd (34, p. 196).

### Hodgkin and Huxley (29) Gates Model

In the HH Model, the authors present ionic currents equations based on variables such that these variables behave as gates allowing ions' flux through the cellular membrane. In this way, if we consider one single ionic channel, these variables, or gates, can be in two different states: opened or closed. Besides that, they have explicit probabilities of changing their state ( $\alpha$  to open and  $\beta$  to close). Schematically, this dynamic can be illustrated as shown in Figure 17.

Figure 17 – Schematic representation for Hodgkin and Huxley (29) Gate model.



Source: Created by the author. (2023).

Considering this two-state scenario, these probabilities  $\alpha$  and  $\beta$  can be mathematically described as follow. Given the amount of  $N$  channels, consider  $P$  the fraction

of channels in the open state  $O$ . Similarly, it can be seen  $1 - P$  as the fraction of the  $N$  channels that are in the closed state  $C$ . In a time step, the portion of channels that switches to the open state can be described as the number of channels in the closed state multiplied by the probability of a single channel opening. Mathematically, it can be described as  $\alpha \times (1 - P)$ . Similarly, the number of channels that switch from the opened to the closed state can be described mathematically as  $\beta \times P$ .

When the system is in equilibrium, the fraction of opened and closed states can be compared as

$$\alpha(1 - P_\infty) = \beta P_\infty \quad (2.11)$$

where  $P_\infty$  is the portion of the  $N$  channels in the opened state under the equilibrium condition. In this way,  $P_\infty$  can be calculated as

$$P_\infty = \frac{\alpha}{\alpha + \beta}. \quad (2.12)$$

If it is considered a system during a transitory condition, the fraction of channels in the opened state,  $P$ , will vary over time as described by the Ordinary Differential Equation (ODE)

$$\frac{dP}{dt} = \alpha(1 - P) - \beta P. \quad (2.13)$$

The solution for the ODE 2.13 can be described by

$$P = -P_{initial} \exp(-t/\tau) \quad (2.14)$$

where  $P_{initial}$  is the initial condition of  $P$  and

$$\tau = \frac{1}{\alpha + \beta}. \quad (2.15)$$

Thus, the transition rates  $\alpha$  and  $\beta$  can be described in function of  $P_\infty$  and  $\tau$  using a combination of the equations 2.12 and 2.15. Equations 2.16 and 2.17 presents, respectively, the mathematical description for  $\alpha$  and  $\beta$  rates.

$$\alpha = \frac{P_\infty}{\tau} \quad (2.16)$$

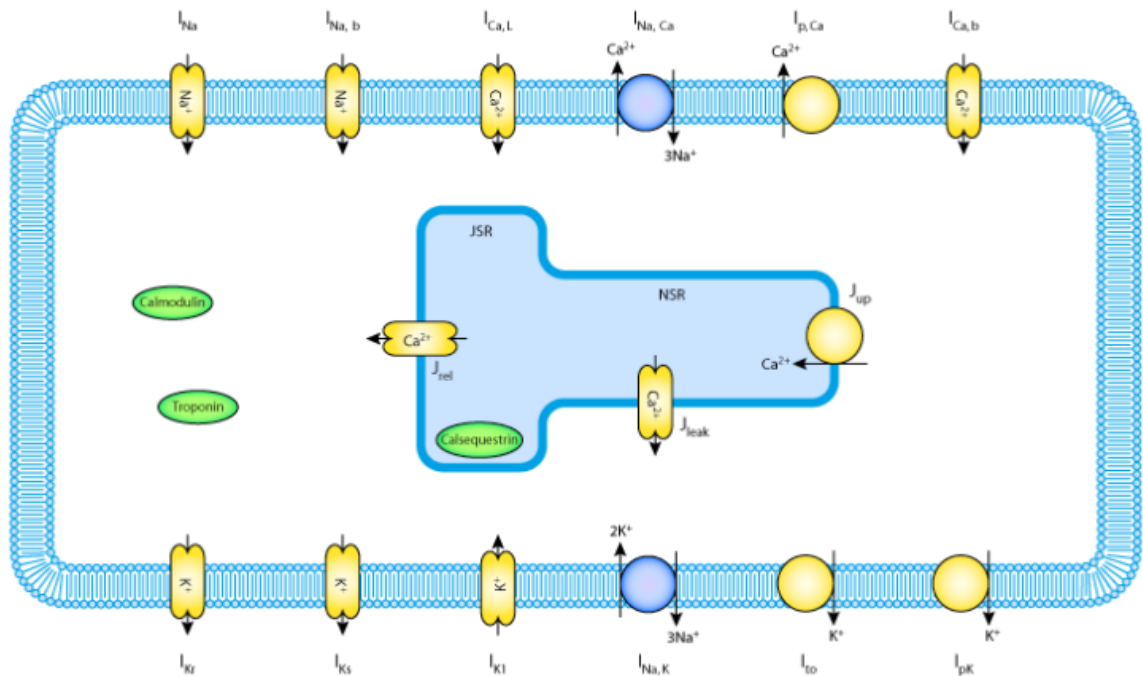
$$\beta = \frac{1 - P_\infty}{\tau} \quad (2.17)$$

As mentioned, several studies in cardiac electrophysiology ensued after the HH model adopted this HH Gate formalism to simulate the ionic channels opening and closing dynamics. As an object of study of this thesis, the ten Tusscher et al. (61), and the ten Tusscher and Panfilov (62) are examples of using the HH Gate formalism.

### 2.3.2 Ten Tusscher et al. Model

The model developed by ten Tusscher et al. (61) (TT) presents a mathematical model for the electrophysiology of human ventricular cells, widely used to simulate arrhythmias (24). The model is based on the HH framework and includes ionic currents such as fast sodium, delayed rectifier potassium, inward rectifier potassium, L-type calcium, and rapid and slow components of the transient outward potassium currents. In addition, the model also includes a description of the intracellular calcium dynamics, which is crucial for capturing the dynamics of the L-type calcium current. The model was calibrated using experimental data from isolated ventricular myocytes and could reproduce a wide range of physiological phenomena, including action potential duration and frequency dependence. Figure 18 shows a schematic representation of the cell and the structures considered by the model.

Figure 18 – Schematic representation of the biological structures considered in ten Tusscher et al. (61) model.



Source: obtained from CellML (13).

In the same way as in HH, in TT, the cellular membrane is modeled as a dielectric of capacitance  $C_m$  connected in parallel with resistors, expressing the ion channels, and batteries, expressing pumps. The evolution of the transmembrane potential  $V$  over time can be written as

$$\frac{dV}{dt} = -\frac{I_{ion} + I_{stim}}{C_m} \quad (2.18)$$

where  $I_{stim}$  is an input stimulus current; and  $I_{ion}$  is the sum of all the ionic currents considered in the model. Equation

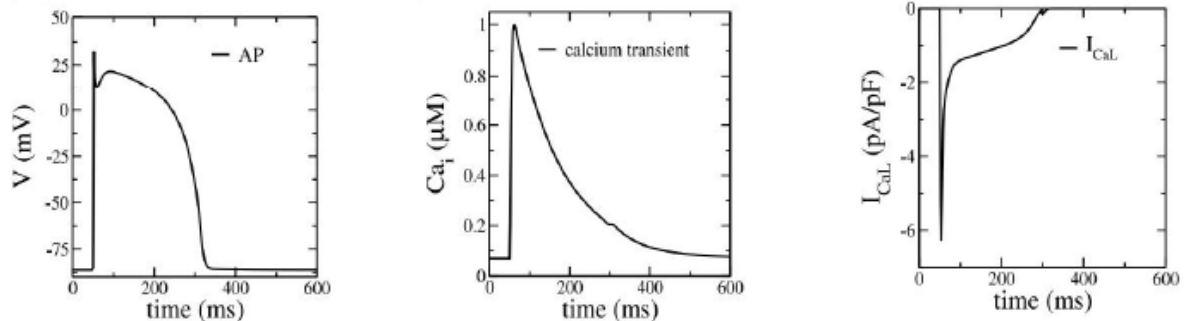
$$I_{ion} = I_{Na} + I_{K1} + I_{to} + I_{Kr} + I_{Ks} + I_{CaL} + I_{NaCa} + I_{NaK} + I_{pCa} + I_{pK} + I_{bCa} + I_{bNa} \quad (2.19)$$

presents the  $I_{ion}$  mathematics.

As seen in Equation 2.19, unlike the HH base model, TT considers a more comprehensive range of currents. This model includes several ionic currents, such as the fast sodium current ( $I_{Na}$ ), the L-type calcium current ( $I_{CaL}$ ), the transient outward potassium current ( $I_{to}$ ), the rapid delayed rectifier potassium current ( $I_{Kr}$ ), the slow delayed rectifier potassium current ( $I_{Ks}$ ), the inward rectifier potassium current ( $I_{K1}$ ), the sodium-calcium exchanger ( $I_{NaCa}$ ) current, the sarcolemmal calcium pump ( $I_{pCa}$ ), the slow inward rectifier potassium current ( $I_{NaK}$ ), the sodium-potassium pump current ( $I_{pK}$ ), and the respective background currents of potassium ( $I_{bK}$ ) and sodium ( $I_{bNa}$ ). To validate the dynamics of these currents, TT considered the ventricular myocyte model developed by Priebe and Beuckelmann (48), and the atrial myocyte model developed by Courtemanche et al. (20).

Figure 19 shows the transmembrane potential  $V$ , the intracellular calcium concentration  $[Ca]_i$ , and the  $I_{CaL}$  current curves obtained as an output of the simulation of the original TT model. The parameters correspond to a ventricular cell with a stimulus frequency of 1 Hz.

Figure 19 – Graphic representation of the results obtained by the ten Tusscher et al. (61) model.



Source: adapted from ten Tusscher et al. (61).

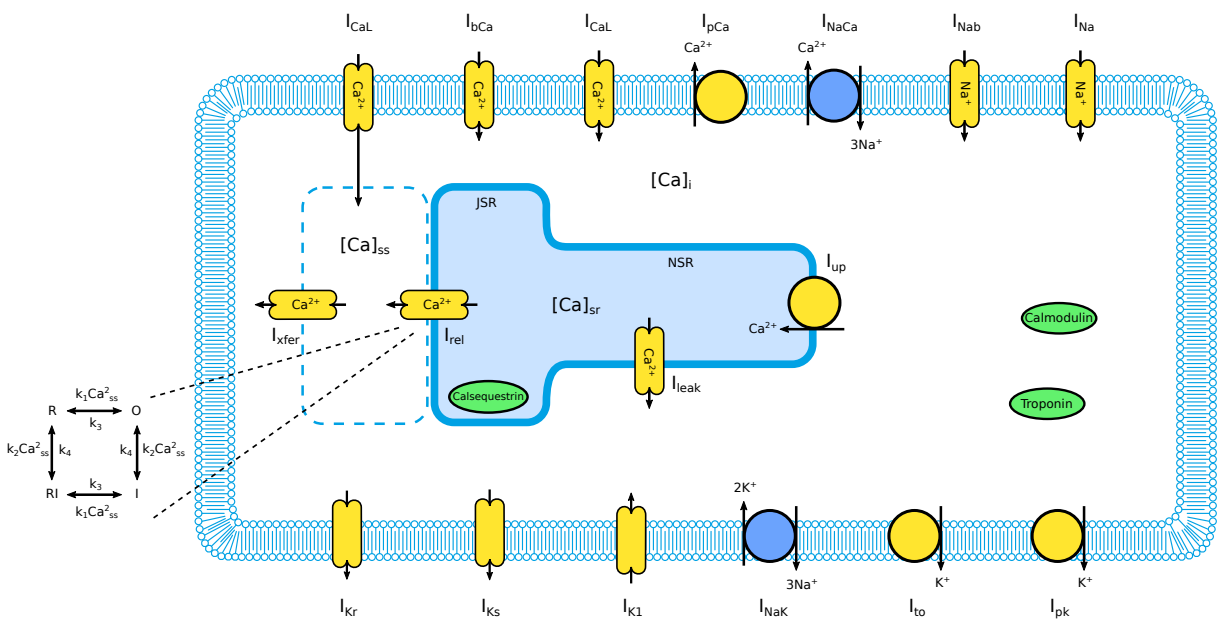
In ten Tusscher and Panfilov (62) study, the authors reformulated the calcium equation to better reproduce intracellular calcium dynamics in cardiac cells. According to the authors, the original TT model was found to have limitations in its representation

of calcium dynamics, particularly during rapid changes in cellular excitation. The reformulated equation in the ten Tusscher and Panfilov (62) paper improved the modeling of intracellular calcium dynamics, allowing for more accurate predictions of physiological phenomena such as calcium transients and sarcoplasmic reticulum calcium release.

### 2.3.3 Ten Tusscher and Panfilov Model

The ten Tusscher and Panfilov (62) (TP) ventricular model is a revised version of the TT model, with refinements made to the calcium handling mechanisms. The main difference from the previous version was incorporating a more detailed description of the calcium handling mechanisms, including reformulating the calcium equation to improve the reproduction of experimental data. This improved representation of the calcium dynamics allowed a better reproduction of physiological phenomena such as action potential duration and frequency dependence. Additionally, the TP model included refinements to the sodium, potassium, and calcium currents to better approximate experimental data. After that, this model became one of the most used for computational simulations of human heart cells (44). The new structure of the cellular model is shown in the schematic representation presented Figure 20.

Figure 20 – Schematic representation of the ten Tusscher and Panfilov (62) Model.



Source: adapted from CellML (13).

As previously developed in the TT model, the variation of AP over time for single cells was represented according to the following differential equation:

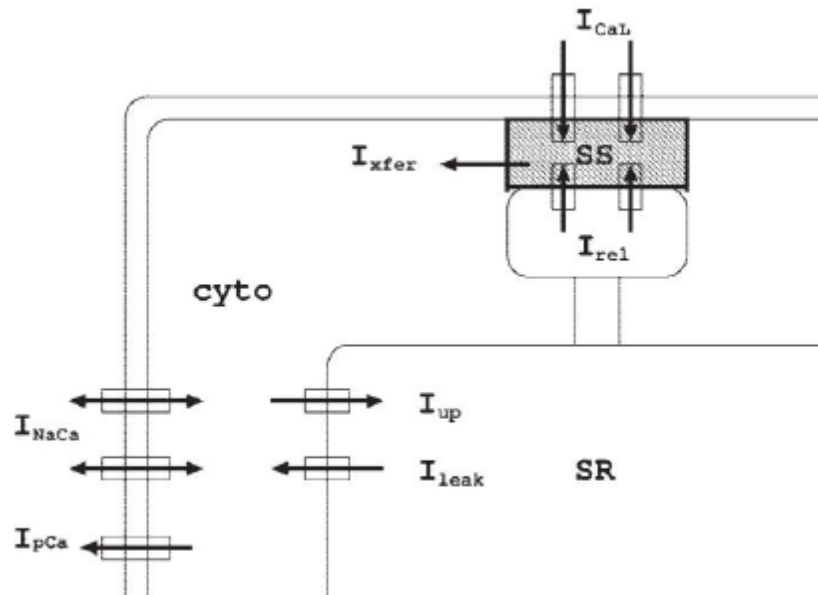
$$C_m \frac{dV}{dT} = -(I_{ion} + I_{stim}) \quad (2.20)$$

where  $C_m$  is the membrane capacitance,  $I_{stim}$  is the input stimulus current and  $I_{ion}$  is the total ionic current. In addition, the  $I_{ion}$  current remained the same as described in the TT (Equation 2.17).

The main improvement implemented in the TP model is associated with intracellular calcium dynamics. This new version included a dynamic model of the ryanodine receptors and reformulated the calcium equation to account for calcium-induced calcium release from the SR through the RyR. This improved representation of calcium handling in the SR allowed for better simulation of SR calcium release and reuptake dynamics. Besides that, this new version also defined a specific calcium site denominated as dyadic subspace (ss). This region comprises the location near the LCCs and the RyR.

With this new conformation, the LCCs allow the entrance of calcium into the subspace. The calcium-sensitive RyR receive this slight increase in subspace calcium concentration and act, allowing a massive release of calcium ions from the SR. The exchanger  $I_{NaCa}$  and the pump  $I_{pCa}$  take the calcium ion to the cell's exterior. The  $I_{up}$  calcium pump in the SR membrane returns the calcium for the interior of the organelle. The  $I_{leak}$  current also models a calcium leak from SR to the intracellular medium. Finally, the intracellular  $I_{xfer}$  current represents the flux of calcium ions from the subspace region to the cytoplasm. Figure 21 shows a detailed representation of these structures.

Figure 21 – Schematic representation of the structures that compose the intracellular calcium dynamics implemented by ten Tusscher and Panfilov (62).

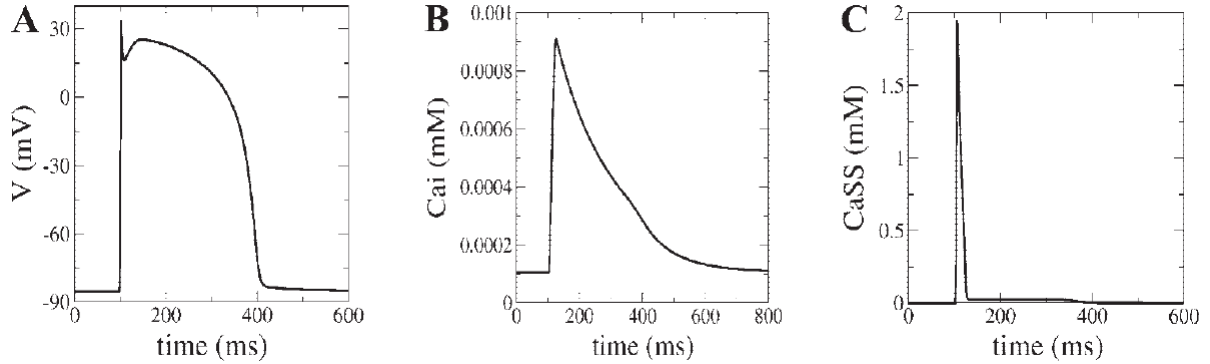


Source: obtained from ten Tusscher and Panfilov (62).

Figure 22 shows the transmembrane potential  $V$ , the free intracellular calcium

concentration  $[Ca]_i$ , and the free subspace calcium concentration  $[Ca]_{ss}$  curves obtained as an output of the simulation of the TP model. The parameters correspond to a ventricular cell from the epicardial region with a stimulus frequency of 1 Hz.

Figure 22 – Graphic representation of the results obtained by the ten Tusscher and Panfilov (62) model.



Source: adapted from ten Tusscher and Panfilov (62).

The TP model is the central topic of this thesis study. Since the TP model has defined the CICR phenomena in its formulation, this thesis adjusted this model to insert the capacity to simulate the CICR process over a multiscale approach. Comprehending the specific formulations of the LCCs and the RyRs is crucial for this thesis development.

### 2.3.3.1 Ten Tusscher and Panfilov LCC Model

The representation of the LCCs inside the TP model is through the  $I_{CaL}$  current. This current is described by an equation that includes four HH-based gates ( $d$ ,  $f$ ,  $f_2$ , and  $f_{cass}$ ), which control the activation and inactivation of the current over time. The specific form of the LCCs gates in the TP model was modified from the original HH to fit and adequately describe the experimental data behavior.

The L-type  $\text{Ca}^{2+}$  current  $I_{CaL}$  from the TP model reads

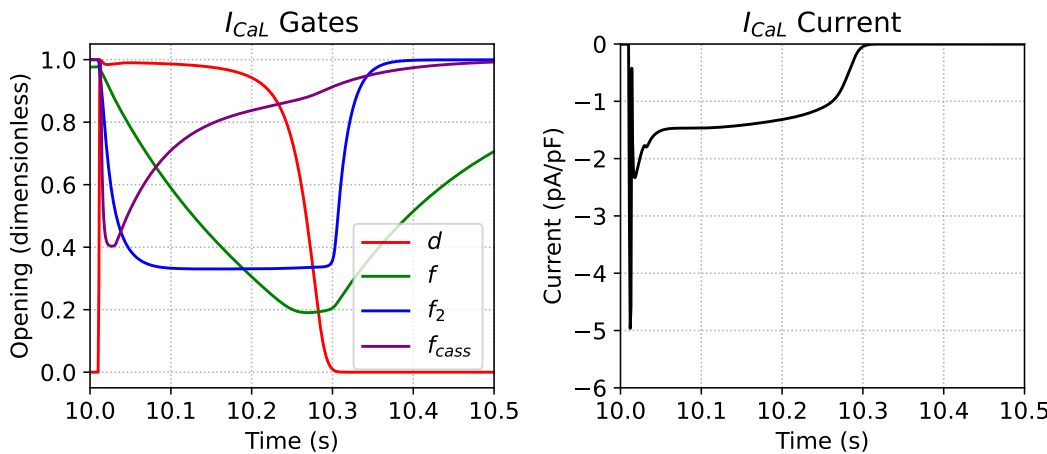
$$I_{CaL} = g_{CaL} d f f_2 f_{Cass} 4 \frac{(V - 15)F^2}{RT} \frac{0.25 [Ca]_{ss} \exp(\frac{2(V-15)F}{RT}) - [Ca]_o}{\exp(\frac{2(V-15)F}{RT}) - 1} \quad (2.21)$$

where  $g_{CaL}$  is the maximum conductivity of the channel;  $V$  is the transmembrane potential;  $[Ca]_{ss}$  is the calcium concentration inside the subspace region;  $[Ca]_o$  is the extracellular calcium concentration; and  $R$ ,  $T$  and  $F$  are physics constants. The variables  $d$ ,  $f$ ,  $f_2$ , and  $f_{cass}$  are the HH-based gates.

Gate  $d$  simulates the activation of the  $I_{CaL}$  current, assuming values close to 1, indicating that the channel is fully open and allowing a large flow of calcium ions; gate  $f$  simulates

the inactivation of the current, assuming values close to 0, indicating that the channel is closed and not allowing ion flow; gate  $f_2$  simulates a slow inactivation process, which occurs over a longer time scale than the inactivation represented by  $f$ ; and  $f_{cass}$  gate simulates the rapid activation and deactivation kinetics of the calcium-activated slow component of the  $I_{CaL}$  current. In summary, gates  $d$ ,  $f$ , and  $f_2$  are voltage-dependent, and the gate  $f_{cass}$  is calcium-dependent. Figure 23 presents the correlation of the  $I_{CaL}$  current and its four gates over time.

Figure 23 –  $I_{CaL}$  gates dynamics (left panel) in comparison with  $I_{CaL}$  current (right panel) of the ten Tusscher and Panfilov (62) model.



Source: Created by the author. (2023).

The ODEs that rule these four gates dynamics are based on HH formalism described in Section 2.3.1. In this way, each one of the four gates has its respective  $\alpha_\bullet$  and  $\beta_\bullet$  transition rates. The dynamic of the gates over the time can also be mathematically describe in terms of the  $\bullet_\infty$  and  $\tau_\bullet$  variables. These equations reads

$$\frac{dd}{dt} = \frac{d_\infty(V) - d}{\tau_d(V)}, \quad (2.22) \quad \frac{df}{dt} = \frac{f_\infty(V) - f}{\tau_f(V)}, \quad (2.23)$$

$$\frac{df_2}{dt} = \frac{f_{2\infty}(V) - f_2}{\tau_{f2}(V)}, \quad (2.24) \quad \frac{df_{cass}}{dt} = \frac{f_{cass\infty}([Ca]_{ss}) - f_{cass}}{\tau_{f_{cass}}([Ca]_{ss})}; \quad (2.25)$$

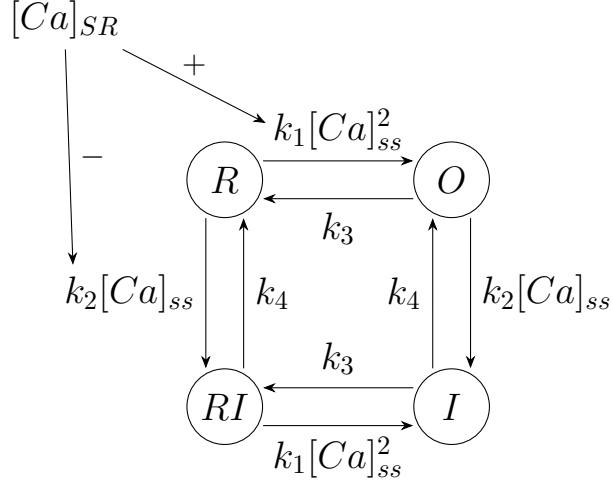
where  $d_\infty$ ,  $\tau_d$ ,  $f_\infty$ ,  $\tau_f$ ,  $f_{2\infty}$ , and  $\tau_{f2}$  are voltage-dependent rates; and  $f_{cass\infty}$  and  $\tau_{f_{cass}}$  are calcium-dependent rates. For more details of the four TP  $I_{CaL}$  current formulation, see ten Tusscher and Panfilov (62, p. 11).

### 2.3.3.2 Ten Tusscher and Panfilov RyR Model

The insertion of the Ryanodine Receptors (RyRs) mathematics was a considerable improvement for the TP model, especially if it is considered the reproduction of the CICR

process. To do this incorporation, TP considered a reduced version of the four-state Markov Chain (MC) used by Shannon et al. (54) and Stern et al. (57) to simulate the same phenomenon in their study. Figure 24 illustrates the original four-state Markov Chain model implemented by Shannon et al. (54) and Stern et al. (57).

Figure 24 – A schematic representation of the four-state Ryanodine Receptor Markov Chain model of Shannon et al. (54) and Stern et al. (57).



Source: adapted from ten Tusscher and Panfilov (62).

The states  $R$ ,  $O$ ,  $I$ , and  $RI$  are the four possible states and represent the resting closed state, the open conducting state, the inactivated closed state, and the resting inactivated closed state. In addition,  $k_1$  and  $k_2$  are transition rates dependent on the  $[Ca]_{SR}$ ;  $[Ca]_{ss}$  is the subspace calcium concentration;  $k_3$  and  $k_4$  are constant rates.

The four-state model incorporates both influences of the subspace calcium concentration (the trigger) and the sarcoplasmic reticulum calcium concentration (the load) on receptor opening and closing dynamics by making the transition rates dependent on these concentrations. These features are in accordance with the CICR process.

The reduced version used by TP consider only two-state MC model  $R$  and  $O$ . The equation that describe their evolution over time is

$$\frac{d\bar{R}}{dt} = -k_2[Ca]_{ss}\bar{R} + k_4(1 - \bar{R}) \quad (2.26)$$

where  $\bar{R} = R + O$ ;  $R$  is the resting closed state, and  $O$  is the open conducting state. The equation to obtain the specific  $O$  value reads

$$O = \frac{k_1[Ca]_{ss}^2\bar{R}}{k_3 + k_1[Ca]_{ss}}. \quad (2.27)$$

Formulated using this reduced two-state MC, the RyR release current  $I_{rel}$  implemented in TP model is mathematically described by

$$I_{rel} = V_{rel}O([Ca]_{SR} - [Ca]_{ss}) \quad (2.28)$$

where  $V_{rel}$  is the parameter to represent the maximum  $I_{rel}$  conductance;  $O$  is the portion of RyR in open state;  $[Ca]_{SR}$  and  $[Ca]_{ss}$  are, respectively the calcium concentration inside the Sarcoplasmic Reticulum and in the dyadic subspace.

### 2.3.4 Deterministic X Stochastic Modeling

Mathematical/computational models can be classified as deterministic or stochastic. According to Caradec and Martorano (12), Deterministic Models are such as all their formulations are based only on deterministic equations, in other words, equations that do not involve random variables. These models will always generate the same outputs considering the same starting condition. Conversely, the Stochastic Models are characterized by stochastic terms in their formulations, such as Random Variables. Contrary to the Deterministic Models, the outputs of the Stochastic Models are highly dependent on the randomness present in the Random variables and, thus, even considering the same starting condition, its results might be different for distinct realizations.

In deterministic models, it considers average values. In this way, a known input data collection will always lead a given system to the same data set in the output. However, a limitation of this model is the impossibility of analyzing the exclusive effect that each input value could cause in the process since it considers the average between them (59).

The presence of random variables in stochastic models describes the ionic currents as random processes and incorporates statistical methods to represent the behavior of ion channels. For instance, this approach considers the effects of noise and fluctuations on the electrical activity of heart cells. Moreover, it allows for the simulation of multiple realizations of the same system to estimate the variability of the outputs. These outputs must be interpreted as a statistical result of the object of study (59).

Both approaches have advantages and disadvantages and are used for different purposes in cardiac modeling. Stochastic models are more suitable for understanding the effects of noise and fluctuations on the electrical activity of heart cells and, thus, more suitable to achieve a more faithful reproduction of the real problem (59). While the deterministic models are better suited for understanding the relationships between ionic currents and gating variables and their contribution to the electrical activity of heart cells.

In addition, as an object of study of this thesis, stochastic and deterministic models are also directly associated with the scale of the scenario being modeled. Deterministic models provide a deterministic description of the electrical behavior of the heart and are used to model the overall heart behavior at the organ level. Stochastic models, on the other hand, consider the influence of random processes such as ion channel fluctuations and are used to model the behavior of individual cells. Stochastic models can be typically used for simulations at a cellular or subcellular scale, while deterministic models are used for simulations at an organ or systemic scale.

### 3 METHODS

The main objective of this thesis is to propose and analyze a novel computational model capable of reproducing the CICR dynamics of human ventricular cells in different scales. This model could contribute to studies that aim to understand how the subcellular structures correlate with the whole cell functions.

At the molecular level, the structure and function of individual ion channels and transporters can be studied in detail. However, this approach raises the probabilistic nature of the ion channel dynamics, and it is essential to consider this feature in studies at this subcellular level. On the other hand, at the cellular level, it is possible to observe the overall behavior of the myocyte, but it is more difficult to understand the underlying mechanisms. In this case, the probabilistic nature of a single ion channel is suppressed by the average behavior of thousands of these structures acting simultaneously.

This multiscale approach can be directly associated with the Stochastic and Deterministic Models. As described in Section 2.3.4, the presence of random variables in Stochastic models can adequately reproduce the probabilistic nature of a single ion channel. On the other hand, the average assumptions considered in Deterministic models match the macro scale nature.

The TP model is widely used to reproduce deterministic outputs of the left ventricular human myocytes. Due to this, it was selected as the base model to develop the multiscale model. However, as discussed, on a micro scale, the probabilistic nature of a single ion channel must be present.

Considering the main object of study, the CICR process, and the choice by the TP model, it is necessary to prepare this model to simulate the stochastic scenario. For this, the Markov Chain structures are a powerful tool to capture this feature of ion channel gating.

In the TP model, the RyRs dynamics, represented by the  $I_{rel}$  current, are already expressed using an MC-based formulation. However, the LCCs dynamics, represented by the  $I_{CaL}$  current, use HH gating-based mathematics. So, replacing the HH gating-based LCCs opening dynamics with an MC-based version was the first and crucial step to turn TP capable of performing stochastic simulations on the CICR process.

Moving forward, the label DTP will be used to represent the Deterministic version of the novel model proposed in this thesis. This novel version will differ from the original TP particularly in its LCCs formulation. At last, to introduce the Stochastic feature in the DTP, Binomial Random variables were used in the MC-based formulations. This new modification is labeled as STP. The thesis Simulation Experiments were generated using the STP model and they were compared with the DTP model.

### 3.1 MC-Based $I_{CaL}$ Version

An extensively employed mathematical model based on a MC description to simulate the electrophysiology of cardiac cells is described in Mahajan et al. (36) (MJ). The main objective of the model presented in MJ is accurately reproducing the cardiac AP and the Intracellular Calcium Cycling at rapid heart rates. Starting from a previous rabbit cardiac model (55), MJ modified the formulation of the  $I_{CaL}$  current by replacing it with a seven-state Markovian model. The  $I_{CaL}$  equation proposed by MJ reads

$$I_{CaL} = P_o \times \bar{g}_{Ca} \frac{4P_{Ca}VF^2}{RT} \frac{c_s e^{2(VF/RT)} - 0.341[Ca^{2+}]_o}{e^{2(VF/RT)} - 1}, \quad (3.1)$$

where  $P_o$  is the Opening fraction of the channels (represented by a Markovian Open state),  $\bar{g}_{Ca}$  is the maximum conductivity parameter,  $V$  is the transmembrane potential, and  $c_s$  is the submembrane calcium concentration. The other terms are parameters of the model or physical constants.

As described in Section 2.3.3, TP adopted the HH Gate-based approach to simulate the opening fraction dynamics of the  $I_{CaL}$  current. Rearranging the terms, the original  $I_{CaL}$  equation for the models reads

$$I_{CaL} = df f_2 f_{cass} \times G_{CaL} \frac{4(V - 15)F^2}{RT} \frac{0.25c_{ss} e^{2(V - 15)F/RT} - [Ca^{2+}]_o}{e^{2(V - 15)F/RT} - 1}, \quad (3.2)$$

where  $d$ ,  $f$  and  $f_2$  are the three voltage-dependent gates, and  $f_{cass}$  is the calcium-dependent one;  $G_{CaL}$  is the maximum conductance of the current;  $V$  is the transmembrane potential; and  $c_{ss}$  is the subspace calcium concentration. The other terms are model parameters or physical constants.

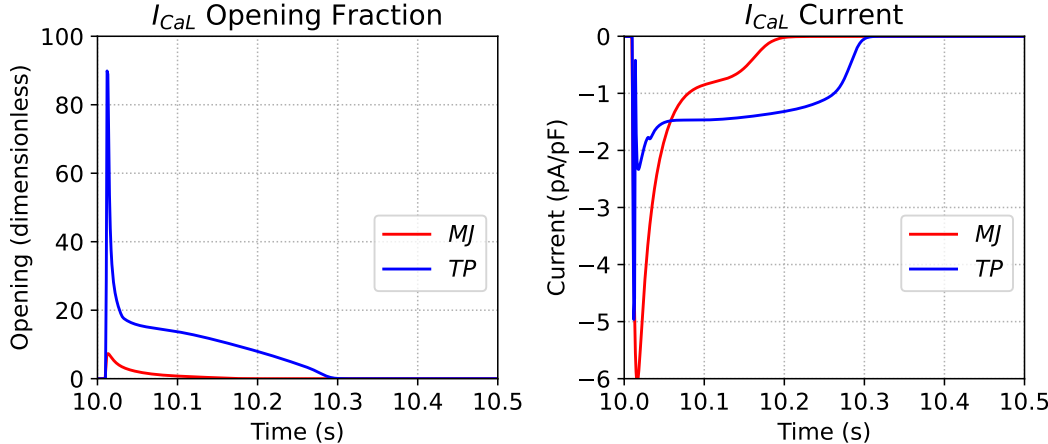
As can be seen, the two cited models, MJ, and TP, simulate the same phenomenon, and, disregarding the parameters and the values of the physical constants, they use the same equation to simulate the  $I_{CaL}$  current. Furthermore, it is possible to read the  $I_{CaL}$  equation of the two models as a multiplication of two terms:

$$I_{CaL} = O_f \times I_{max}; \quad (3.3)$$

where  $O_f$  is the channels Opening fraction and the  $I_{max}$  is the maximum current value when all channels are open. In MJ model, this opening fraction term is represented by the Markovian state  $P_o$  and reaches peak levels around 10% of opening. On the other hand, in TP model, this opening fraction is represented by the multiplication of the four gates  $d$ ,  $f$ ,  $f_2$ ,  $f_{cass}$ , and reaches the peak of around 90% in the opening levels. In the first moment, this difference in the amplitude of the opening fraction values can look weird. However, it is important to highlight the different natures that each model assumes. For instance, MJ focus on models for the cardiac cells of rabbits. In contrast, TP propose models for the cardiac cells of humans.

Therefore, the difference observed in Figure 25, showing the dynamics of the opening fraction,  $O_f$ , and the  $I_{CaL}$  current over the time for the models from MJ, and TP, may be due to the differences between rabbits and humans.

Figure 25 – Output dynamics generated by the simulation of the models Mahajan et al. (36) (MJ), and ten Tusscher and Panfilov (62) (TP). Left panel shows the  $I_{CaL}$  Opening Fraction,  $O_f$ ; right panel shows the  $I_{CaL}$  current.

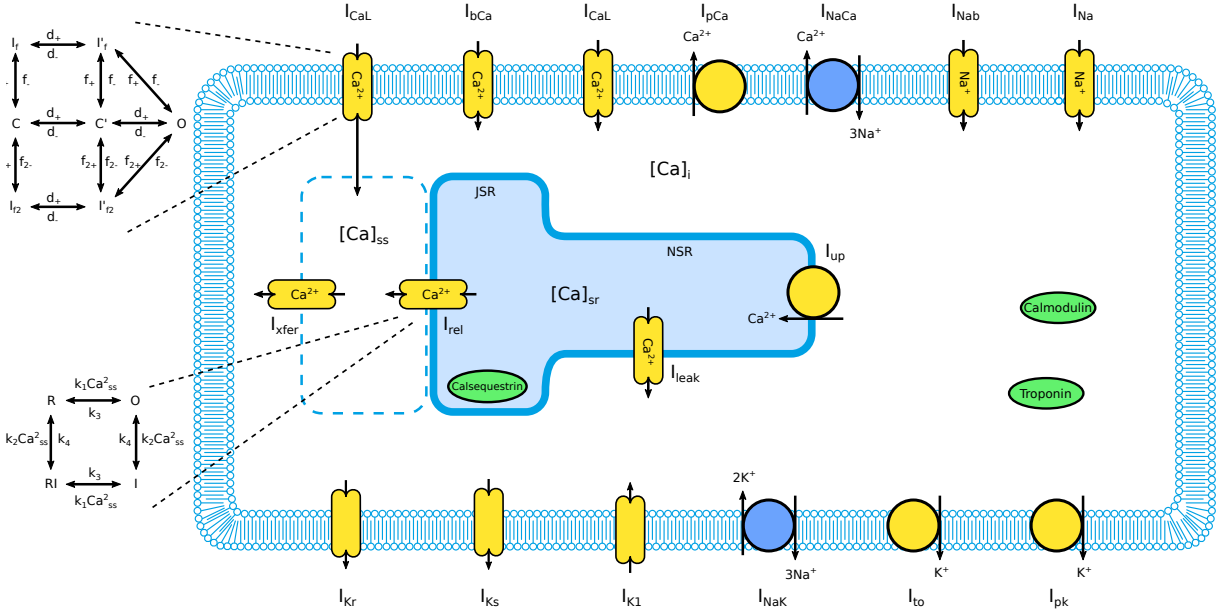


Source: Created by the author. (2023).

As stated above, there are two approaches to model the opening fraction dynamics. MJ use an MC-based structure, while TP use a Gate-based formulation. However, as discussed by MJ, the use of an MC-based approach naturally models the ion channel biophysical properties in terms of molecular transitions between discrete conformation states.

The first goal of this work is to propose and test a new MC-based  $I_{CaL}$  model that can replace the opening fraction,  $O_f$ , composed by the four gates  $d$ ,  $f$ ,  $f_2$ ,  $f_{cass}$ , initially used in TP model. For that, it was used as a starting point the MC-based  $I_{CaL}$  from MJ model. At the end of the process, a novel version DTP of the original TP model was generated. Figure 26 shows the schematic representation for this novel version.

Figure 26 – Schematic representation of the novel MC-based ten Tusscher and Panfilov (62) Model (DTP) with the insertion of the MC-based  $I_{CaL}$  model proposed by Mahajan et al. (36).



Source: adapted from CellML (13).

As can be noted by comparing the schematic representation of the original TP model, Figure 20, with the schematic representation of the novel DTP model, Figure 26, the only difference in their mathematics is the substitution of the gating-based equations that drive the original TP  $I_{CaL}$  current opening fraction by the MC-based formulation from the MJ model. This replacement is composed of two primary processes. The first one is the definition of the new MC formulation. Since it will modify the original TP model, it is necessary to do a fitting procedure to recover the original TP model outputs. Section 3.1.1 presents the method used to define the MC topology and rates. Section 3.1.2 presents the method to fit the new MC-based formulation to maintain the original TP outputs.

The method and results obtained in the DTP  $I_{CaL}$  reformulation were extensively tested, and the whole study was published in Novaes et al. (40).

### 3.1.1 DTP $I_{CaL}$ Formulation

Considering that a single generic HH gate  $g$  can assume only two states (O - Open, and C - Close), a two-state Markovian model can be generated for this gate, calculating the transition rates  $g_+$  (rate of the transition  $C \rightarrow O$ ) and  $g_-$  (rate of the transition  $O \rightarrow C$ ) as

$$g_+ = \frac{g_\infty}{\tau_g} \quad (3.4)$$

and

$$g_- = \frac{1 - g_\infty}{\tau_g}, \quad (3.5)$$

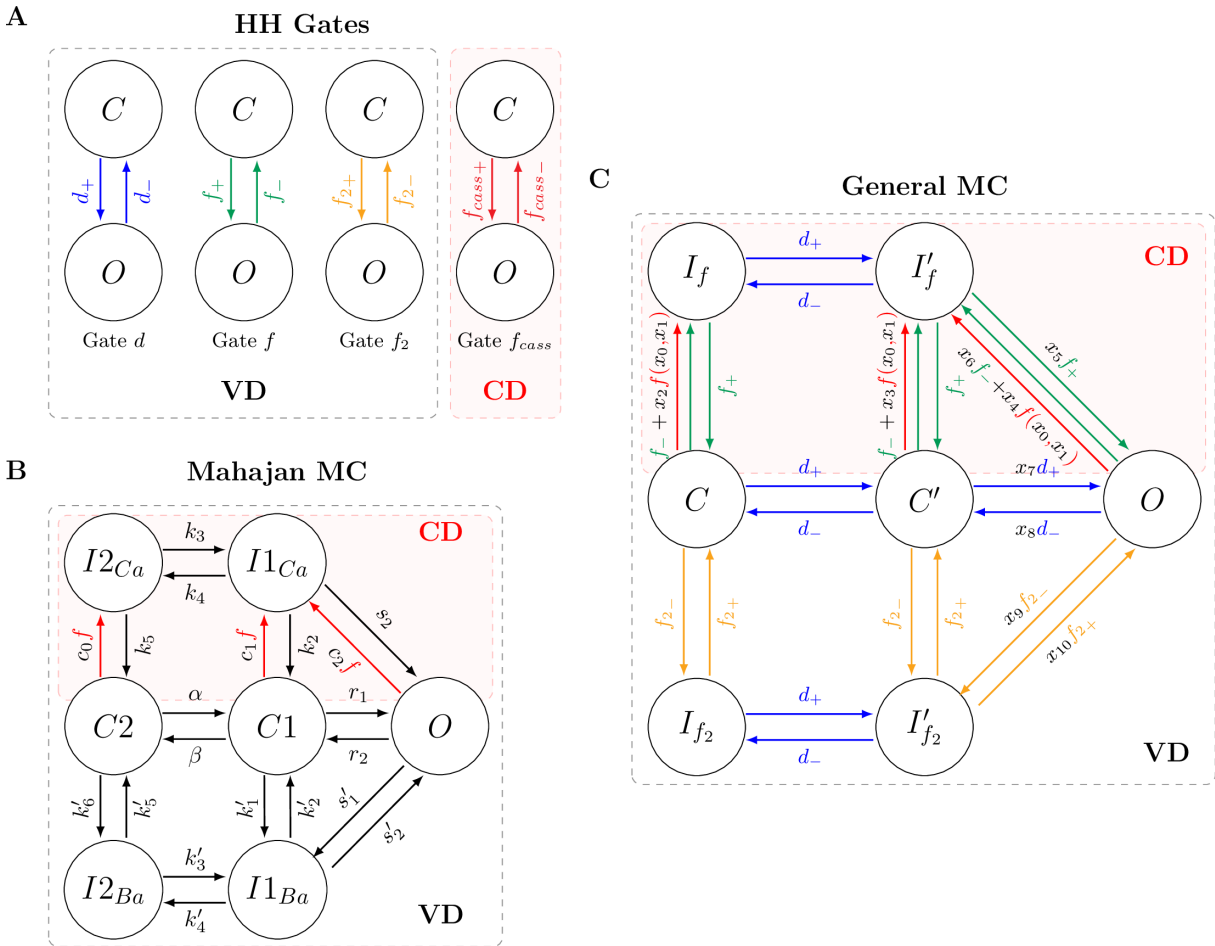
where  $g_\infty$  and  $\tau_g$  are equations defined by the HH Gate-based formalism as described in Section 2.3.1.

As discussed in Section 2.3.3.1, applying this analysis to the four gates from the TP model, it is possible to calculate all the rates that control the dynamics between the Open and Close states for each gate. Figure 27A illustrates these single MCs for each of the four gates and their respective transition rates. The construction of the MC-based  $I_{CaL}$  current for the DTP model was based on these eight transition rates.

Once the transition rates were defined, it was necessary to set the MC topology. This thesis proposition adopted the minimal seven-state MC arrangement proposed by MJ. Figure 27B illustrates the original MJ MC for their  $I_{CaL}$  formulation.

Thus, to transform the original  $I_{CaL}$  current formulations from the Gate-based models into the MC-based, it was combined the rates of the HH formalism, Figure 27A, with the consolidated  $I_{CaL}$  MC-based topology, Figure 27B. This combination has resulted in the proposed MC-based model presented in Figure 27C. In addition, to adjust this new MC-based model to reproduce the original TP human model, there were introduced a set of eleven parameters that multiply some of the MC transition rates:  $\mathbf{x} = \{x_i | x_i \in \mathbb{R} \text{ and } i = 0 - 10\}$ .

Figure 27 – Schematic representations of the three markov chain structures considered in this study. A: The four independent Markov Chains for each gate of the ten Tusscher and Panfilov (62) model considering only two possible states, Open ( $O$ ) and Close ( $C$ ) for each one. B: The original structure of the Markov Chain used by Mahajan et al. (36) to simulate the  $I_{CaL}$  phenomenon. C: The DTP Markov Chain created as a combination of the Hodgkin and Huxley (29) formalism rates and the Mahajan et al. (36) topology, to replace the gates in the ten Tusscher and Panfilov (62) model. The MC transitions generated considering the Hodgkin and Huxley (29) gates  $d$ ,  $f$ , and  $f_2$  are shown respectively in blue, green, and yellow. The calcium-dependent function  $f$  and the rates associated with the calcium concentration are shown in red. The set of parameters  $\alpha$  used to fit both calcium-dependent rates (parameters  $x_0$  to  $x_4$ ) and voltage-dependence rates (parameters  $x_5$  to  $x_{10}$ ) are shown in black.



Source: obtained from Novaes et al. (40).

The first five fitting parameters,  $x_0$  up to  $x_4$ , are used to handle the MC calcium sensitivity. Considering the MC top layer, states  $I_f$  and  $I'_f$ , as the calcium-dependence layer, these five parameters are related to calcium-dependence. The first two parameters,  $x_0$  and  $x_1$ , compose the calcium-dependent equation

$$f(c, x_0, x_1) = \frac{1}{1 + (x_0 \bar{c}_p/c)^{x_1}}, \quad (3.6)$$

originally adapted from the MC proposed by MJ. The other three parameters,  $x_2$ ,  $x_3$ , and  $x_4$ , multiply, respectively, the calcium-dependent function  $f$  presented in the rates  $C \rightarrow I_f$ ,  $C' \rightarrow I'_f$ , and  $O \rightarrow I'_f$ .

Conversely, the voltage-dependence appears in all MC states and rates. The top layer, states  $I_f$  and  $I'_f$ , and the fitting parameters  $x_5$  and  $x_6$  are associated with the voltage dependence behavior of the gate  $f$ ; the bottom layer, states  $I_{f2}$  and  $I'_{f2}$ , and the fitting parameters  $x_9$  and  $x_{10}$  are associated with the voltage dependence behavior of the gate  $f_2$ ; and the main layer, states  $C$ ,  $C'$ , and  $O$ , and the fitting parameters  $x_7$  and  $x_8$  are associated with the voltage dependence behavior of the gate  $d$ . Concerning the fitting process,  $x_5$  and  $x_6$  are used to fit the voltage dependence (top layer); the parameters  $x_9$  and  $x_{10}$  are used to fit the bottom layer, and  $x_7$  and  $x_8$  are used to fit the main layer. To see a more detailed description of the new MC model, please see Appendix A.

### 3.1.2 DTP $I_{CaL}$ Fitting Procedure

In Section 3.1.1, it was proposed an MC-based model to use in the  $I_{CaL}$  formulation for the TP model replacing the gate-based opening fraction equations. Next, adjusting the MC fitting parameters set  $\boldsymbol{x}$  is necessary to reproduce the original outputs.

The fitting procedure has one primary objective: to find the eleven parameters  $x_i$  that make the Opening fraction of the new MC-based model able to reproduce the original Gate-based opening values. As it replaced the  $I_{CaL}$  Opening fraction, once its dynamics are recovered, it also recovers the  $I_{CaL}$  current and, consequently, all the other model outputs, such as the AP and intracellular calcium outputs.

As can be seen in Equation 3.2, the multiplication  $df f_2 f_{cass}$  determines the Opening fraction,  $O_f$ , for the TP model. The curves generated by this model are shown in Figure 25A.

The goal is to replace these opening fraction terms with the proposed MC-based open state and find a parameter set  $\boldsymbol{x}$  capable of recovering the original model outputs. So, this process can be seen as a minimization problem where the objective is to find the best set of parameters  $\boldsymbol{x}$  that minimizes the error between the new MC-based  $I_{CaL}$  curve of the DTP model and the original TP. As a minimization problem, it is necessary to choose the objective function, or fitness function,  $F$ . The target was defined as the  $I_{CaL}$  curve of the eleventh pulse (after a series of stimulated AP pulses). So, for each individual, or candidate set  $\boldsymbol{x}$ , the  $F$  function reads

$$F(\boldsymbol{x}) = \sqrt{\sum_{t=10s}^{11s} \frac{(I_{CaL_{MC}}(\boldsymbol{x}, t) - \overline{I_{CaL_{TP}}}(t))^2}{\overline{I_{CaL_{TP}}}(t)^2}}, \quad (3.7)$$

where  $\overline{I_{CaL_{TP}}}$  is the calcium current of the TP gate-based model, and the  $I_{CaL_{MC}}$  is the calcium current generated by the new MC-based model using the parameter set  $\boldsymbol{x}$ . To

obtain the  $I_{CaL}$  curves for both DTP, and TP models, they were simulated using a pacing of 1Hz.

To solve the optimization problem, it was used the Differential Evolution (DE) algorithm available in the **Python** library **Pygmo** (8). In the DE field, each set of parameters  $\boldsymbol{x}$  is labeled as an individual or possible solution. Moreover, a set of individuals, or solutions, is labeled as a population. The primary purpose of an evolutionary algorithm as DE is to begin from a random initial population and, generations over generations, to evolve this population to find individuals, or solutions, that better solve the minimization problem. For more details about the DE algorithm, please see Price (47).

To execute the DE, the population size was set to 100 individuals, and, to generate the initial population used by the algorithm, it was used the Latin Hypercube method available in **Python** library **SMT** (9). The number of generations of the algorithm was set to 50. So, at the end of the DE execution, it will have  $50 \times 100$  possible solutions. The optimization algorithm is constrained by imposing limits for each one of the parameter. The search space  $\mathbb{S}$  for the parameters was set as  $\mathbb{S} = \{\mathbb{S} \subset \mathbb{R}^{11} | 0.1 \leq s_i \leq 5.9\}$ , where  $s_i$  is the search space of the respective parameter  $x_i$ . All the other algorithm settings were adopted as the standard values implemented by the **Pygmo** library. To see more details about its settings, please see Biscani et al. (8).

### 3.1.3 Definition of a Calcium Release Unit in DTP Model

Considering the DTP model presented in this Section, one single CRU comprises the main structures involved in the CICR process. So, each CRU has its own ionic currents:  $I_{CaL}$ ,  $I_{rel}$ ,  $I_{up}$ ,  $I_{leak}$ ,  $I_{xfer}$ ,  $I_{bCa}$ ,  $I_{pCa}$ , and the  $I_{NaCa}$ ; and its own calcium concentrations:  $[Ca]_i$ ,  $[Ca]_{ss}$  and the  $[Ca]_{SR}$ . At this point, it can be adopted the notation  $I_\bullet^u$  and  $[Ca]_\bullet^u$  to represent the ionic currents and the calcium concentrations belonging locally to the CRU  $u$ .

In summary, considering the scope of the DTP model, Table 1 presents the description of the structures that compose a single CRU  $u$ .

Table 1 – Structures of the MC-based version of the ten Tusscher and Panfilov (62) model that compose a single CRU  $u$ .

$\text{Ca}^{2+}$ Currents	Description
$I_{CaL}^u$	L-Type Calcium Current
$I_{rel}^u$	Ryanodine Receptors Release Current
$I_{up}^u$	SERCA pump
$I_{leak}^u$	Small SR Leak Current
$I_{xfer}^u$	Calcium Flux From the $[Ca]_{ss}$ to $[Ca]_i$
$I_{bCa}^u$	Transmembrane $\text{Ca}^{2+}$ Background Current
$I_{pCa}^u$	Transmembrane $\text{Ca}^{2+}$ Pump Current
$I_{NaCa}^u$	Sodium-Calcium Transmembrane Exchanger

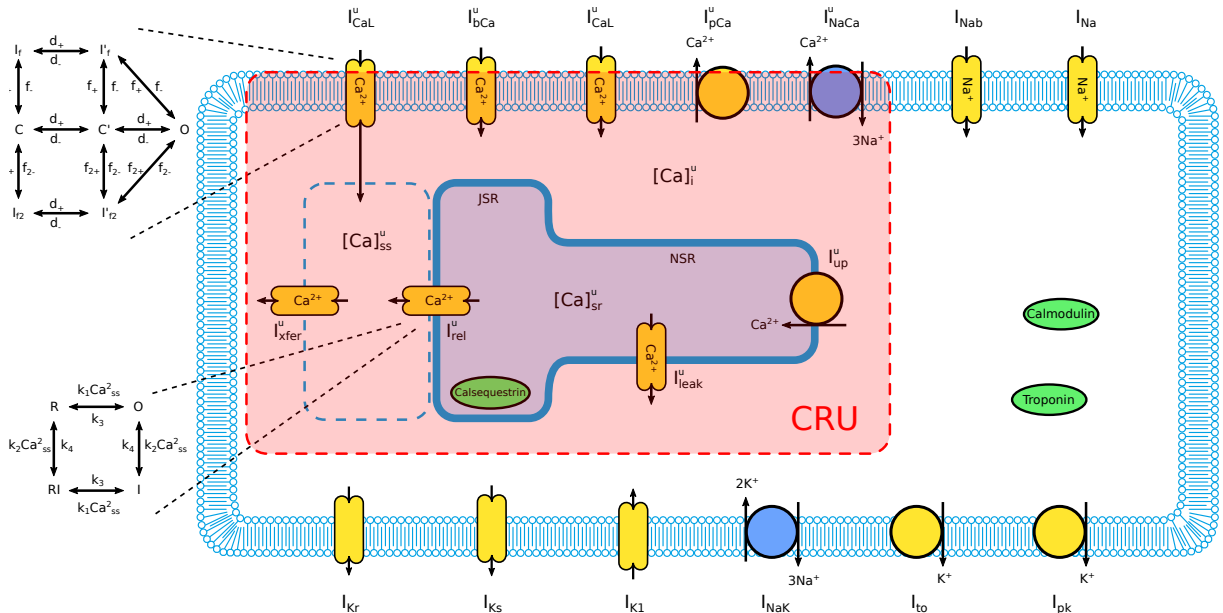
  

$\text{Ca}^{2+}$ Concentrations	Description
$[Ca]_i^u$	Intracellular Calcium Concentration
$[Ca]_{ss}^u$	Subspace Calcium Concentration
$[Ca]_{SR}^u$	Sarcoplasmic Reticulum Calcium Concentration

Source: Created by the author. (2023).

Figure 28 presents an illustration of the DTP model highlighting the single CRU present in it.

Figure 28 – Schematic representation of the novel MC-based ten Tusscher and Panfilov (62) Model highlighting, in red, the structures that compose a single CRU  $u$ .



Source: adapted from CellML (13).

Another important definition of a CRU is the amount of LCCs and RyRs inside it. Although each CRU has only one representation of the  $I_{CaL}$  and  $I_{RyR}$  current, each

respective current is the result of a cluster of many channels (66). Considering a human left ventricle myocyte, the amount of LCCs inside each CRU varies from 2 to 10, and the amount of RyRs varies from 10 to 50 (3, 30, 23, 33). In terms of notation, mathematically, it could be written that the number of LCCs inside the CRU  $u$  is

$$N_{LCC}^u = \{l \in \mathbb{N} | 2 \leq l \leq 10\}, \quad (3.8)$$

and the number of RyRs inside the same CRU  $u$  is

$$N_{RyR}^u = \{r \in \mathbb{N} | 10 \leq r \leq 40\}. \quad (3.9)$$

Thus, it is crucial to introduce these variables in the DTP model in order to make it capable of simulating the variations in these values. For that, a modification of the local  $I_{CaL}^u$  and  $I_{rel}^u$  mathematics is necessary.

Considering a single CRU  $u$ , the initial equations for the local  $I_{CaL}^u$  and  $I_{rel}^u$  currents reads

$$I_{CaL}^u = O_f^u_{LCC} \times G_{CaL} \frac{4(V^u - 15)F^2}{RT} \frac{0.25[Ca]_{ss}^u e^{2(V^u - 15)F/RT} - [Ca^{2+}]_o}{e^{2(V^u - 15)F/RT} - 1}, \quad (3.10)$$

and

$$I_{rel}^u = O_f^u_{RyR} \times V_{rel}([Ca]_{SR}^u - [Ca]_{ss}^u) \quad (3.11)$$

where  $O_f^u_{LCC}$  and  $O_f^u_{RyR}$  represents the respective opening fractions of the LCCs and RyRs inside the CRU  $u$ . This initial assumption can adequately describe an infinite number of those channels since  $O_f^u$  represents the total channels opening fraction. However, it is not the most appropriate to describe a real myocyte since this cell has a finite number of LCCs and RyRs. To introduce these finite values into the Equations 3.10 and 3.11, the new  $I_{CaL}^u$  and  $I_{rel}^u$  mathematics became

$$I_{CaL}^u = \frac{O_{LCC}^u}{N_{LCC}^u} \times G_{CaL} \frac{4(V^u - 15)F^2}{RT} \frac{0.25[Ca]_{ss}^u e^{2(V^u - 15)F/RT} - [Ca^{2+}]_o}{e^{2(V^u - 15)F/RT} - 1}, \quad (3.12)$$

and

$$I_{rel}^u = \frac{O_{RyR}^u}{N_{RyR}^u} \times V_{rel}([Ca]_{SR}^u - [Ca]_{ss}^u) \quad (3.13)$$

where, in this new formulation,  $O_{LCC}^u$  and  $O_{RyR}^u$  represent, respectively, the absolute finite number of LCCs and RyRs in the Open state inside the CRU  $u$ .

With the insertion of the variables  $O_{LCC}^u$  and  $O_{RyR}^u$  in the DTP model, it became capable of simulating experiments under a multiscale approach since it is possible to vary the number of channels that compose each CRU  $u$ . In this way, it is expected to reproduce the micro scale when using a small number of ion channels. As soon as these values are increased, the simulations might reproduce the macro scales.

Nevertheless, when using DTP to simulate microscale experiments, one crucial feature remains to be implemented in the model: stochasticity. Section 3.1.4 presents the method used to insert the stochasticity feature in the DTP and, thus, the generation of the Stochastic version of the model. This Stochastic version is labeled as STP.

### 3.1.4 DTP Stochastic Version

Up to this point, although the DTP model can perform simulations considering small quantities of LCCs and RyRs acting in the CICR process, it still needs to consider the stochasticity encountered in the micro scale since all its formulations are composed of deterministic algebraic equations. Regarding that this study has the objective of proposing a novel computational model capable of simulating the phenomena associated with the CICR process on a micro scale, this stochasticity feature must be present in the model formulation. In this way, Random Variables were used to replace strategic formulations of the DTP model directly associated with the CICR process.

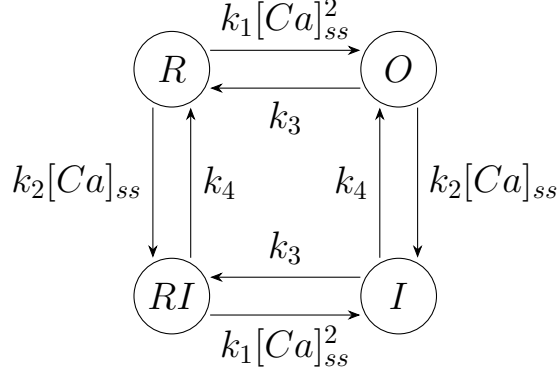
For that, there were selected the formulations of the two Markov Chains existing in the model, the  $I_{CaL}^u$  and the  $I_{rel}^u$ , that are associated, respectively, with the L-type Calcium Channels and Ryanodine Receptors. All the transitions between the states that compose the respective MCs were replaced by stochastic formulations based on Random Variables. To describe this replacement, let us take the  $I_{rel}$  MC formulation.

As written in Equation 3.13, the  $I_{rel}^u$  mathematics reads

$$I_{rel}^u = \frac{O_{RyR}^u}{N_{RyR}^u} \times V_{rel}([Ca]_{SR}^u - [Ca]_{ss}^u),$$

where  $O_{RyR}^u$  is the number of RyR in the Open state,  $N_{RyR}^u$  is the total number of RyR channels,  $V_{rel}$  is the velocity of the ion release,  $[Ca]_{SR}^u$  is the Sarcoplasmic Reticulum Calcium concentration, and  $[Ca]_{ss}^u$  is the Dyadic Subspace Calcium concentration. This open state expressed by the variable  $O_{RyR}^u$  is part of a four-state MC that controls all the current dynamics. The MC is composed by the  $I$  state that represents an Inactivated closed state, the  $R$  state that represents a Resting closed state, the  $RI$  that represents a Resting Inactivated closed state, and the  $O$  that represents the Open conducting state. Figure 29 presents an illustration of the four-state MC and its transitions used to represent the dynamics of the RyR channels conformation.

Figure 29 – Four-state Markov Chain used to represent the states that the RyR channels can assume. The state  $I$  represents an Inactivated closed state, the state  $R$  represents a Resting closed state, the state  $RI$  represents a Resting Inactivated closed state, and the state  $O$  represents the Open conducting state.



Source: adapted from ten Tusscher and Panfilov (62).

All the dynamics of the four-state MC can be described by four ODEs that calculate the variation of the number of channels in each state. The equations for this variation over the time of each state reads

$$\frac{dI}{dt} = k_1[Ca]_{ss}^2 RI + k_2[Ca]_{ss} O - k_3 I - k_4 I, \quad (3.14)$$

$$\frac{dR}{dt} = k_3 O + k_4 RI - k_1[Ca]_{ss}^2 R - k_2[Ca]_{ss} R, \quad (3.15)$$

$$\frac{dRI}{dt} = k_2[Ca]_{ss} R + k_3 I - k_1[Ca]_{ss}^2 RI - k_4 RI, \quad (3.16)$$

$$\frac{dO}{dt} = k_1[Ca]_{ss}^2 R + k_4 I - k_2[Ca]_{ss} O - k_3 O; \quad (3.17)$$

where  $[Ca]_{ss}$  is the Dyadic Subspace calcium concentration and  $k_\bullet$  are the transition rates parameters.

One of the intrinsic features of this kind of MC model is the mass conservation law. Mathematically, it can be noticed by summing all the derivative equations and seeing that the result must be zero. Considering the whole MC system, it means that the total number of elements present over all states is preserved. Regarding this feature in the ionic channels context, it makes sense since the total number of channels does not change. The total number of ionic channels must be preserved while their state must change.

In this way, each ODE that composes the four-state MC model can be seen as a summation of the ionic channels that change their conformation for the characterized state (positive terms) and ionic channels that changed their conformation from the represented state (negative terms) in a fraction of time  $dt$ . To illustrate, let us use the Open state ODE. According to Equation 3.17, the Open state ODE comprises two positive and two negative terms. The first and second positive terms represent the number of channels that

changed their state from the  $R$  state, and from the  $I$  state to the  $O$  state. Conversely, the two negative terms represent the number of channels that changed their state from the  $O$  state to the  $I$  and  $R$  state. Visually, it can be written as

$$\overbrace{\frac{dO}{dt}}^{\text{variation of the channels in } O \text{ state by } dt} = \overbrace{k_1[Ca]_{ss}^2 R}^{\text{channels from } R \text{ state}} + \overbrace{k_4 I}^{\text{channels from } I \text{ state}} - \overbrace{k_2[Ca]_{ss} O}^{\text{channels to } I \text{ state}} - \overbrace{k_3 O}^{\text{channels to } R \text{ state}}. \quad (3.18)$$

As with any other ODE, the Open state derivative can be solved by applying the Explicit Euler Method. In addition, as with any deterministic Initial Value Problem, the Euler method will always generate the same output results if applied using the same initial value. Considering the macro scale, in other words, the clustering of several channels in a single representation, this deterministic solution is feasible since the average obtained by this clustering must generate the same outputs. However, this deterministic feature must give way to the stochastic nature on a micro scale.

Therefore, to introduce this stochastic nature into the MC model, its ODEs formulations were rewritten replacing the deterministic terms with Binomial random variables. In a general view, a Binomial random variable represents the number of successes  $x$  in  $n$  repeated trials of a binomial experiment\*. Mathematically, a generic Binomial random variable  $\delta$  can be written as

$$\delta = \text{Binomial}(p, n), \quad (3.19)$$

where  $p$  is the probability to have success, and  $n$  in the number trials.

In this way, each term that composes the ODEs of the MC model can be rewritten as a Binomial random variable that represents the Binomial experiment where the number of trials is the number of ionic channels in the chance to do a transition, and the probability of having success, or doing the transition by the period of  $dt$  time, is a multiplication of the transition rate by the value of  $dt$ .

Let us take the Open state ODE to illustrate this exchange of the deterministic terms by the stochastic ones. From Equation 3.17, its ODE reads

$$\frac{dO}{dt} = k_1[Ca]_{ss}^2 R + k_4 I - k_2[Ca]_{ss} O - k_3 O.$$

Rearranging the terms, the same Equation can be written as

$$dO = (k_1[Ca]_{ss}^2 \times dt)R + (k_4 \times dt)I - (k_2[Ca]_{ss} \times dt)O - (k_3 \times dt)O. \quad (3.20)$$

---

\*A binomial experiment is a statistical trial characterized by two possible outcomes, typically referred to as "success" and "failure." It involves a fixed number of independent and identical trials, each with the same probability of success.

where  $dO$  represents explicitly a number of channels that varied around the Open state during  $dt$  time.

So, the stochastic version for the same variable  $dO$ , number of channels that varied around the Open state during  $dt$  time, can be written as

$$\Delta O = \delta_{RO} + \delta_{IO} - \delta_{OI} - \delta_{OR}, \quad (3.21)$$

where  $\Delta O$  is the total number of channels that varied around the  $O$  state;  $\delta_{RO}$  is the Binomial random variable that represents the number of channels that change their state from  $R$  to  $O$ , calculated as

$$\delta_{RO} = \text{Binomial}(k_1 [Ca]_{ss}^2 \times dt, R); \quad (3.22)$$

$\delta_{IO}$  is the Binomial random variable that represents the number of channels that change their state from  $I$  to  $O$ , calculated as

$$\delta_{IO} = \text{Binomial}(k_4 \times dt, I); \quad (3.23)$$

$\delta_{OI}$  is the Binomial random variable that represents the number of channels that change their state from  $O$  to  $I$ , calculated as

$$\delta_{OI} = \text{Binomial}(k_2[Ca]_{ss} \times dt, O); \quad (3.24)$$

and  $\delta_{OR}$  is the Binomial random variable that represents the number of channels that change their state from  $O$  to  $R$ , calculated as

$$\delta_{OR} = \text{Binomial}(k_3 \times dt, O). \quad (3.25)$$

Visually, the Equation 3.21 can be written as

$$\text{variation of channels in } O \text{ state by } dt = \overbrace{\Delta O}^{\text{channels from } R \text{ state}} + \overbrace{\delta_{IO}}^{\text{channels from } I \text{ state}} - \overbrace{\delta_{OI}}^{\text{channels to } I \text{ state}} - \overbrace{\delta_{OR}}^{\text{channels to } R \text{ state}}. \quad (3.26)$$

The insertion of the stochastic nature into the CICR process modeled by the DTP model was done by applying this approach using Binomial random variables in the four-state MC formulations used to simulate the  $I_{rel}$  current, and in the seven-state MC formulations used to simulate the  $I_{CaL}$  current. After that, the Stochastic version of the model, the STP model, was defined.

### 3.1.5 Spatial Model Version

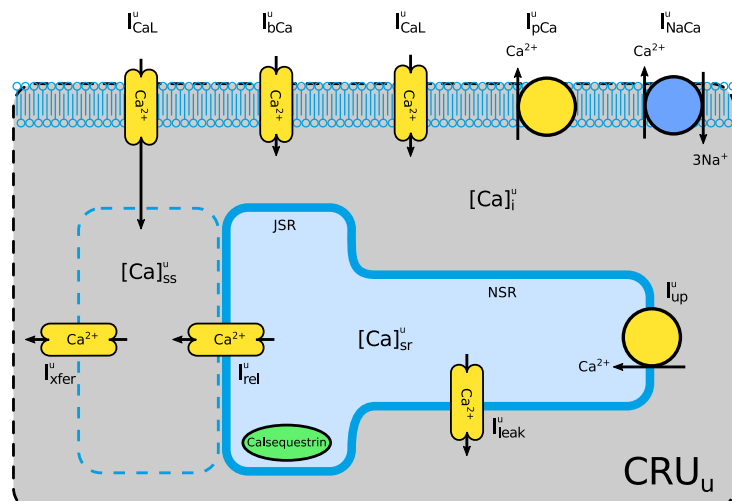
The simulations performed by the STP model can give insight into how the stochasticity may behave as soon as the parameters alter between the extremes scale, the micro, and the macro scale. This conversion is conducted by increasing the number of

LCCs and RyRs inside the CRU. However, considering this thesis focuses on the CICR process, ionic diffusion is another essential factor that has a role in this process.

As the STP model consider only one CRU, it merges all the LCCs and RyRs in a single structure and, consequently, in a single representation of the respective currents  $I_{CaL}$  and  $I_{RyR}$ . To illustrate this condition's limitation, considering the arrangement obtained using the single CRU with 4 LCCs and 20 RyRs for the whole cell is distant from a natural scenario (2, 3, 32). However, these values of LCCs and RyRs are appropriate values to compose the single CRU. The mistake appears in considering one single CRU.

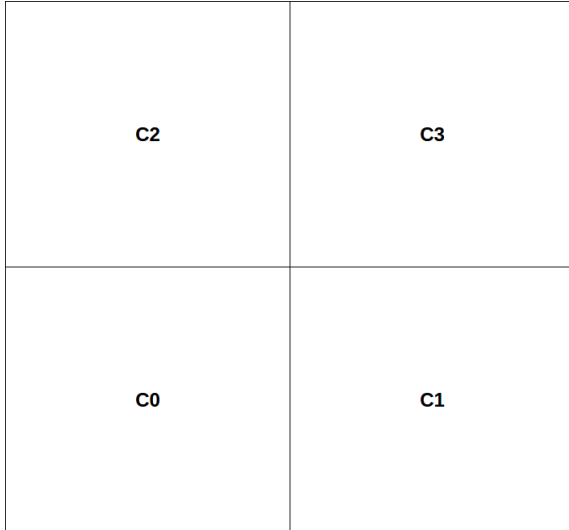
To avoid this mistake, it was created a spatial version of the STP model composed of a two-dimensional grid of NxN CRUs. Using this NxN grid, the computational model, as a whole, became composed of  $N^2$  CRUs, with, as described in Section 3.1.3, each CRU  $u$  having its variables. Figure 30 presents an illustration of the structures that compose a CRU, and Figure 31 shows an illustration of different NxN CRUs grid conformations.

Figure 30 – Schematic representation a single CRU  $u$  that compose the STP model.

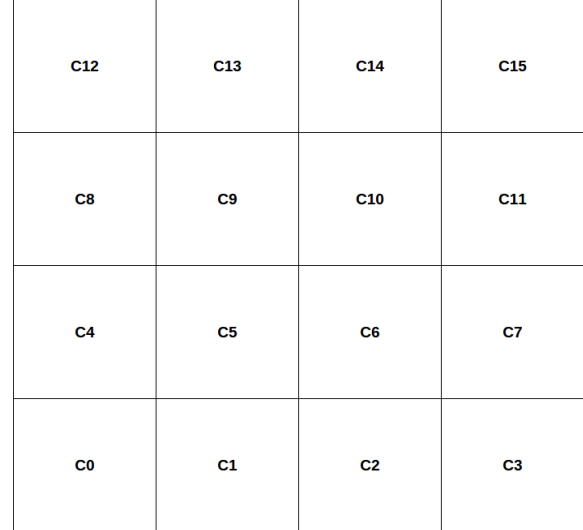


Source: adapted from CellML (13).

Figure 31 – Illustrations of different NxN CRUs Grid conformations.



(a) 2x2 CRUs Grid Conformation



(b) 4x4 CRUs Grid Conformation

C56	C57	C58	C59	C60	C61	C62	C63
C48	C..	C..	C..	C..	C..	C..	C55
C40	C..	C..	C..	C..	C..	C..	C47
C32	C..	C..	C..	C..	C..	C..	C39
C24	C..	C..	C..	C..	C..	C..	C31
C16	C..	C..	C..	C..	C..	C..	C23
C8	C..	C..	C..	C..	C..	C..	C15
C0	C1	C2	C3	C4	C5	C6	C7

(c) 8x8 CRUs Grid Conformation

C240	C241	C242	C243	C244	C245	C246	C247	C248	C249	C250	C251	C252	C253	C254	C255
C224	C..	C239													
C208	C..	C223													
C192	C..	C207													
C176	C..	C191													
C160	C..	C175													
C144	C..	C159													
C128	C..	C143													
C112	C..	C127													
C96	C..	C111													
C80	C..	C95													
C64	C..	C79													
C48	C..	C63													
C32	C..	C47													
C16	C..	C31													
C0	C1	C2	C3	C4	C5	C6	C7	C8	C9	C10	C11	C12	C13	C14	C15

(d) 16x16 CRUs Grid Conformation

Source: Created by the author. (2023).

Other important definitions are the local and global variables. Since the model is composed of a NxN grid of CRUs and each CRU  $u$  is composed of a set of variables as, for instance, the  $I_{CaL}^u$  current, let us assume each one of these values as local variables. Meanwhile, a global value of these variables is necessary to calculate the others composing the model, such as the AP. So, in this way, the global variables were defined as the average of all local values.

To exemplify the correlation between the local and the global variables, let us use

the AP equation. The AP equation of the STP model reads

$$\frac{dV}{dt} = -\frac{I_{Na} + I_{K1} + I_{to} + I_{Kr} + I_{Ks} + I_{bNa} + I_{pK} + I_{NaK} + \overbrace{I_{CaL} + I_{NaCa} + I_{pCa} + I_{bCa}}^{\text{calcium-dependent}}}{C_m}. \quad (3.27)$$

To facilitate the visualization, the Equation 3.27 can be separated into two parts considering the calcium dependence of the currents. In this way, the currents are separated as currents that are inside the CRUs or not. So, the same equation can be displayed as

$$\frac{dV}{dt} = -\frac{I_{Na} + I_{K1} + I_{to} + I_{Kr} + I_{Ks} + I_{bNa} + I_{pK} + I_{NaK} + \overbrace{I_{CaL} + I_{NaCa} + I_{pCa} + I_{bCa}}^{\text{calcium-dependent}}}{C_m}, \quad (3.28)$$

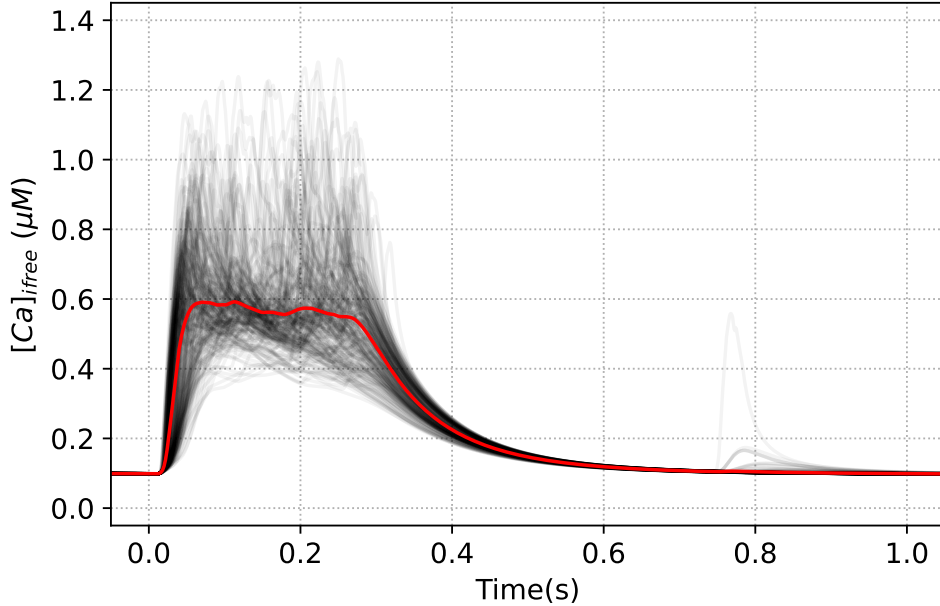
where  $I_{CaL}$ ,  $I_{NaCa}$ ,  $I_{pCa}$  and  $I_{bCa}$  are, respectively, the global values of the L-type Calcium Current, Sodium-Calcium exchanger, Calcium pump and the Background Calcium current. These global values are calculated as

$$I_{CaL} = \frac{1}{N^2} \sum_{u=1}^{N^2} I_{CaL}^u \quad (3.29) \qquad I_{NaCa} = \frac{1}{N^2} \sum_{u=1}^{N^2} I_{NaCa}^u \quad (3.30)$$

$$I_{pCa} = \frac{1}{N^2} \sum_{u=1}^{N^2} I_{pCa}^u \quad (3.31) \qquad I_{bCa} = \frac{1}{N^2} \sum_{u=1}^{N^2} I_{bCa}^u \quad (3.32)$$

where the currents  $I_{\bullet}^u$  are the local values of the current  $I_{\bullet}$  within the CRU  $u$ . To illustrate the relation between the local and global values, Figure 32 presents the traces of all local  $[Ca]_i^u$  traces compared with their global value obtained from a 16x16 grid simulation.

Figure 32 – Comparison between all 256 local  $[Ca]_{i\ free}^u$  traces (black lines) alongside the global  $[Ca]_{i\ free}$  (red line).



Source: Created by the author. (2023).

The same approach was used for the whole model equations, where an interface between the local and global calculations was necessary. In conclusion, it will be used the notation  $\bullet^u$  for the local value of the variable  $\bullet$ .

The NxN grid conformation also allows to insert the ionic diffusion into the model. Since it represents a spatial distribution of the CRUs, it is reasonable to implement the diffusion of the calcium ions within these units.

### Diffusion Flux

The implementation of the NxN grid of CRUs allows to analyze the effects of the calcium diffusion on the whole model behavior.

The original TP model and, consequently, the STP version proposed in this thesis have defined three calcium concentrations: Intracellular Calcium Concentration ( $[Ca]_i$ ), Sarcoplasmic Reticulum Calcium Concentration ( $[Ca]_{SR}$ ), and Diadic Subspace Concentration ( $[Ca]_{ss}$ ). These variables have total concentrations, free plus buffered concentrations. Mathematically, algebraic equations correlate the total, the buffered, and the free portions of these concentrations. These equations reads

$$\begin{cases} [Ca]_{i\ buff} = \frac{[Ca]_i \times Buf_i}{[Ca]_i + K_{bufi}}, \\ [Ca]_i = [Ca]_{i\ free} + [Ca]_{i\ buff}, \end{cases} \quad (3.33)$$

$$\begin{cases} [Ca]_{SR\ buff} = \frac{[Ca]_{SR} \times Buf_{sr}}{[Ca]_{SR} + K_{bufsr}}, \\ [Ca]_{SR} = [Ca]_{SR\ free} + [Ca]_{SR\ buff}, \end{cases} \quad (3.34)$$

$$\begin{cases} [Ca]_{ss\ buff} = \frac{[Ca]_{ss} \times Buf_{ss}}{[Ca]_{ss} + K_{bufss}}, \\ [Ca]_{ss} = [Ca]_{ss\ free} + [Ca]_{ss\ buff}. \end{cases} \quad (3.35)$$

The diffusion term was implemented only in the Intracellular and the Sarcoplasmic

Reticulum Calcium Concentrations of each CRU  $u$ , respectively,  $[Ca]_i^u$  and  $[Ca]_{SR}^u$ . It was considered that the free Diadic Subspace Calcium concentrations, the  $[Ca]_{ss}^u$ , are local values and affect only the structures within its CRU.

Based on the original model, the equations for the local variables  $[Ca]_i^u$  and  $[Ca]_{SR}^u$  are

$$\frac{d[Ca]_i^u}{dt} = -\frac{I_{bCa}^u + I_{pCa}^u - 2I_{NaCa}^u}{2V_c F} + \frac{V_{sr}}{V_c} (I_{leak}^u - I_{up}^u) + I_{xfer}^u \quad (3.36)$$

and

$$\frac{d[Ca]_{SR}^u}{dt} = (I_{up}^u - I_{leak}^u - I_{rel}^u). \quad (3.37)$$

With the implementation of the two-dimensional grid, besides the time variation, the  $[Ca]_i^u$  and  $[Ca]_{SR}^u$  dynamics had two more spatial variables, the x-axis, and the y-axis. This way, the Equations 3.36 and 3.37 became Partial Differential Equations (PDE) and, with the addition of the diffusion term  $\nabla \cdot J_\bullet^u$ , the updated mathematics for the respective equations reads

$$\frac{\partial [Ca]_i^u}{\partial t} = -\frac{I_{bCa}^u + I_{pCa}^u - 2I_{NaCa}^u}{2V_c F} + \frac{V_{sr}}{V_c} (I_{leak}^u - I_{up}^u) + I_{xfer}^u - \nabla \cdot \mathbf{J}_i^u \quad (3.38)$$

and

$$\frac{\partial [Ca]_{SR}^u}{\partial t} = (I_{up}^u - I_{leak}^u - I_{rel}^u) - \nabla \cdot \mathbf{J}_{SR}^u. \quad (3.39)$$

where  $\mathbf{J}_i^u = -D_i^u \nabla [Ca]_i^u$ ,  $\mathbf{J}_{SR}^u = -D_{SR}^u \nabla [Ca]_{SR}^u$ . In this thesis, the diffusion factors  $D_i^u$  and  $D_{SR}^u$  were defined as both being isotropic. So,  $D_i^u = D_{i,x}^u = D_{i,y}^u$  and  $D_{SR}^u = D_{SR,x}^u = D_{SR,y}^u$ . Besides this, both diffusion factors were defined as uniform over the whole two-dimensional grid. So,  $D_i^u = D_i$  and  $D_{SR}^u = D_{SR}$ .

Thus, the  $[Ca]_i^u$  Equation (3.38) can be rewritten as

$$\begin{aligned} \frac{\partial [Ca]_i^u}{\partial t} &= -\frac{I_{bCa}^u + I_{pCa}^u - 2I_{NaCa}^u}{2V_c F} + \frac{V_{sr}}{V_c} (I_{leak}^u - I_{up}^u) + I_{xfer}^u + D_i \nabla \cdot \nabla [Ca]_i^u. \\ &= -\frac{I_{bCa}^u + I_{pCa}^u - 2I_{NaCa}^u}{2V_c F} + \frac{V_{sr}}{V_c} (I_{leak}^u - I_{up}^u) + I_{xfer}^u + D_i \Delta [Ca]_i^u. \end{aligned} \quad (3.40)$$

From Equation 3.33, the variable  $[Ca]_i^u$  can be replace by the sum  $[Ca]_{i,free}^u + [Ca]_{i,buf}^u$ . Thus, Equation 3.40 can be rewritten as

$$\frac{\partial [Ca]_i^u}{\partial t} = -\frac{I_{bCa}^u + I_{pCa}^u - 2I_{NaCa}^u}{2V_c F} + \frac{V_{sr}}{V_c} (I_{leak}^u - I_{up}^u) + I_{xfer}^u + D_i \Delta ([Ca]_{i,free}^u + [Ca]_{i,buf}^u). \quad (3.41)$$

According to the Additivity Property of the Laplacian operator, Equation 3.41 can be rewritten as

$$\frac{\partial [Ca]_i^u}{\partial t} = -\frac{I_{bCa}^u + I_{pCa}^u - 2I_{NaCa}^u}{2V_c F} + \frac{V_{sr}}{V_c} (I_{leak}^u - I_{up}^u) + I_{xfer}^u + D_i \Delta [Ca]_{i,free}^u + D_i \Delta [Ca]_{i,buf}^u. \quad (3.42)$$

In this way, Equation 3.42 presents the  $[Ca]_i^u$  time variation in the function of the ionic currents and the diffusion terms. Concerning diffusion terms, they represent the diffusion of two portions that compose the intracellular calcium concentration: the free and the buffered calcium. However, once the buffered portion of calcium ions are bonded to specific proteins, they do not diffuse over the cell. Thus, inserting this physical condition into Equation 3.42, it became

$$\begin{aligned} \frac{\partial [Ca]_i^u}{\partial t} &= -\frac{I_{bCa}^u + I_{pCa}^u - 2I_{NaCa}^u}{2V_c F} + \frac{V_{sr}}{V_c} (I_{leak}^u - I_{up}^u) + I_{xfer}^u + \\ &\quad + D_i \Delta [Ca]_{i free}^u + \underbrace{D_i \Delta [Ca]_{i buff}^u}_0 \\ &= -\frac{I_{bCa}^u + I_{pCa}^u - 2I_{NaCa}^u}{2V_c F} + \frac{V_{sr}}{V_c} (I_{leak}^u - I_{up}^u) + I_{xfer}^u + D_i \Delta [Ca]_{i free}^u \end{aligned} \quad (3.43)$$

Finally, Equation 3.43 was the final Equation used to represent the  $[Ca]_i^u$  dynamics in the two-dimensional version of the STP model. In an analog description, it can be deduced that the final Equation for the  $[Ca]_{SR}^u$  dynamics reads

$$\frac{\partial [Ca]_{SR}^u}{\partial t} = (I_{up}^u - I_{leak}^u - I_{rel}^u) + D_{SR} \Delta [Ca]_{SR free}^u. \quad (3.44)$$

For both  $[Ca]_i^u$  and  $[Ca]_{SR}^u$  PDEs, it was considered the Neumann Boundary condition. Mathematically it reads

$$\nabla [Ca]_i^u \cdot n = 0 \quad (3.45) \qquad \nabla [Ca]_{SR}^u \cdot n = 0, \quad (3.46)$$

where  $n$  is the unit normal vector pointing outward from the boundary.

### 3.2 Simulation Experiments

As a multiscale model, the novel ten Tusscher and Panfilov (62) model proposed by this thesis and presented in Section 3.1 must be capable of performing simulations both on macro and micro scales. For that, it is required to define these two scenarios in this thesis scope.

As mentioned in Section 1, this thesis is focused on the intracellular calcium dynamics represented by the CICR process. So, in this context, the macro scale must present the CICR process and its main variables at a cellular level. For that, the DTP model results will be adopted as the reference values for this scale. It was defined considering that it is a well-accepted cellular model widely used in the literature, even for higher scales such as tissue simulations. Conversely, the micro scale scenario must present the stochastic nature of the ionic channels and, thus, the stochastic nature of the whole CICR process. The stochasticity presented at this level might lead to the critical phenomena of

the Spontaneous Sparks (Section 2.2.4). As reference values at this micro scale model, some values obtained in the literature were considered.

Since the novel MC-based model proposed in this thesis can simulate the ionic channels in different states of conformation, it must be capable of reproducing the local ionic channel behaviors and their stochasticity as observed on micro scale. Furthermore, as soon as some specific model variables assume values from a macro scale scenario, the same model must be capable of reproducing the reference results expected at this level.

Simulations were performed in two conditions to see this central feature of the proposed STP model. The first condition is considering that a cell is composed of only one CRU. To create a pattern in the labels, the label “1x1” will be used to refer to this first condition. In the second condition, it was considered that a cell is composed of a two-dimensional grid of NxN CRUs. Sections 3.2.1 and 3.2.2 describes in detail these two conditions of simulations.

### 3.2.1 1x1 CRU Computational Experiments

Considering the novel STP model proposed in this thesis, the condition in which the cell is composed of one single CRU, or 1x1 CRU, is a reproduction of the DTP model but with the stochasticity nature acting in the  $I_{CaL}$  and  $I_{rel}$  currents within the calcium unit. Figure 28 presents a schematic representation of this 1x1 composition showing the single CRU in the red area.

To use this condition to simulate the opposite scales, micro and macro scales, the experiments were performed by varying the number of LCCs inside this single unit, ranging from 1 to 32768, using the rule of doubling the number of LCCs at each set of experiments. So, mathematically, the number of LCCs was ranged as

$$N_{LCC} = \{2^i | i \in \mathbb{N} \text{ and } i = 0 - 15\}. \quad (3.47)$$

Based on literature (6, 50), for each value assumed by the  $N_{LCC}$ , the assigned value of  $N_{RyR}$  was set as

$$N_{RyR} = 5 \times N_{LCC}. \quad (3.48)$$

For each value for  $N_{LCC}$  and, consequently,  $N_{RyR}$ , a set of 110 pulses in a row were simulated using a pacing rate of 1Hz. The first ten pulses were disregarded. This protocol generated a total of 100 pulse outputs for each value assumed by  $N_{LCC}$  and  $N_{RyR}$ .

To quantify the stochasticity obtained in each set of simulations, it was considered the amount of influx of ion calcium from the sarcoplasmic reticulum to the intracellular medium through the  $I_{rel}$  current over the cycle of one second after the stimulation instant. Mathematically, this influx of calcium can be calculated as

$$S(I_{rel}) = \sum_t^{t+1s} I_{rel}(t) \times dt, \quad (3.49)$$

where  $t$  represents the instant the model is stimulated.

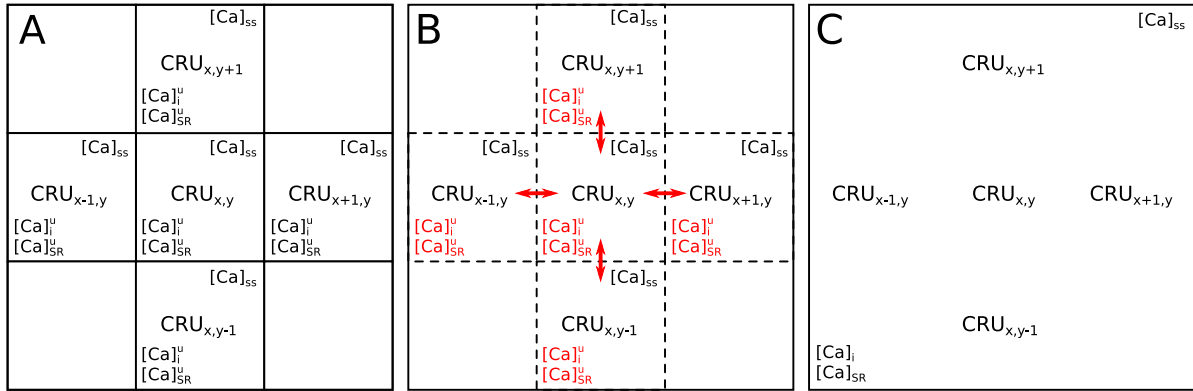
The results of the respective summations  $S(I_{rel})$  are expressed using the descriptive measures of the set of realizations. Besides the variable  $S(I_{rel})$ , the traces of the variables Action Potential (AP), Free Intracellular Calcium Concentration ( $[Ca]_{i\text{free}}^u$ ), L-type Calcium Current ( $I_{CaL}$ ), and the Calcium Release through the RyR ( $I_{rel}$ ), obtained from each one of the 100 pulses, are compared with the DTP model references.

### 3.2.2 NxN CRUs Computational Experiments

Considering that diffusion is an important phenomenon within the CICR process, the two-dimensional version of the STP model were simulated using three distinct conditions for the diffusion factors present in the model.

The first condition was defined as there is no diffusion between the CRUs. In terms of the model, the diffusion terms  $D_i$  and  $D_{SR}$  were set as  $D_i = 0$  and  $D_{SR} = 0$ . In the second condition, the diffusion terms were defined considering biological values obtained from the literature. In this case,  $D_i$  and  $D_{SR}$  diffusion terms were set accordingly to the literature (19) as  $D_i = 0.4\mu m^2/ms$  and  $D_{SR} = 0.12\mu m^2/ms$ . At last, in the third condition, the diffusion effect was implemented considering a hypothetical infinite diffusion. In this case, all the dynamics of the local calcium concentrations must instantly influence the whole CRUs grid, independently of the position (or distance) of the CRUs. This infinite diffusion condition was implemented by merging all the  $[Ca]_{i\text{free}}^u$  and  $[Ca]_{SR\text{free}}^u$  local variables into a single one shared by all CRUs. Mathematically, it could be written as  $[Ca]_{i\text{free}}^u = [Ca]_{i\text{free}}$  and  $[Ca]_{SR\text{free}}^u = [Ca]_{SR\text{free}}$ , where  $[Ca]_{i\text{free}}$  and  $[Ca]_{SR\text{free}}$  are the respective shared variable. In this way, once the local CRU alters the shared variable  $[Ca]_{i\text{free}}$  and  $[Ca]_{SR\text{free}}$ , all the other CRUs feel this variation instantaneously. The labels  $D_0$ ,  $D_R$ , and  $D_\infty$  will be used to characterize each of these three conditions, no-diffusion, realistic diffusion, and infinite diffusion, in the results in Section 4.2.2. Figure 33 shows an illustration of each one of these three diffusion conditions.

Figure 33 – Illustration of the three different diffusion conditions considered in the NxN CRUs grid simulations. (A) No-Diffusion Condition ( $D_0$ ). Each CRU  $u$  has local values for  $[Ca]_{i\ free}^u$  and  $[Ca]_{SR\ free}^u$ . Furthermore, the local dynamics influence only the local CRU. (B) Realistic Diffusion Condition ( $D_R$ ). Each CRU  $u$  has local values for  $[Ca]_{i\ free}^u$  and  $[Ca]_{SR\ free}^u$ . However, the local dynamics influence the local CRU and its adjacent. (C) Infinite Diffusion Condition ( $D_\infty$ ). Each CRU  $u$  share the one single global values for  $[Ca]_{i\ free}$  and  $[Ca]_{SR\ free}$ . So, the local dynamics influence instantly all the CRU grid.



Source: Created by the author. (2023).

In the Results chapter (Chapter 4), the outputs obtained by the spatial version of the STP were compared with the reference values for both micro and macro scales. From the point of view of the macro scale, the global outputs obtained by the spatial version of the STP model were compared with the DTP model outputs. So, the AP, the global  $[Ca]_{i\ free}$ , the global  $I_{CaL}$ , and the global  $I_{rel}$  were presented side by side with the same variables of the DTP model. Regarding the micro scale, the outputs of the local variables generated by the spatial version of the STP model were analyzed in their capacity to reproduce the stochastic phenomena of the spontaneous calcium Sparks.

To analyze the outputs of the different conformations that the NxN version of the STP model can assume, it was defined to use five distinguishable conformations: 1x1, 2x2, 4x4, 8x8, and 16x16. The total number of LCCs inside the grid was constant for all these conformations at 1024. In this way, the simulations using the 1x1 grid were set the  $N_{LCC} = 1024$ , the simulations of the 2x2 grid were set the  $N_{LCC} = 256$ , the simulations of the 4x4 grid were set the  $N_{LCC} = 64$ , the simulations of the 8x8 grid were set the  $N_{LCC} = 16$ , and the simulations of the 16x16 grid were set the  $N_{LCC} = 4$ . Five realizations were executed for each conformation considering the protocol described in Section 3.2.2.

### Protocol of Simulation

Some cardiac pathologies, for instance, arrhythmia, are directly associated with the non-expected starting of the CICR process. Considering that a cardiac myocyte has a natural stimulation pacing of 1Hz, it is expected that the intracellular calcium dynamics

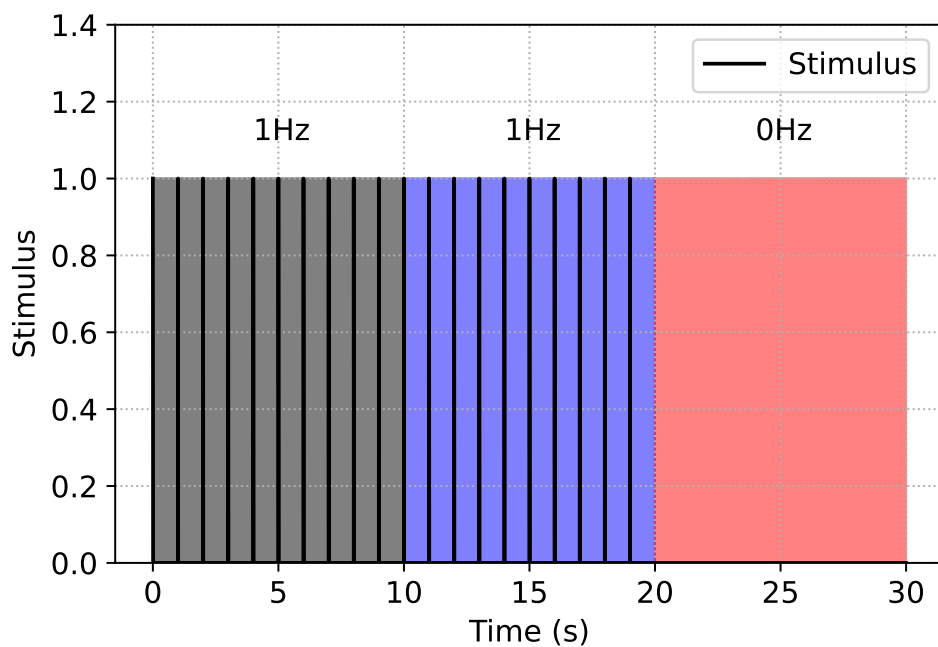
might follow this same pacing. Thus, the pathological effects caused by the Spontaneous calcium Sparks within the cell occur mainly during a resting phase.

To test how the proposed STP model can reproduce these Spontaneous Sparks of calcium in the intracellular medium, it was adopted a stimulation protocol composed of three phases performed in a row:  $P_1$ ,  $P_2$ , and  $P_3$ . The first phase, the  $P_1$ , was performed for 10 seconds under a stimulation frequency of 1Hz. The purpose of phase  $P_1$  was to model reach equilibrium; therefore, the results obtained in this phase were disregarded. The second phase, the  $P_2$ , has the same configurations as the phase  $P_1$ . It was performed for 10 seconds with a stimulation pacing of 1Hz. However, in phase  $P_2$ , the output results were registered and considered for this study. The third phase, the  $P_3$ , was also performed for 10 seconds, but the stimuli were interrupted over the stage. In other words, it was performed for 10 seconds without pacing.

When considering the phases  $P_2$  and  $P_3$  in this study analysis, it can be checked how the proposed model reproduces the sparks in these different pacing conditions, at 1Hz and 0Hz.

Figure 34 shows an illustration of the whole protocol of the stimulation presenting the entire 30 seconds of simulation highlighting the three phases  $P_1$ ,  $P_2$ , and,  $P_3$ .

Figure 34 – Stimulation protocol used in the 16x16 CRUs grid simulations. The protocol is composed by three phases  $P_1$  (black area),  $P_2$  (blue area) and  $P_3$  (red area).



Source: Created by the author. (2023).

### 3.2.3 Computational Implementation

The STP model proposed by this thesis is composed of 22 Ordinary Differential Equations (ODEs) derived from the original model, plus 6 ODEs added from the adaptation of the MC-based  $I_{CaL}$  model from the MJ model. All these ODEs have as domain the variable time.

However, once the diffusion of the free portion of the calcium ion is implemented in the  $[Ca]_i$  and  $[Ca]_{SR}$  dynamics, two spatial representations were inserted: the x-axis and y-axis. These two axes can be interpreted as the two-dimensional conformation of the NxN grid.

The numerical solution of all the 28 ODEs in the STP model was implemented using the Explicit Euler Method. The choice of this method was based on a test where it was used to simulate the novel proposed model under conditions in which the outputs must be the same as the original ten Tusscher and Panfilov (62) model. The outputs generated by the method were practically the same as expected by the original model. So, considering the quality obtained in this test and that it is one of the simplest methods to solve ODEs, the Explicit Euler Method was chosen to solve the ODEs in the computational experiments performed in this thesis. In resume, when applied in the hypothetical ODE

$$\frac{dF}{dt} = f(t), \quad (3.50)$$

the Explicit Euler Method generates an approximation of the solution by discretizing the domain of the variable  $t$  in  $\Delta t$  steps and evolving the variable  $F$  as

$$F(t + \Delta t) = F(t) + \Delta t \times f(t). \quad (3.51)$$

Concerning the equations of the variables  $[Ca]_i$  and  $[Ca]_{SR}$ , Equations 3.43 and 3.44, the time evolution of these equations was also solved using the Explicit Euler Method. For that, the calculus of the diffusion terms  $\Delta \bullet$  was done based on the Finite Difference Method. So, considering a two-dimensional CRU grid, the equation for the respective terms  $\Delta \bullet$  is

$$\begin{aligned} D_\bullet \Delta [Ca]_{\bullet free}^u &= D_\bullet \left( \frac{\partial^2 [Ca]_{\bullet free}^u}{\partial x^2} + \frac{\partial^2 [Ca]_{\bullet free}^u}{\partial y^2} \right) \\ &= D_\bullet \left( \frac{\partial^2 [Ca]_{\bullet free}^{x,y}}{\partial x^2} + \frac{\partial^2 [Ca]_{\bullet free}^{x,y}}{\partial y^2} \right) \\ &= D_\bullet \left( \frac{[Ca]_{\bullet free}^{x-1,y} - 2[Ca]_{\bullet free}^{x,y} + [Ca]_{\bullet free}^{x+1,y}}{\Delta x^2} + \right. \\ &\quad \left. + \frac{[Ca]_{\bullet free}^{x,y-1} - 2[Ca]_{\bullet free}^{x,y} + [Ca]_{\bullet free}^{x,y+1}}{\Delta y^2} \right) \end{aligned} \quad (3.52)$$

where the labels  $x$  and  $y$  represent the position of the CRU  $u$  inside the two-dimensional grid, and  $\Delta x$  and  $\Delta y$  represent the spatial distance between the CRUs.

It is important to clarify that the 1x1 simulations do not consider the effects of ionic diffusion since there is a single CRU. So, in the simulations under this condition, the fluxes  $\Delta \bullet$  were removed.

All the code developed was created in C++ language. The solution of the ODEs was executed using the Explicit Euler Method with a time step  $\Delta t = 10^{-3}ms$ . In the NxN simulations, the spatial discretization used to calculate the diffusion fluxes were homogeneously set over the whole CRUs grid in accordantly to the literature (28) as  $\Delta x = \Delta y = 0.5\mu m$ . To improve the efficiency of the computational execution, the NxN simulations were performed using the Message Passing Interface (MPI) technique to parallelize the solving of the equations within each CRU that composes the NxN grid. In this way, the computing of the local variables of each CRU is divided by the set of cores available for execution.

All simulations presented in this thesis were performed in a computer composed of one processor Intel(R) Core(TM) i9-9940X CPU @ 3.30GHz with 14 cores and a RAM capacity of 130GiB.

## 4 RESULTS

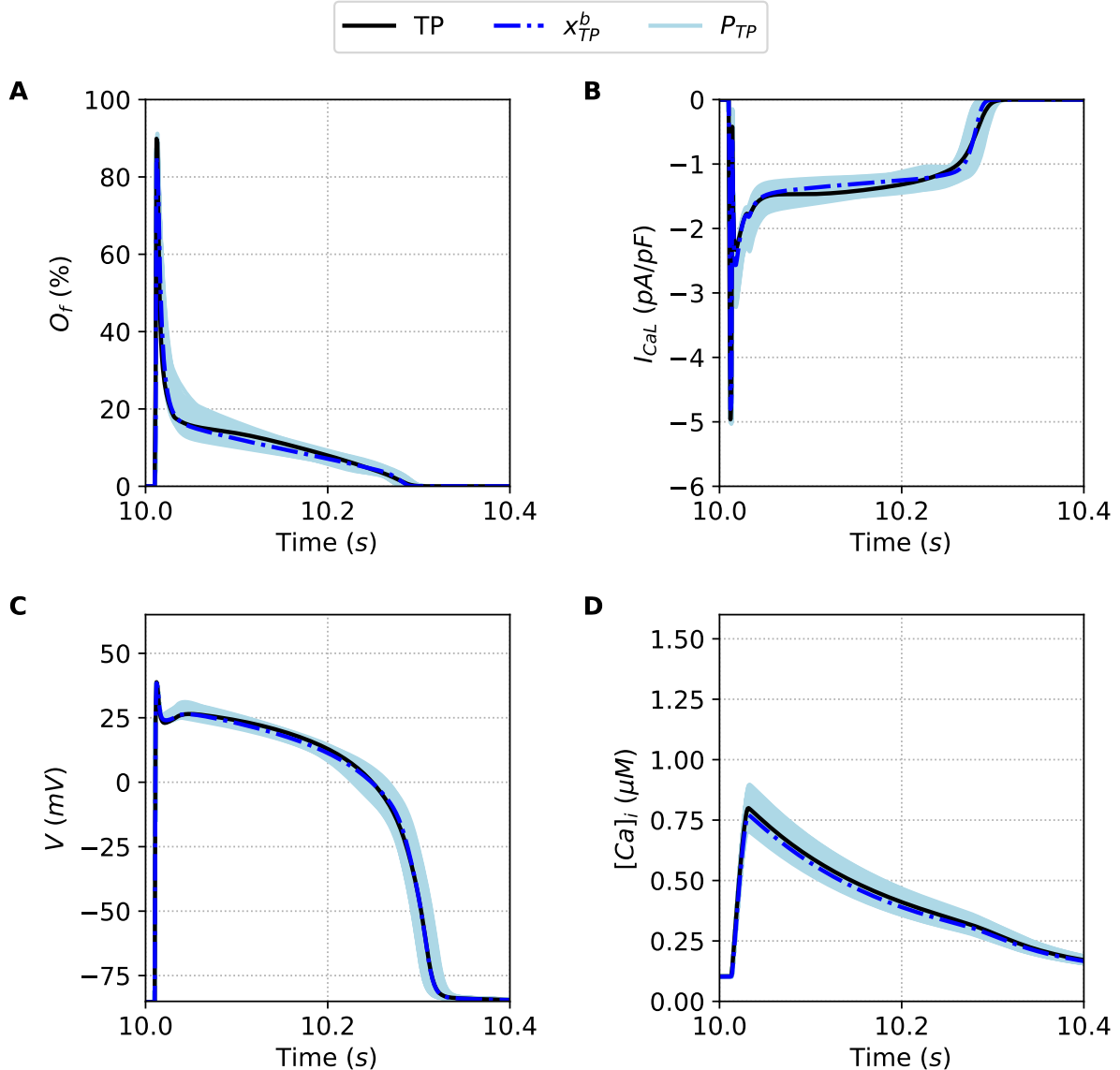
In this chapter, the results are according to each specific objective of this thesis. Section 4.1 presents the results of the fitting procedure used to insert the MC-based  $I_{CaL}$  model into the original TP model. This procedure generated the DTP model. From the DTP, the STP was generated by replacing strategic terms of the  $I_{CaL}$  and  $I_{rel}$  equations with random variables. The computational experiments performed using the 1x1 CRU STP model are presented in Section 4.2.1. At least, as explained in Section 3.1.5, the Spatial STP model was also used to analyze its capacity to reproduce the multiscale feature in the CICR process. The results obtained by the Spatial STP model are presented in Section 4.2.2.

### 4.1 DTP Model Fitting

The main objective of this thesis is to generate a computational model capable of reproducing the CICR dynamics of ventricular cardiac myocytes on micro and macro scales. This multiscale feature, from the subcellular to cellular level, is an object of analysis and study in ongoing studies associated with cardiac arrhythmias (18). In order to generate this multiscale computational model, the first step was the definition of the model formulations. As described in Section 3.1, this formulation was developed by replacing the original TP  $I_{CaL}$  dynamics with a new version based on the MJ formulation. As expected, this simple merging could not reproduce the human ventricular myocyte electrophysiology represented by the original TP. A Differential Evolution algorithm was used to elucidate this mismatch to fit this new model to the original TP outputs.

Using the strategies described in Section 3.1.2, the DE algorithm was executed only once to fit the DTP to the original TP model. Among the population  $P_{TP}$  of feasible solutions encountered by DE, the best solution  $x_{TP}^b$  was selected considering the fitness error values. Figure 35 shows the original traces for the Opening fraction of the LCC, the  $I_{CaL}$  current, the AP, and the Calcium transient  $[Ca]_i$  for the TP model. In each panel, the original output (black line) is plotted together with the results of the population selection of the algorithm alongside the best global fit of this population (blue lines).

Figure 35 – Outputs generated by the population of solutions  $P_{TP}$ . Traces obtained using the best solution of the population  $P_{TP}$ ,  $x_{TP}^b$  (dashed blue line), alongside the traces obtained using the other solutions that compose the population (light blue lines) compared with the original ten Tusscher and Panfilov (62) model (black line). A: Opening fraction,  $O_f$ . B:  $I_{CaL}$  current. C: Action Potential. D: Intracellular Calcium concentration,  $[Ca]_i$ .



Source: obtained from Novaes et al. (40).

The selection of the population made by the DE execution was very good. The key is not that there is a particular solution that fits almost perfectly the outcome but that the population spans remarkably the general surroundings of the model space. We can see in Table 2 a comparison of the key properties of the AP and  $[Ca]_i$  for the original model with the average and standard deviation values obtained from the selected populations  $P_{TP}$  and the best solution  $x_{TP}^b$ .

Table 2 – Features for the AP and  $[Ca]_i$  traces of the best solutions obtained by DE execution.

Features	$P_{TP}$	$x_{TP}^b$	TP
$APD_{50}^a$	$275.2 \pm 4.9$	274	273
$APD_{90}^a$	$301.8 \pm 4.8$	301	301
$[Ca]_{iMin}^b$	$0.1 \pm 0.001$	0.1	0.1
$[Ca]_{iPeak}^b$	$0.8 \pm 0.04$	0.77	0.81

Values of the features for the Action Potential (AP) and Intracellular Calcium concentration ( $[Ca]_i$ ) for the population of solutions  $P_{TP}$  and its best solution  $x_{TP}^b$  obtained by the DE algorithm for the DTP model in comparison with respective original ten Tusscher and Panfilov (62) model.

<sup>a</sup>Values are expressed in  $ms$ .

<sup>b</sup>Values are expressed in  $\mu M$ .

Source: Created by the author. (2023)

These populations of solutions  $P_{TP}$  fitted with typical errors in the AP and  $[Ca]_i$  features around 0–1%. Another important fact is that the values for the best parameter fit was  $F(x_{TP}^b) = 9\%$ . In this way, the best solution  $x_{TP}^b$  encountered is such that

$$x_{TP}^b = \{ \overbrace{1.293}^{x_0}, \overbrace{0.688}^{x_1}, \overbrace{1.162}^{x_2}, \overbrace{1.620}^{x_3}, \overbrace{1.369}^{x_4}, \overbrace{0.415}^{x_5}, \overbrace{1.027}^{x_6}, \overbrace{0.397}^{x_7}, \overbrace{0.793}^{x_8}, \overbrace{1.279}^{x_9}, \overbrace{0.739}^{x_{10}} \}.$$

This solution was selected to generate the Simulation Experiments described in Section 3.2. The results of these Simulation Experiments are presented in Section 4.2.

## 4.2 Simulation Results

Section 4.1 presents the results of the method used to generate the base model for this thesis, a deterministic version of the TP model with an MC-based formulation in the  $I_{CaL}$  mathematics. This novel model was adjusted for two stochastic versions: the 1x1 and the NxN STP model. Sections 4.2.1 and 4.2.2 present the computational experiment results using the respective versions.

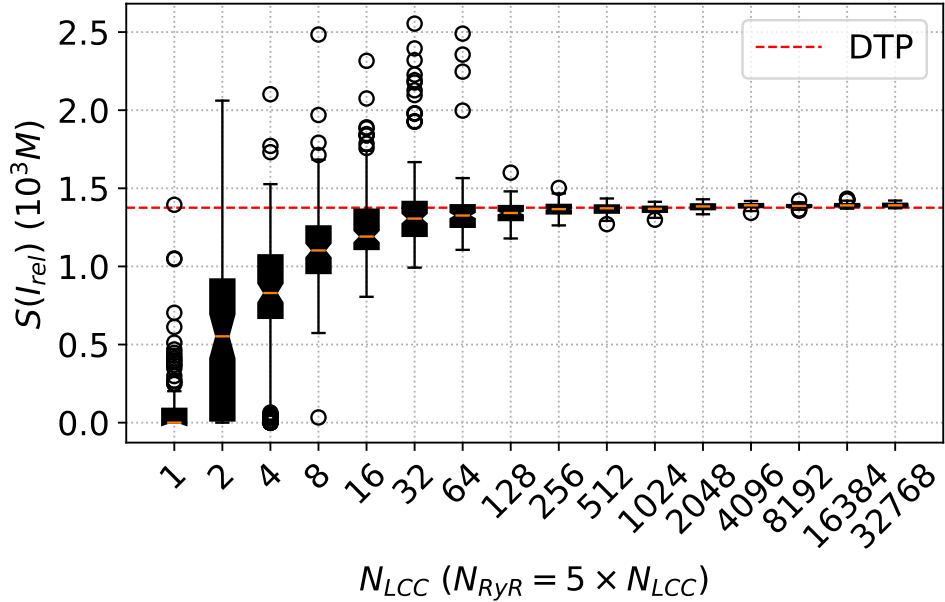
### 4.2.1 1x1 CRU Simulation Results

The first set of experiments assumed the STP model composed of a 1x1 grid of CRU or, in other words, one single CRU. In this case, the multiscale factor is applied by varying the total number of LCCs and RyRs inside this single CRU. For that, as described in Section 3.2.1, the total number of LCCs ran as  $N_{LCC} = \{2^i | i \in \mathbb{I} \text{ and } i = 0 - 15\}$ ; and, for each respective value of  $N_{LCC}$ , the total number of RyRs was defined as  $N_{RyR} = 5 \times N_{LCC}$ .

Using the STP model composed of 1x1 CRU, it was simulated 110 pulses for each value assumed by the  $N_{LCC}$  and  $N_{RyR}$ . Disregarding the first ten pulses, Figure 36 shows

the descriptive measures of the  $S$  values (Equation 3.49) grouped by  $N_{LCC}$  and  $N_{RyR}$ . These measures are compared with the same  $S$  value obtained from the deterministic version of the DTP model.

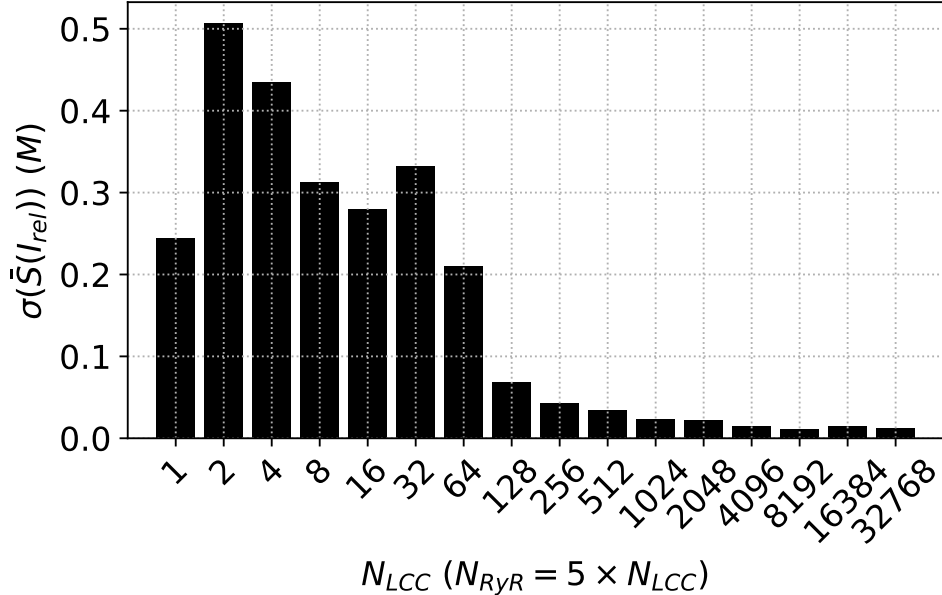
Figure 36 – Descriptive Measures of the stochastic metric  $S$ . The results present the outputs of STP model varying the  $N_{LCC}$  as  $N_{LCC} = \{2^i | i \in \mathbb{I} \text{ and } i = 0 - 15\}$  and using  $N_{RyR} = 5 \times N_{LCC}$ . For each  $N_{LCC}$  and, consequently,  $N_{RyR}$ , there were generated  $n = 100$  outputs. In contrast, there are presented also the  $S$  values for the DTP model.



Source: Created by the author. (2023).

As shown in Figure 36, in qualitative analysis, the STP model could reproduce the multiscale feature since the outputs expressed the stochastic behavior in the sets of simulations using small values for  $N_{LCC}$  and  $N_{RyR}$  ( $N_{LCC} \leq 64$ ). This stochastic behavior is directly associated with what is expected in simulations under the micro scale condition. The simulations using higher values for  $N_{LCC}$  and  $N_{RyR}$  ( $N_{LCC} \geq 128$ ) presented a notable decrease in the stochasticity of the outputs. This phenomenon agrees with what is expected by the multiscale feature since, once the  $N_{LCC}$  and  $N_{RyR}$  increase in the model formulation, it is expected that a macro scale behavior appear in the simulations outputs. Thus, it is expected that the model start to reproduce the Deterministic scenario causing a decrease in the randomness of the outputs of the simulations. Figure 37 shows the Standard Deviation  $\sigma(\bar{S})$  where  $\bar{S}$  is the set of 100  $S$  values obtained from the simulation experiments for each respective  $N_{LCC}$  and  $N_{RyR}$ .

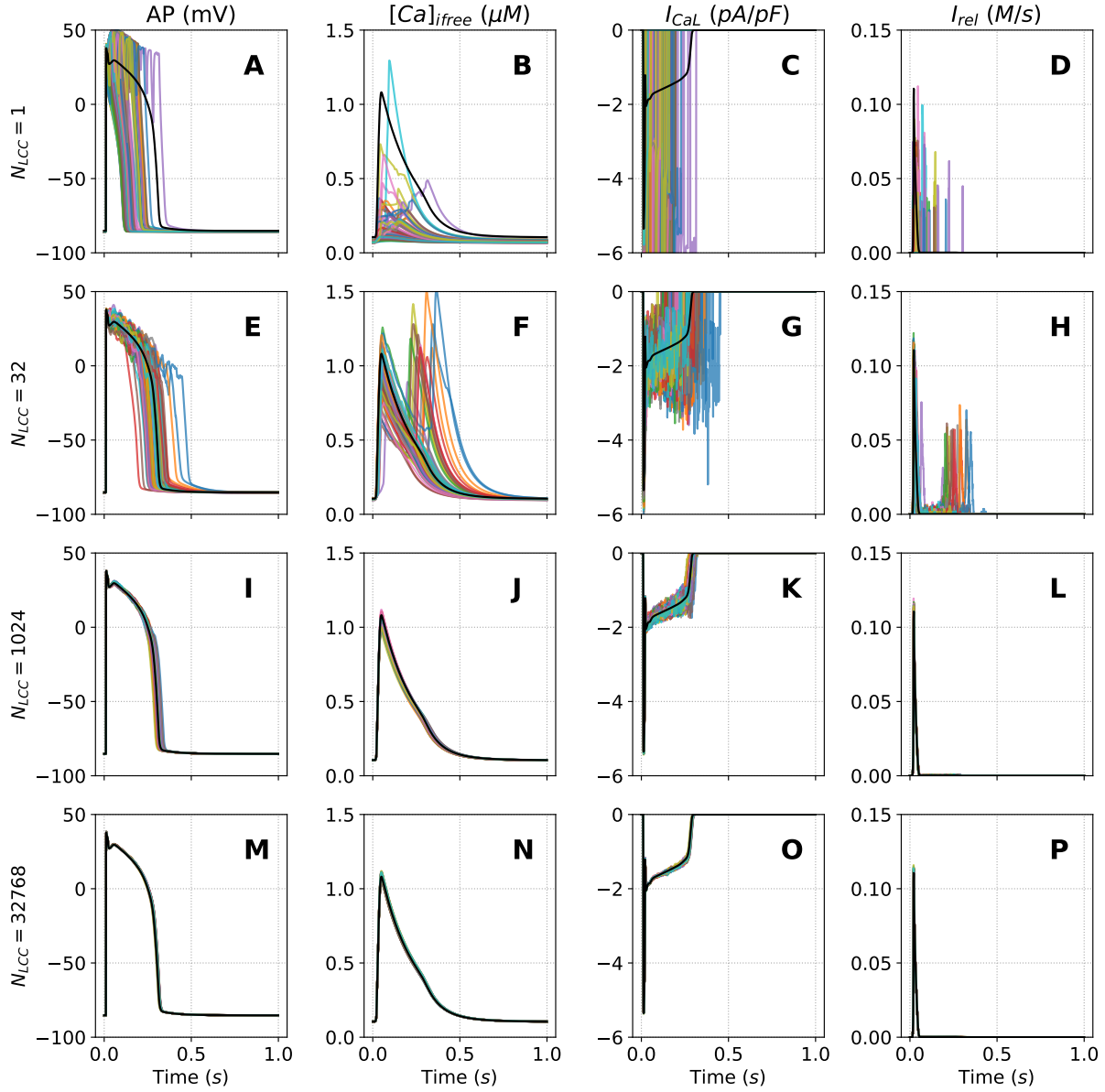
Figure 37 – Standard Deviation  $\sigma(\bar{S})$  obtained from the set of  $n = 100$   $S$  values calculated for each respective value assumed by  $N_{LCC}$  as  $N_{LCC} = \{2^i | i \in \mathbb{I} \text{ and } i = 0 - 15\}$  and using  $N_{RyR} = 5 \times N_{LCC}$ . For each  $N_{LCC}$  and, consequently,  $N_{RyR}$ , they were generated  $n = 100$  outputs.



Source: Created by the author. (2023).

Besides the  $S$  and the  $\sigma(S)$  values, the same behavior can be seen in the traces of the outputs. Figure 38 presents the 100 output curves of the main variables of the STP outputs (color lines) in comparison with the same traces obtained by the DTP model (black line). Panels A-D show the AP,  $[Ca]_{i free}$ ,  $I_{CaL}$ , and  $I_{rel}$  traces obtained from STP using  $N_{LCC} = 1$ ; panels E-H show the same traces obtained from STP using  $N_{LCC} = 32$ ; panels I-L show the same traces obtained from STP using  $N_{LCC} = 1024$ ; and panels M-P show the same traces obtained from STP using  $N_{LCC} = 32768$ . For all simulations the  $N_{RyR}$  was defined as  $N_{RyR} = 5 \times N_{LCC}$ .

Figure 38 – Output curves of the AP,  $[Ca]_{i,free}$ ,  $I_{CaL}$  and  $I_{rel}$ . The results present the outputs of the STP model varying the  $N_{LCC}$  as  $N_{LCC} = \{1, 32, 1024, 32768\}$  and using  $N_{RyR} = 5 \times N_{LCC}$ . For each  $N_{LCC}$  and, consequently,  $N_{RyR}$ , there are presented  $n = 100$  samples. In contrast, there are presented also the output values for the DTP model (black line).



Source: Created by the author. (2023).

Following the same behavior shown in Figure 36, the curves presented in Figure 38 also converged to the deterministic values as soon as the  $N_{LCC}$  and  $N_{RyR}$  grew. It indicates that the STP model could adequately reproduce both extreme scales, micro and macro scales since it was capable of expressing the stochastic nature under a micro scale condition (low values for  $N_{LCC}$ ) and reproducing the deterministic outputs as expected in simulations under a macro scale condition (high values for  $N_{LCC}$ ).

#### 4.2.2 NxN CRUs Simulations Results

The results presented in Section 4.2.1 express insight into the capacity of the STP model to reproduce the micro and the macro scales when it analyses the effects of the number of LCCs and RyRs in the cellular stochastic nature. However, these simulations have several limitations since it does not consider essential features that play a crucial role in the CICR dynamics as, for instance, intracellular calcium diffusion. This Section presents the results of simulating the STP model using the NxN CRUs grid assuming  $N = \{1, 2, 4, 8, 16\}$ . Using this two-dimensional disposition of CRU, it is possible to consider the effects of calcium diffusion over the intracellular domain.

Assuming a Basic Cycle Length (BCL) of one second, each realization of the STP model using the protocol presented in Section 3.2.2 generated ten samples of this BCL under 1Hz pacing and ten samples of the same BCL without pacing. The mentioned protocol was executed five times for each set of experiments, each assuming the respective N value. So, for each value assigned for N, five realizations times ten samples generated 50 samples of one-second BCL for both 1Hz and 0Hz pacing rates.

Section 4.2.2.1 presents the first set of results, which shows the relation between Micro and Macro scales within the spatial version of the STP model. For this, the diffusion factor for all experiments were set as being the realistic value,  $D_R$ . Besides this, the total number of LCCs and RyRs in the NxN CRUs grid was set as  $N_{LCC} = 1024$  and  $N_{RyR} = 5N_{LCC} = 5120$ . This global value was defined based on the 1x1 CRU STP results that, using the  $N_{LCC} = 1024$ , already presented the deterministic behavior (see Figure 36). So, in the same way, the NxN STP version must also reproduce the deterministic outputs of the DTP model. Besides the definition of the global value of the LCCs and RyRs, it was defined different conformations for the NxN grid size. It was defined as five distinct conformations: 1x1, 2x2, 4x4, 8x8, and 16x16. In this manner, to keep the global value of the  $N_{LCC}$  and  $N_{RyR}$ , the local values for the  $N_{LCC}^u$  ranged respectively as 1024, 256, 64, 16, and 4 (for all cases the ratio  $N_{RyR}^u = 5N_{LCC}^u$  was maintained). The results presented in Section 4.2.2.1 compare the global outputs of the spatial STP model with the DTP reference values. For that, it was used the outputs obtained with the realizations at 1Hz pacing. In summary, 4.2.2.1 demonstrates how the global values of the spatial version of the STP model correlate with the DTP.

Then, in Section 4.2.2.2, it was analyzed the specific phenomenon of sparks. For this analysis, it was selected the 16x16 STP model. This choice was made because this conformation has small values for the  $N_{LCC}$  and  $N_{RyR}$  and, consequently, has more probability of reproducing the calcium Sparks. Besides this, the local values for the LCCs and RyRs in this conformation are in the physiological ranges expressed in the literature(50). Section 4.2.2.2 presents the results obtained under the 1Hz pacing and the outputs obtained under the 0Hz. This condition of no stimulus is suitable for analyzing

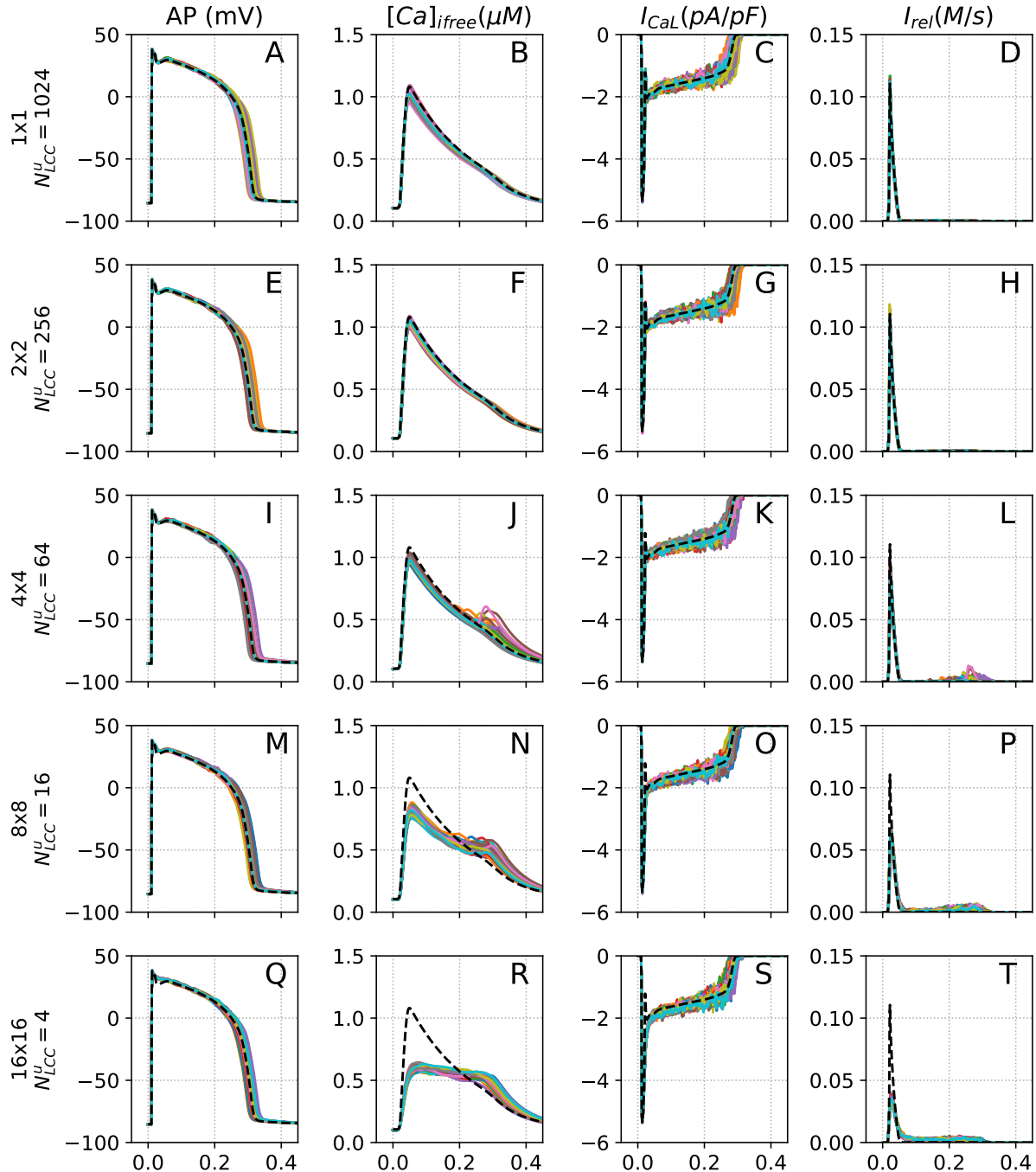
these stochastic phenomena. The effects of the diffusion factor are also presented in Section 4.2.2.2 analyses.

#### 4.2.2.1 Micro vs Macro Scale Analysis

The multiscale feature considered in this thesis is the capacity of the model to reproduce both the local stochastic nature of the ionic channels (micro scale) and the global deterministic outputs at a cellular level (macro scale). The NxN STP model was simulated in different conformations to analyze its capacity to reproduce the multiscale feature.

Figure 39 presents the traces of the global variables AP,  $[Ca]_{i,free}$ ,  $I_{CaL}$ , and  $I_{rel}$  obtained by the spatial STP model under the different conformations in contrast with the same variables from the DTP model.

Figure 39 – Output curves of the AP,  $[Ca]_{i,free}$ ,  $I_{CaL}$  and  $I_{rel}$ . The results present the outputs of the NxN CRUs STP model varying the N as  $N = \{1, 2, 4, 8, 16\}$ . For all cases, the global value for the  $N_{LCC}$  and  $N_{RyR}$  were  $N_{LCC} = 1024$  and  $N_{RyR} = 5N_{LCC} = 5120$ . For each N there are presented  $n = 50$  samples. In contrast, there are presented also the output traces from the DTP model (black line).



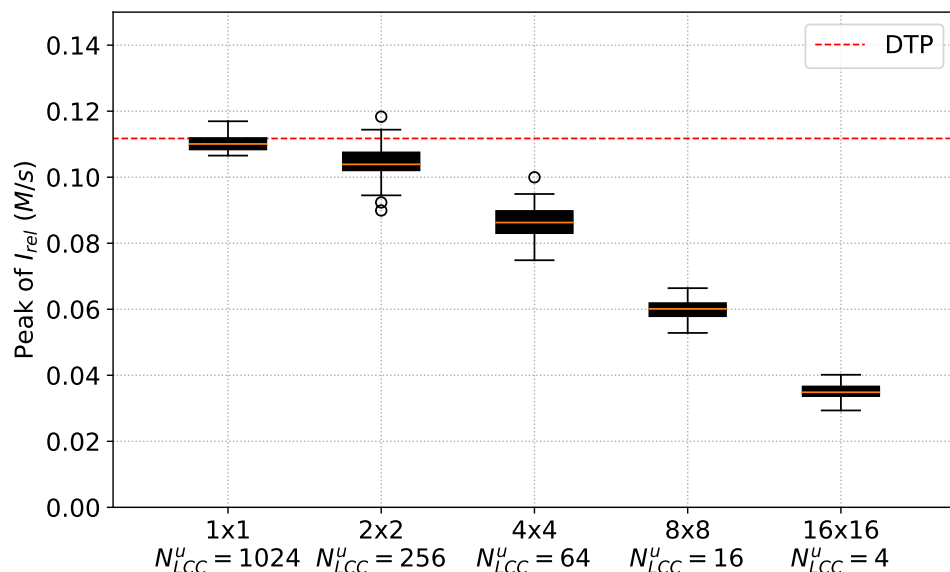
Source: Created by the author. (2023).

Figure 39 shows that the spatial STP model suitably reproduced the global values of AP and  $I_{CaL}$  variables in the five conformations. However, the  $[Ca]_{i,free}$  and the

$I_{rel}$  outputs diverged from the expected DTP reference when the  $N_{LCC}$  and  $N_{RyR}$  local parameters assumed small values (in a subjective view, as soon as the local parameters assumed a micro scale condition).

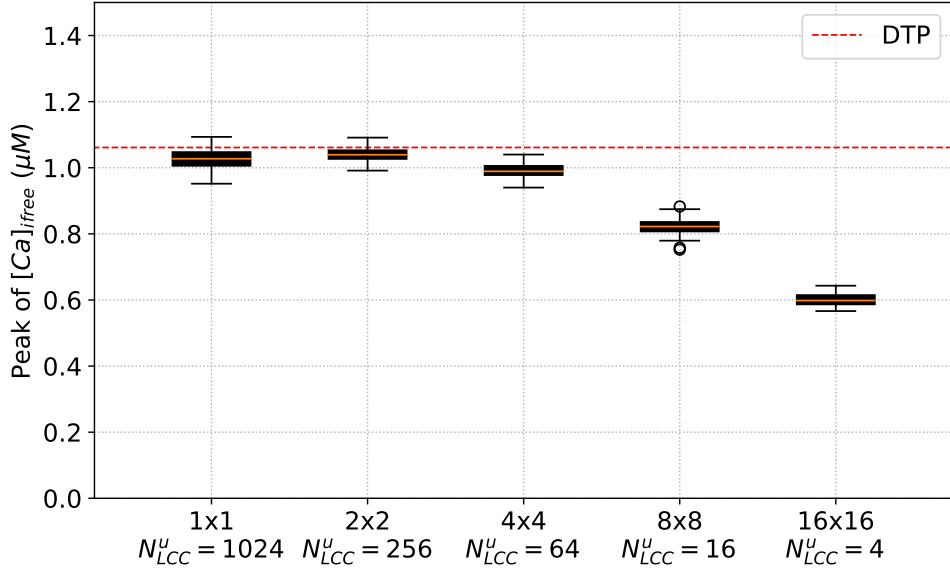
As shown in Figure 39, the peak values reached by both  $[Ca]_{ifree}$  and  $I_{rel}$  are smaller than expected by the DTP model. Although this divergence was not expected, the fact that both  $[Ca]_{ifree}$  and  $I_{rel}$  had this behavior simultaneously is explained by the fact that the  $I_{rel}$  is the main responsible for filling the  $[Ca]_i$  medium with calcium. An insufficiency in the  $I_{rel}$  current should lead to a smaller peak of the  $[Ca]_i$  levels. To clarify this relation, Figure 40 and Figure 41 present the  $I_{rel}$  and the  $[Ca]_{ifree}$  peak values of the outputs obtained by the spatial STP model compared to the DTP reference for of the five conformations.

Figure 40 – Descriptive Measures of the peak values of the  $I_{rel}$  current obtained by the simulation of the spatial STP model in the five conformations: 1x1, 2x2, 4x4, 8x8, 16x16. For each conformation, there were generated  $n = 50$  samples.



Source: Created by the author. (2023).

Figure 41 – Descriptive Measures of the peak values of the  $[Ca]_{i,free}$  concentration obtained by the simulation of the spatial STP model in the five conformations: 1x1, 2x2, 4x4, 8x8, 16x16. For each conformation, there were generated  $n = 50$  samples.



Source: Created by the author. (2023).

As can be seen, the spatial STP model could reproduce the macro scale outputs only when assuming higher values for the local variables  $N_{LCC}^u$  and  $N_{RyR}^u$  ( $N_{LCC}^u \geq 64$ ). When taking smaller values of the same variables ( $N_{LCC}^u \leq 16$ ), the model could not reproduce the global or the macro scale outputs. So, although the spatial STP model could reproduce the micro scale outputs under a micro scale conditions (Section 4.2.1) and the macro scale outputs under macro scale conditions (Figure 39), the model could not link these two scales. In other words, the spatial STP model could not reproduce the macro scale using locally micro scale parameters. This finding presents a limitation of the proposed spatial STP model in reproducing the multiscale feature.

#### 4.2.2.2 Calcium Sparks

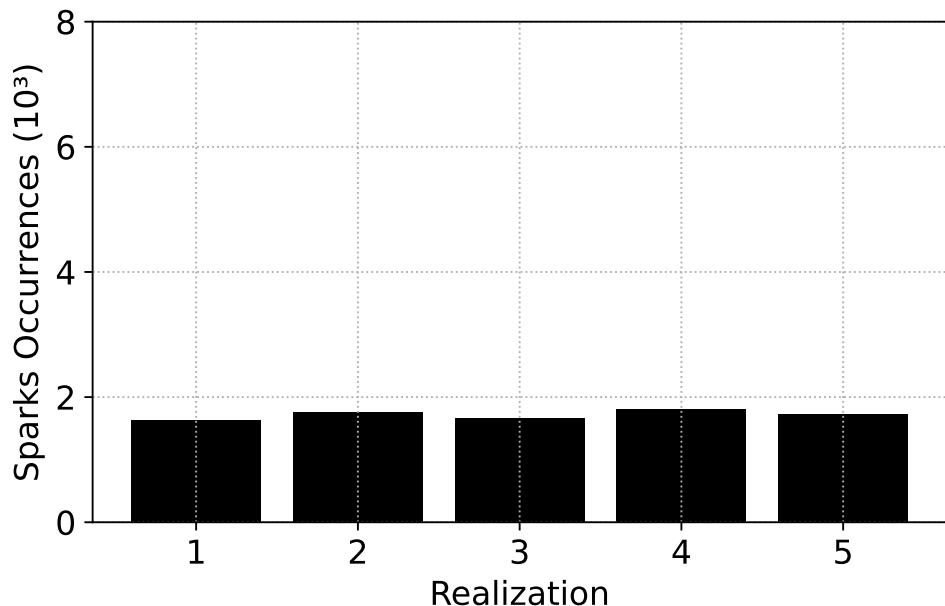
As mentioned in Section 2.2.4, Spontaneous calcium Sparks are closely linked to cardiac ailments like arrhythmias. Therefore, a computational model replicating this phenomenon might be valuable in further research in this area. Since the STP model has the presence of random variables in its formulation, it is expected that it could reproduce the local stochasticity presented in a CICR process, including the appearance of the Spontaneous Sparks. To check the reproduction of the calcium Sparks by the STP model, its outputs at 1Hz and 0Hz pacing rates were considered. Besides, the Spark phenomena are a local flux of calcium ions. So, the results presented in this Section were obtained by simulating the 16x16 spatial STP model considering the realistic scenario,  $D_R$ , for the

diffusion factors. The outputs presented in this Section were taken from all the local CRU  $u$  that compose the grid individually.

### Sparks at 1Hz pacing

At 1Hz pacing, the STP model presented a considerable number of calcium Sparks over the entire BCL. The total number of sparks obtained by each realization was practically the same, approximately 1700. Figure 42 shows the total number of Sparks encountered by each realization.

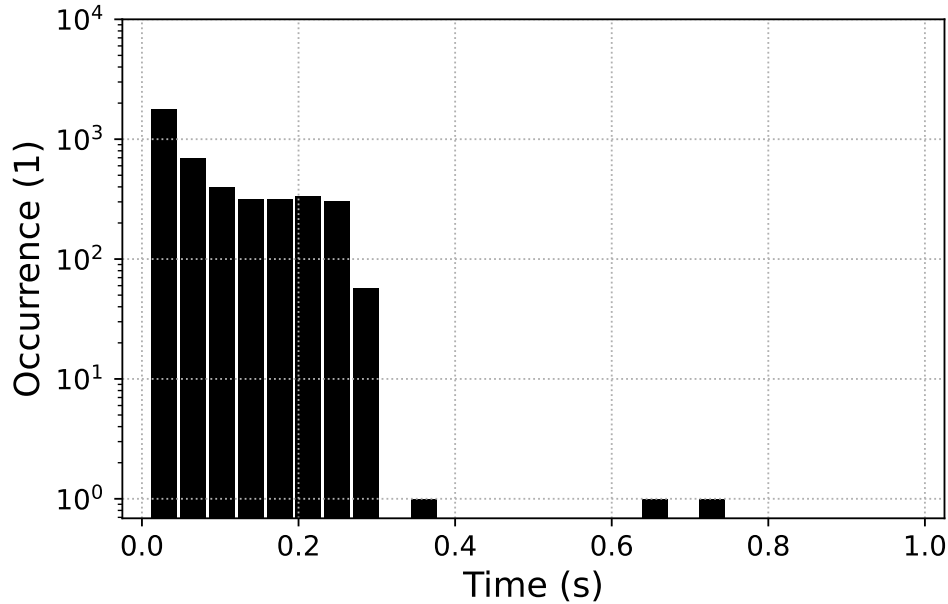
Figure 42 – Total number of Sparks obtained by each realization of the 16x16 STP model stimulated at 1Hz by ten seconds.



Source: Created by the author. (2023).

Considering that each realization has ten BC samples, it means that, on average, there were around 170 sparks by each BC over the whole 16x16 grid. It is important to highlight that this value includes Evoked Sparks and Spontaneous Sparks. Since the STP model was stimulated during this period, all the calcium Sparks obtained during the cell activation are Evoked. The calcium Sparks obtained after the cell restore the resting condition are Spontaneous. The STP model case is expected to achieve this resting condition around 350ms after the stimulation. In this way, from the 8476 Sparks encountered by all realizations, only three appeared after the 350ms. Figure 43 shows a histogram with the distribution of the occurrence of all calcium Sparks by each fraction of the BCL.

Figure 43 – Distribution of the occurrence of all calcium Sparks encountered by the five realizations of the 16x16 STP model simulated at a 1Hz pacing rate over the whole CRU grid.



Source: Created by the author. (2023).

As can be seen, practically all calcium Sparks occurred before the 350ms. It is following what is expected since, during this period, the CICR process is very active due to the stimulus. Figure 43 also presented a remarkable decrease in the number of calcium sparks that appeared after the cell restored the resting condition (after 350ms). In this period, the ideal scenario would be the absence of sparks. But, due to the stochasticity nature of the cell, the STP model reproduced three occurrences of this phenomenon during this resting phase.

Figure 44 presents the traces of the local  $[Ca]_{i\ free}^u$ ,  $I_{CaL}^u$ , and  $I_{rel}^u$  curves of one BC sample where both the Evoked and Spontaneous calcium Sparks can be seen.

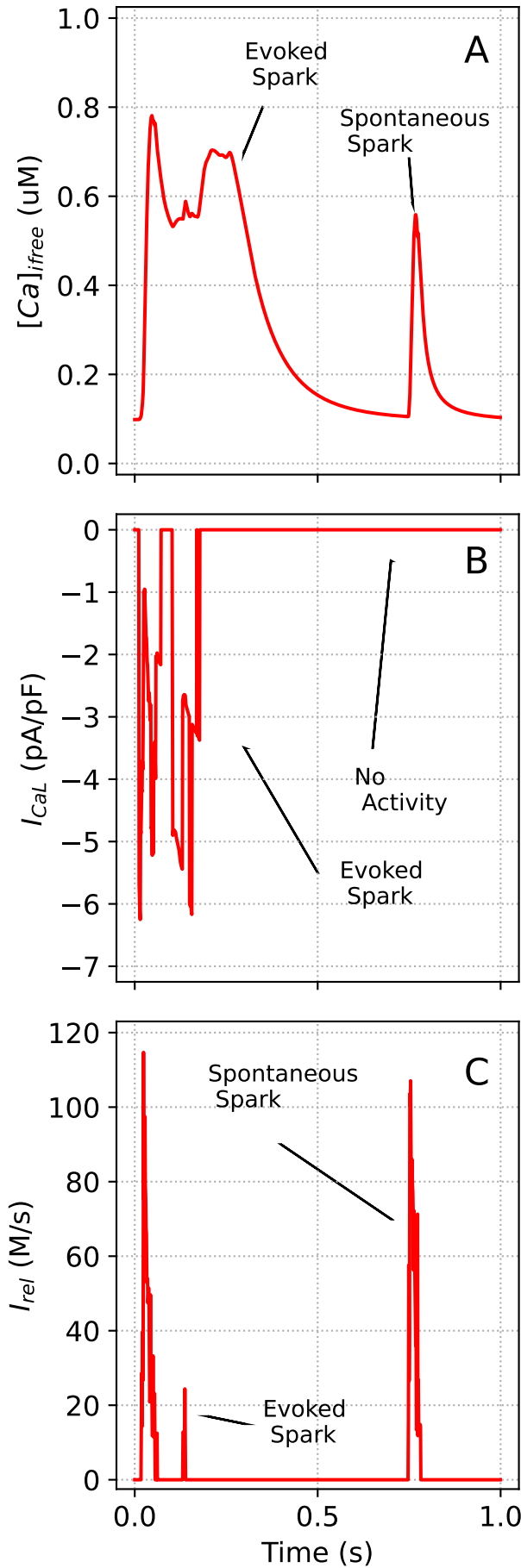


Figure 44 – Traces of the  $[Ca]_{free}^u$ ,  $I_{CaL}^u$ , and  $I_{rel}^u$  variables obtained by one CRU  $u$  that compose the 16x16 CRU grid of the STP model simulated under 1Hz stimulation. In this BC sample, it can be seen both the Evoked and the Spontaneous calcium Sparks. The first one is Evoked since it occurs during the active phase of the cell. In this phase, the LCCs may still be active and allow calcium influx inside the cell. As can be noticed in  $I_{CaL}^u$  current, panel B, this first Spark was preliminary triggered due to the LCC opening. The activation of the RyR was not so expressive (panel C). The second calcium Spark was different. As can be seen in panel B, the LCCs remained completely inactive. The occurrence of the Spark was exclusively due to the RyR randomness; hence, it was Spontaneous.

Source: Created by the author. (2023).

Figure 45 presents a sequence of distinct moments of the locals  $[Ca]_{i free}^u$  dynamics over the time obtained by stimulating the 16x16 STP model. As this sequence shows the CRU activities due to the stimulation, the calcium sparks observed in the images can be seen as Evoked calcium sparks.

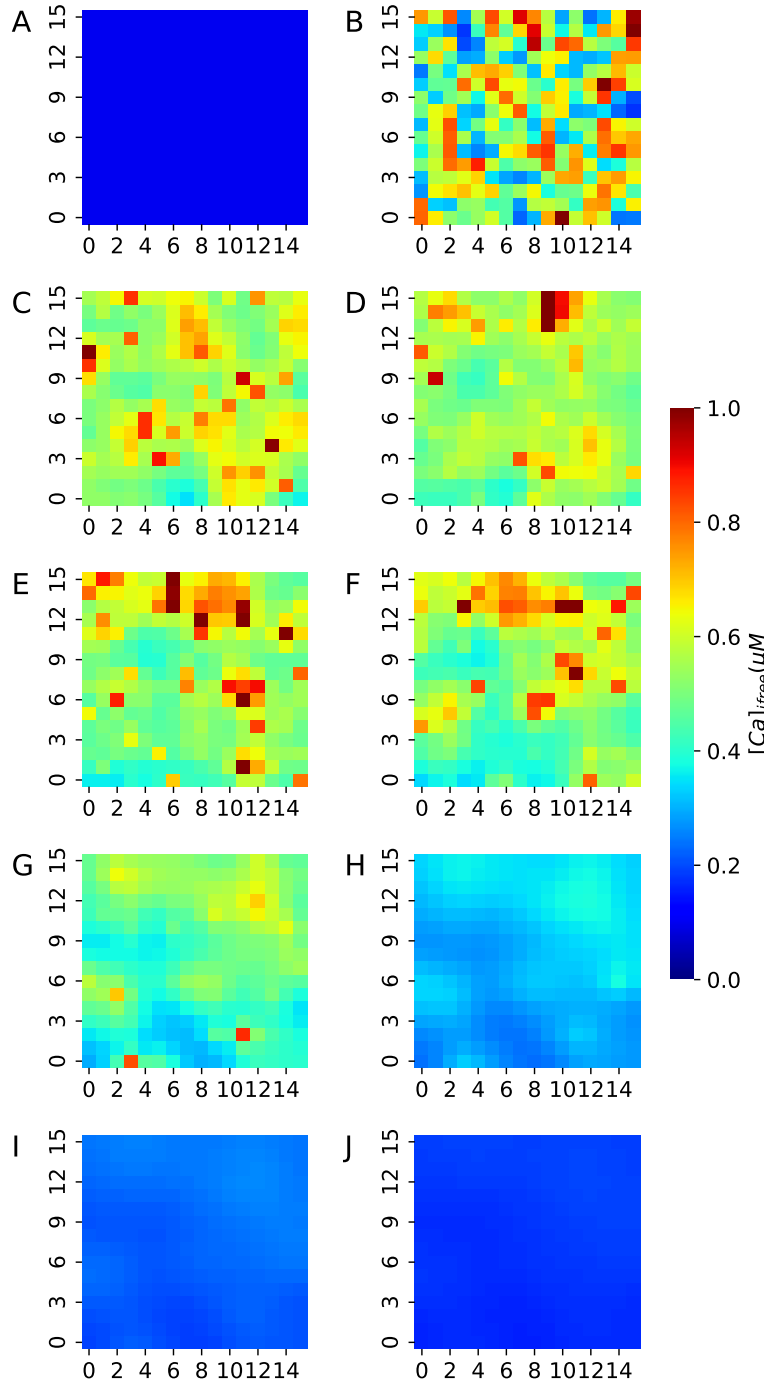


Figure 45 – Sequence of distinct moments of the dynamics of the local variables  $[Ca]_{i free}^u (\mu M)$  over 450ms after the stimulation. The Panels were chronologically organized where Panel A represents the moment  $t = 0ms$ , Panel B represents the moment  $t = 50ms$ , Panel C represents the moment  $t = 100ms$ , up to Panel J that represents the moment  $t = 450ms$ .

Source: Created by the author. (2023).

Besides the Evoked calcium Sparks generated due to the stimulation presented in Figure 45, the 16x16 STP model also reproduced the Spontaneously calcium Sparks. Figure 46 shows distinct moments of the locals  $[Ca]_{i free}^u$  dynamics over the time obtained

by the STP model at a resting phase. As the CRUs were expected to remain inactive, the calcium spark observed in the images can be seen as Spontaneous calcium sparks.

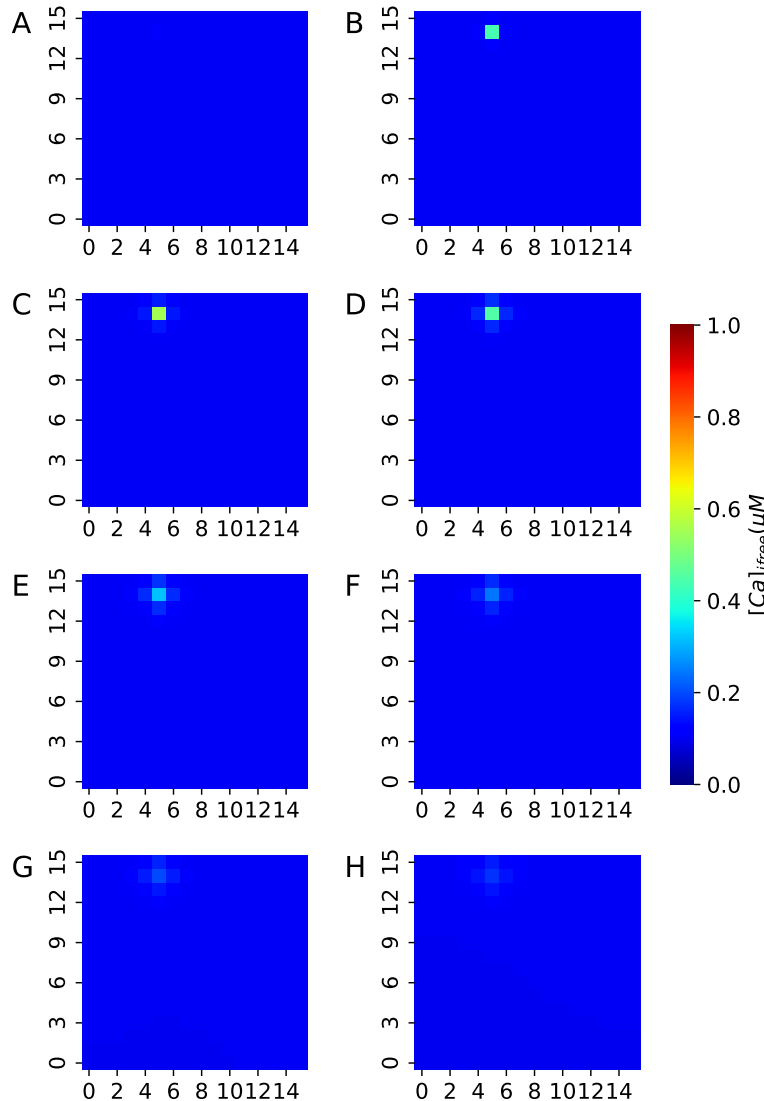
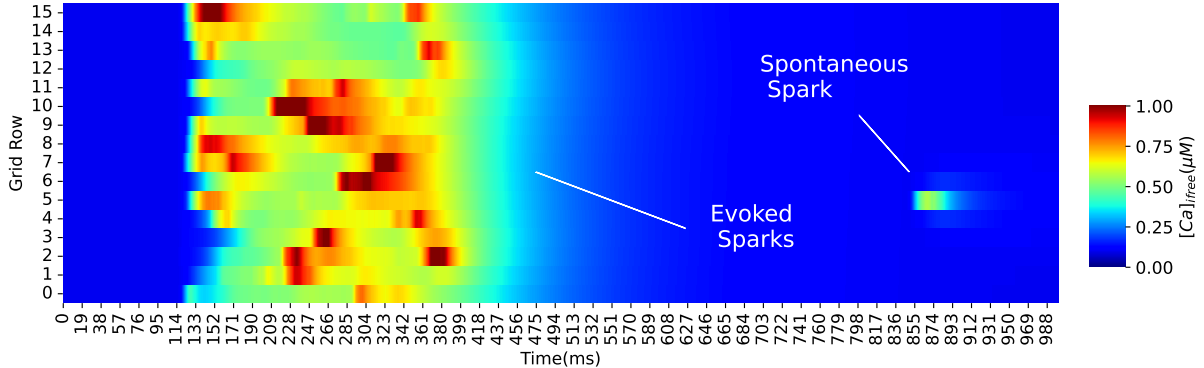


Figure 46 – Sequence of distinct moments of the dynamics of the local variables  $[Ca]_i^u \text{ free} (\mu M)$  over 350ms during a resting phase. The Panels were chronologically organized where Panel A represents the moment  $t = 0s$ , Panel B represents the moment  $t = 0.05s$ , Panel C represents the moment  $t = 0.10s$ , up to Panel H that represents the moment  $t = 0.35s$ .

Source: Created by the author. (2023).

Both Evoked and Spontaneous Sparks can be seen in the same image by using a linescan-type plot of the 16x16 CRU grid of the STP model. Figure 47 shows both Evoked and Spontaneous Sparks in the linescan-type image of the 14th row of the 16x16 CRU grid over one second of simulation.

Figure 47 – Linescan image of the 14th row of the 16x16 CRU grid that compose the STP model obtained by one second of simulation.



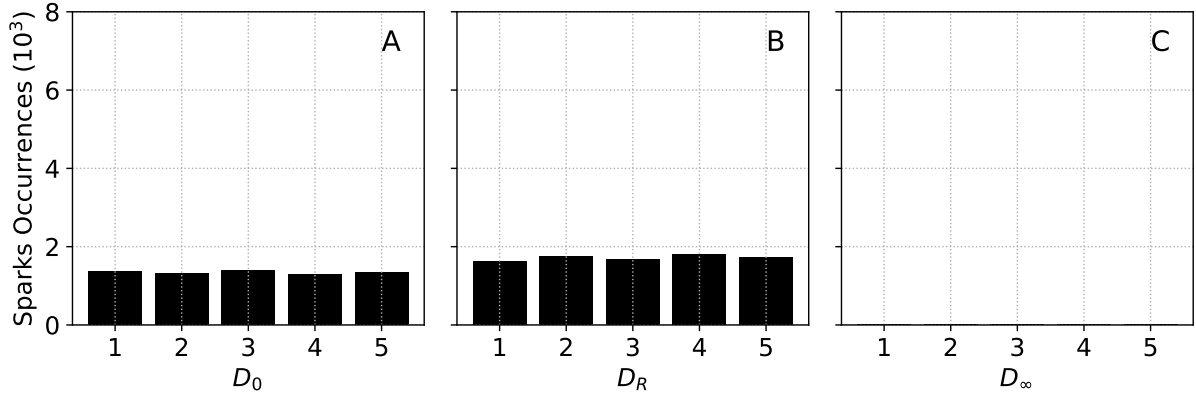
Source: Created by the author. (2023).

Concerning the effects of the Diffusion Factor on the number of Sparks, the STP model was also simulated in the other two diffusion conditions defined in Section 3.1.5. As can be seen in Figure 48, simulating the STP model under the  $D_0$  condition presented fewer calcium Sparks when compared with the realistic diffusion factor  $D_R$ . This behavior is expected since the calcium diffusion might provide a slight increase in the general level of calcium ions and, so, this higher level of intracellular calcium concentrations might contribute for the emergence of new Sparks. In the conditions using the diffusion factor  $D_0$ , only the local calcium concentration increases. The others remain at the expected basal level and, thus, are less susceptible to generating calcium Sparks.

On the other extreme, in the  $D_\infty$  condition, it can be noticed that Spontaneous calcium Sparks stop appearing (Figure 48, panel C). This absence of the calcium Sparks might be associated with the multiscale feature. It makes sense since this global and unique calcium concentration have the same formulation as the DTP model. In this way, this lack of calcium Sparks makes sense once the  $D_\infty$  is one step toward achieving the macro scale where the stochastic phenomena take place to the deterministic behavior.

Figure 48 presents the number of calcium Sparks and their relation with the calcium ion diffusion.

Figure 48 – Comparison of the total number of spontaneous calcium Sparks obtained in the STP model composed by the 16x16 CRU grid simulated by ten seconds at 1Hz pacing under the three diffusion conditions:  $D_0$  (A),  $D_R$  (B), and  $D_\infty$  (C).



Source: Created by the author. (2023).

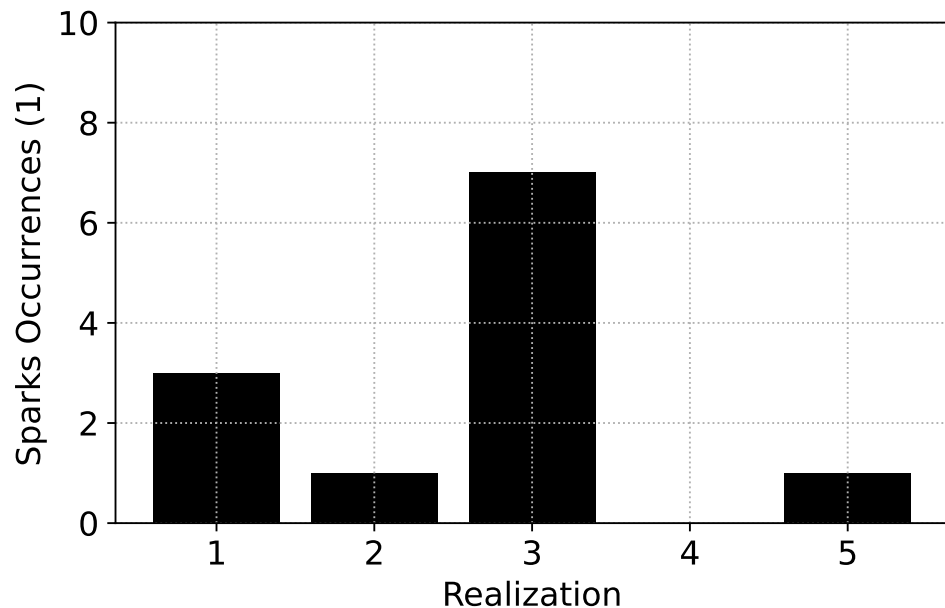
### Sparks Without Pacing

The same analyses can be replicated over the 16x16 STP results executed using a pacing rate of 0Hz. Since the model was never stimulated, all calcium Sparks are Spontaneous in this case.

As expected, the outputs of the simulations without pacing generated considerably fewer calcium Sparks when compared with the same number of simulations under the 1Hz pacing for the same amount of samples. Altogether, 12 calcium Sparks appeared over the five realizations composed of ten BCL samples. As discussed before, this is expected because the model simulated at 0Hz, is not stimulated, and, consequently, its activity is dependent exclusively on the probabilities of stochasticity. The comparison between the two protocol phases, 1Hz and 0Hz, is more appropriate when it is considered only the resting phase of the BC at 1Hz ( $t \geq 350ms$ ). In this case, it can be seen that three calcium Sparks encountered at the 1Hz condition have the same magnitude order as the 12 occurrences obtained at the 0Hz condition.

Figure 49 shows the total number of Sparks encountered by each realization without any stimulation.

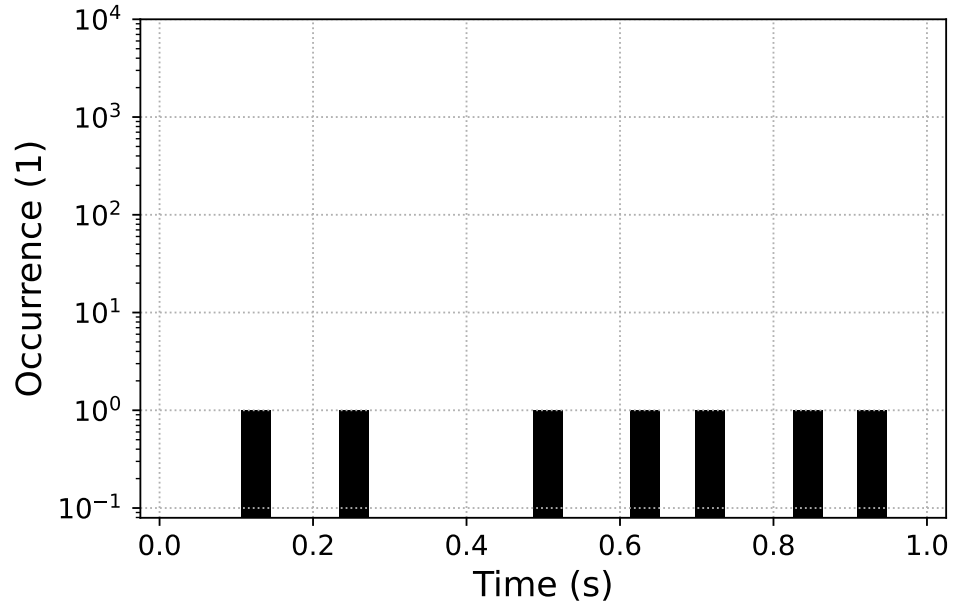
Figure 49 – Total number of Sparks obtained by each realization of the 16x16 STP model simulated without any stimulation by ten seconds.



Source: Created by the author. (2023).

Considering the absence of stimulus, the probability of a Spark occurring is the same over the BCL. This feature was observed in the STP model outputs at 0Hz since the Sparks obtained were homogeneously distributed over the period. Figure 50 shows a histogram with the distribution of the occurrence of the calcium Sparks obtained by simulating the 16x16 STP model without pacing grouped by each fraction of the BCL.

Figure 50 – Distribution of the occurrence of all calcium Sparks encountered by the five realizations of the 16x16 CRUs STP model simulated without pacing over the whole CRU grid.



Source: Created by the author. (2023).

Figure 51 presents the traces of the local  $[Ca]_{i\ free}^u$ ,  $I_{CaL}^u$ , and  $I_{rel}^u$  curves of one BC sample where the Spontaneous calcium Sparks can be seen.

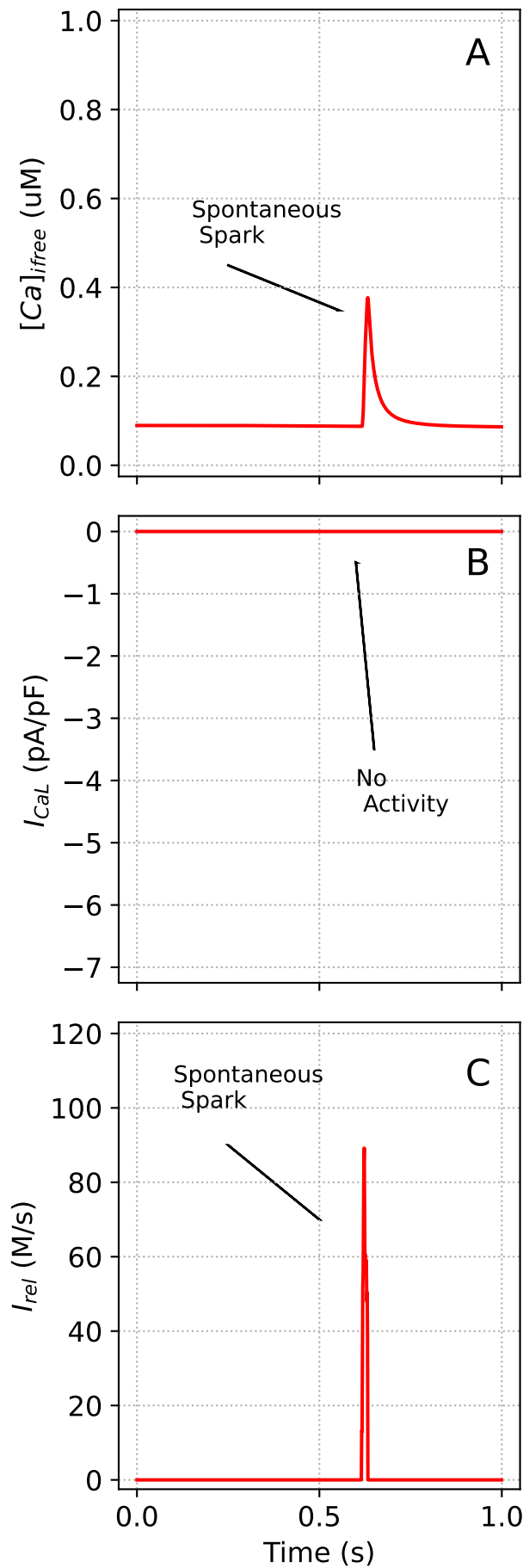


Figure 51 – Traces of the  $[Ca]_{free}^u$ ,  $I_{CaL}^u$ , and  $I_{rel}^u$  values obtained by one CRU  $u$  that compose the 16x16 CRU grid of the STP model simulated under 0Hz stimulation. In this BC sample, as the model was not stimulated, only the Spontaneous calcium Spark can be seen. It can be noted in panels B and C that the calcium Spark occurred exclusively due to the RyR opening; the LCCs remain inactive during the whole BCL.

Source: Created by the author. (2023).

Figure 52 shows distinct moments of the locals  $[Ca]_{i\ free}^u$  dynamics over the time obtained by the STP model simulated without pacing. As the CRUs were expected to remain inactive, the calcium spark observed in the images can be seen as Spontaneous calcium sparks.

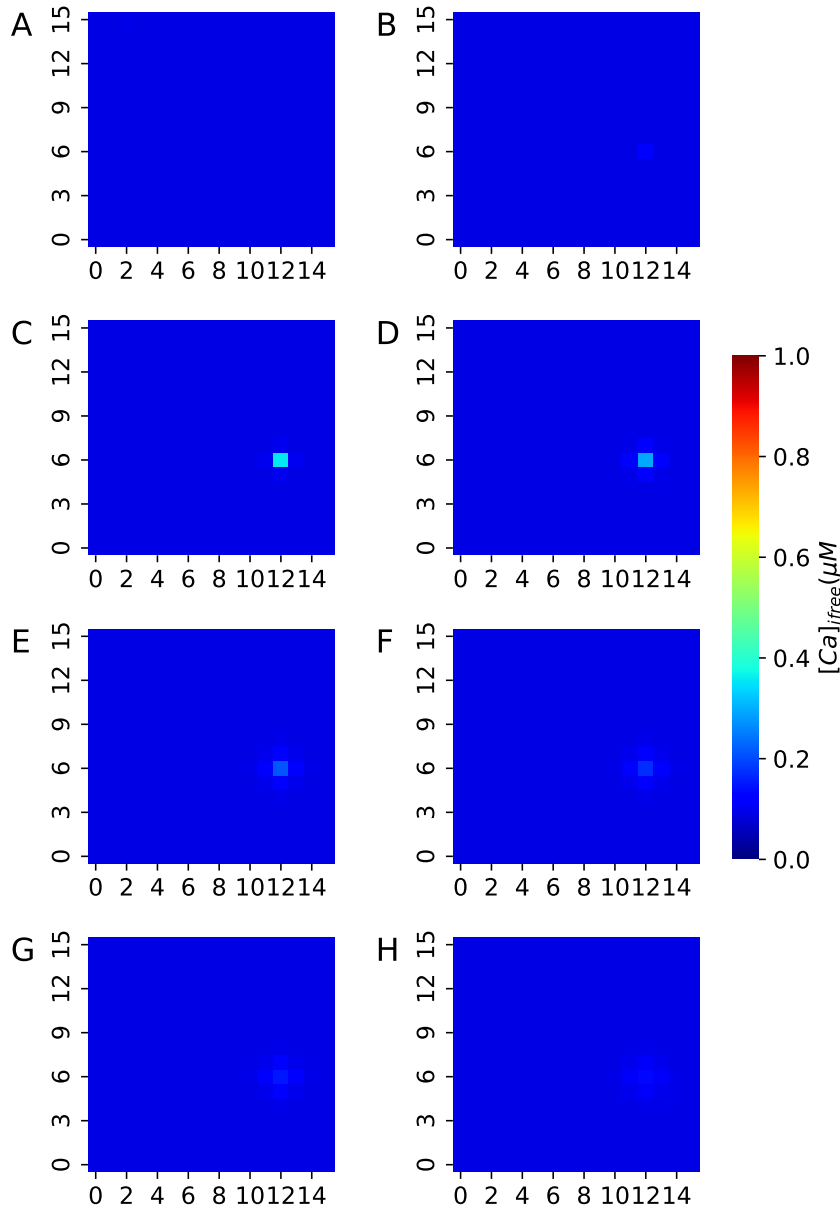
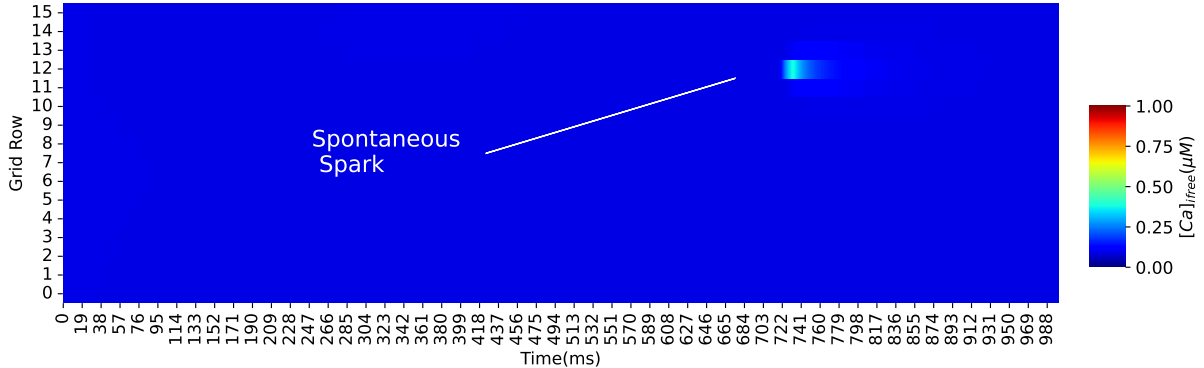


Figure 52 – Sequence of distinct moments of the dynamics of the local variables  $[Ca]_{i\ free}^u(\mu M)$  over 350ms simulated without pacing. The Panels were chronologically organized where Panel A represents the moment  $t = 0ms$ , Panel B represents the moment  $t = 50ms$ , Panel C represents the moment  $t = 100ms$ , up to Panel H that represents the moment  $t = 350ms$ .

The same linescan-type image can be done for this simulation. Figure 53 shows the Spontaneous Spark in linescan-type image from the 6th row of the 16x16 CRU grid over one second of simulation.

Figure 53 – Linescan image of the 6th row of the 16x16 CRU grid that compose the STP model obtained by one second of simulation.

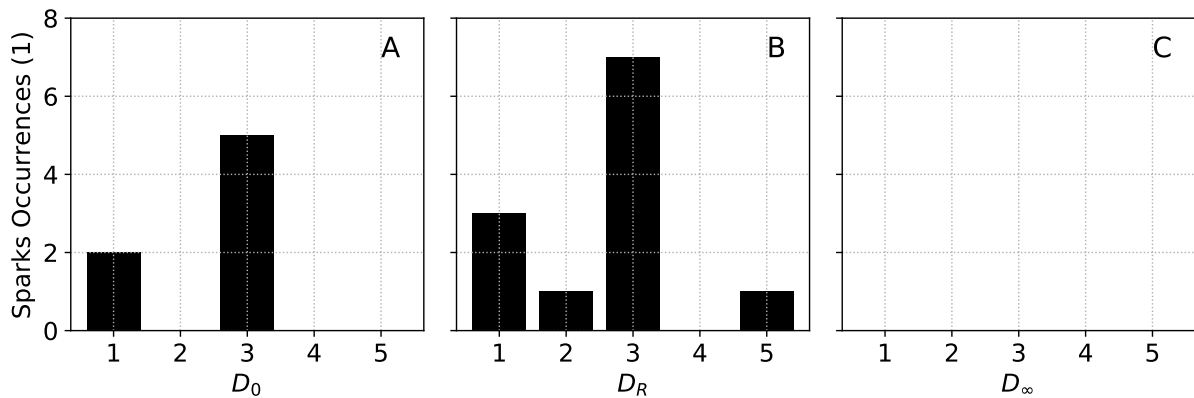


Source: Created by the author. (2023).

Concerning the effects of the calcium ion Diffusion, the outputs obtained by simulating the STP model without pacing presented the same behavior as encountered in 1Hz outputs. As shown in Figure 54, the  $D_0$  scenario presented less number of Sparks than the  $D_R$ . Furthermore, the  $D_\infty$  condition obtained zero occurrences of calcium Sparks. This absence of Spontaneous sparks at  $D_\infty$  condition was precisely what happened with the outputs obtained in the realizations under 1Hz considering the same condition.

Figure 54 presents the number of calcium Sparks and their relation with the calcium ion diffusion.

Figure 54 – Comparison of the total number of calcium Sparks obtained in the STP model composed by the 16x16 CRU grid simulated by ten seconds at 0Hz pacing under the three diffusion conditions:  $D_0$  (A),  $D_R$  (B), and  $D_\infty$  (C).



Source: Created by the author. (2023).

## 5 DISCUSSIONS

The main objective of this thesis was to develop a novel computational model for human left ventricle myocyte capable of reproducing the CICR process in a multiscale approach. Historically, computational models for cardiac electrophysiology were developed based on a “common pool” idea that merges all the thousands of intracellular structures in a single representation (2). This assumption simplified the model elaboration but, in contrast, led to limitations in its application. The traditional cellular models are well-accepted and widely used to replicate the general activities of the cell. They can reproduce the cell phenomena on a macro scale point of view. On the other hand, over the last few years, the advances in experimental imaging modalities enabled the reconstruction of intracellular structures by super-resolution imaging at the nanometer scale (18). Potentialized by these new imaging techniques, the Computational Modeling field can contribute to understanding the micro scale underlying the overall cellular function(18).

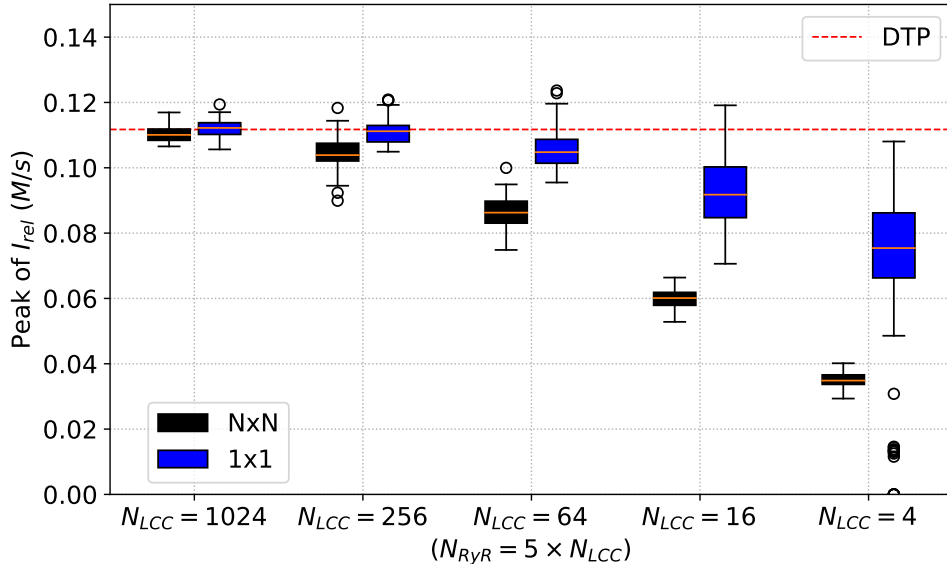
### 1x1 STP Model

In this context, the STP model presented in this thesis is a promising tool for analyzing this multiscale correlation. As shown in Section 4.2.1, the 1x1 version of the STP model could, by changing the number of LCCs and RyRs inside the single CRU, accurately reproduce the stochasticity expected in micro scale and also the deterministic outputs observed in the macro scale. This multiscale feature is dependent only on two parameters in the model: the  $N_{LCC}$  and the  $N_{RyR}$ . It is an evident positive feature of the 1x1 STP model. For instance, it could be used to test the effects of a drug that inhibits a specific ion channel at macro scale and then check the impact of this inhibition on the micro scale by varying the number of LCCs and RyRs.

### NxN STP Model - Macro Scale

As presented in Sction 4.2.2, the results obtained by the NxN STP model expected for reproducing the macro scale outputs (the deterministic outputs) were not good. Initial analysis indicated that the reduction in the  $I_{rel}$  currents led to a considerable decrease in the peak of the  $[Ca]_{ifree}$  transients (Figures 40 and 41). This behavior was unexpected, but it could be explained when combined with the outputs obtained by the 1x1 STP model. Figure 55 presents side by side the Descriptive Measures of the Peak values of the  $I_{rel}$  currents for both NxN and 1x1 STP model varying the  $N_{LCC}$  value.

Figure 55 – Descriptive Measures of the peak values of the  $I_{rel}$  current obtained by the simulation of the spatial NxN STP model (1x1, 2x2, 4x4, 8x8, and 16x16) in comparison with same measures obtained by the simulation of the 1x1 STP model.



Source: Created by the author. (2023).

Based on Figure 55, it was found that the coupling of the local  $\bullet_i$  and  $\bullet_{SR}$  media among the CRUs through the diffusion term was not enough to replicate the global deterministic behavior. The NxN CRUs presented similar behaviors to the single CRU present in 1x1 STP model when both had varying  $N_{LCC}$  value. This behavior was unexpected, but it could be explained when combined with the information presented in Section 4.2.1, Figure 36. As shown in Figure 36, the amount of calcium released by the  $I_{rel}$  current over the BCL decreases as the  $N_{LCC}$  drops. Considering the 16x16 grid conformation, it has 256 CRUs composed of  $N_{LCC}^u = 4$ . Figure 36 shows that the amount of calcium released through the  $I_{rel}$  was considerably smaller than expected by the deterministic version (DTP). So, all individual CRUs composed of 4 LCCs released less calcium into the cytosol. In this way, it is reasonable that the global value for this variable had decreased. In other words, the diffusion factors in the  $\bullet_i$  and  $\bullet_{SR}$  medium could not make the coupling between the NxN CRUs, and they behaved as NxN-independent structures. In this way, it explains that the NxN STP model replicated the 1x1 behavior.

Reviewing the assumptions made by the NxN version of the STP model, a subtle definition might contributed to this unexpected limitation of the NxN STP model in reproducing the macro scale outputs. As described in Section 3.2.2, the calcium diffusion was implemented only in the intracellular ( $\bullet_i$ ) and sarcoplasmic reticulum ( $\bullet_{SR}$ ) medium. There was no diffusion in the subspace ( $\bullet_{ss}$ ) medium. Conceptually, the  $\bullet_{ss}$  medium is precisely where the LCC and RyR are located. So, all calcium release thought the local  $I_{rel}^u$  current fills this medium. This way, without calcium diffusion in the  $\bullet_{ss}$ , a local calcium

release would never influence the next CRUs. On the contrary, considering that the RyR opening is regulated by the presence of calcium ions in its medium, it is reasonable to infer that the calcium diffusion in the  $\bullet_{ss}$  medium would lead to a more expressive activation of the local RyR and, thus, of the  $I_{rel}^u$  current. Therefore, although the CRU units were coupled via calcium diffusion within the  $\bullet_i$  and  $\bullet_{SR}$  mediums, this coupling was weak in that they still behaved as independent random variables.

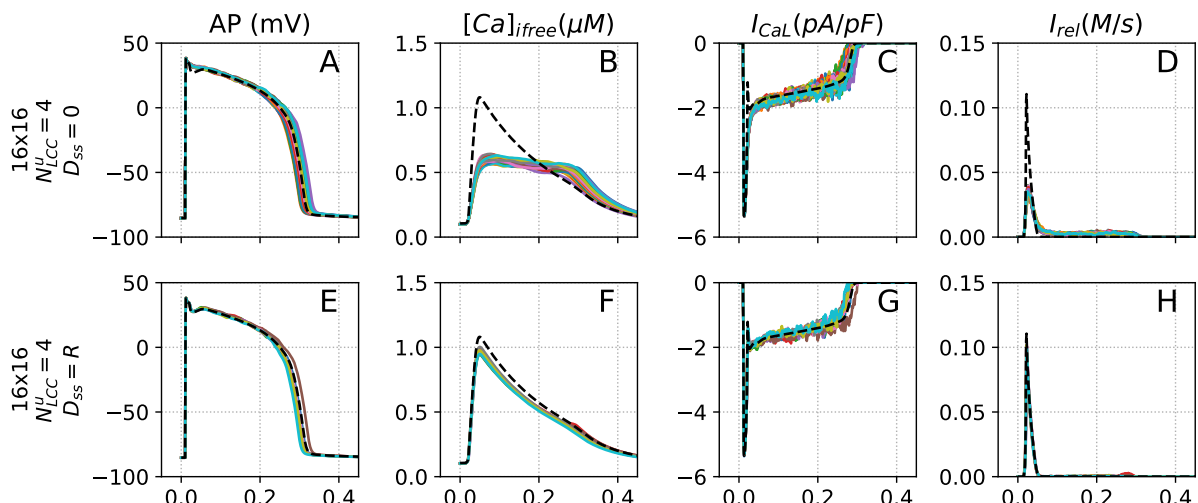
The 16x16 STP model was reimplemented to test this hypothesis and the diffusion term  $\nabla \cdot J_{ss}^u$  was added in the  $[Ca]_{ss}^u$  dynamics. The methods used in this implementation were the same as those used in the  $[Ca]_i^u$  and  $[Ca]_{SR}^u$  equations (Section 3.1.5). Thus, based on the original TP formulation, the PDE equation for the  $[Ca]_{ss}^u$  dynamics reads

$$\frac{\partial [Ca]_{ss}^u}{\partial t} = -\frac{I_{CaL}^u}{2V_{ss}F} + \frac{V_{sr}}{V_{ss}} I_{rel}^u - \frac{V_c}{V_{ss}} I_{xfer}^u + D_{ss} \Delta [Ca]_{ss free}^u. \quad (5.1)$$

In the same way as done for the  $[Ca]_i^u$  and  $[Ca]_{SR}^u$  dynamics, it was considered the Neumann Boundary condition for the  $[Ca]_{ss}^u$  formulations.

A set of five realizations were performed considering the diffusion within the  $\bullet_{ss}$  medium. The realizations were done defining  $D_{ss} = D_i = 0.4 \mu m^2/ms$  and a pacing rate of 1Hz. Figure 56 presents the traces obtained by the simulation of the 16x16 STP model considering the diffusion in the  $\bullet_{ss}$  medium in contrast with the same 16x16 STP but without considering the diffusion on  $\bullet_{ss}$ .

Figure 56 – Output curves of the AP,  $[Ca]_{ifree}$ ,  $I_{CaL}$  and  $I_{rel}$ . The results present the outputs of the 16x16 STP model with the implementation of the calcium diffusion on the  $\bullet_{ss}$  medium (panels A-D); and considering the implementation of the diffusion in the space (panel E-F). For each N there are presented  $n = 50$  samples. In contrast, there are presented also the output traces from the DTP model (black line).

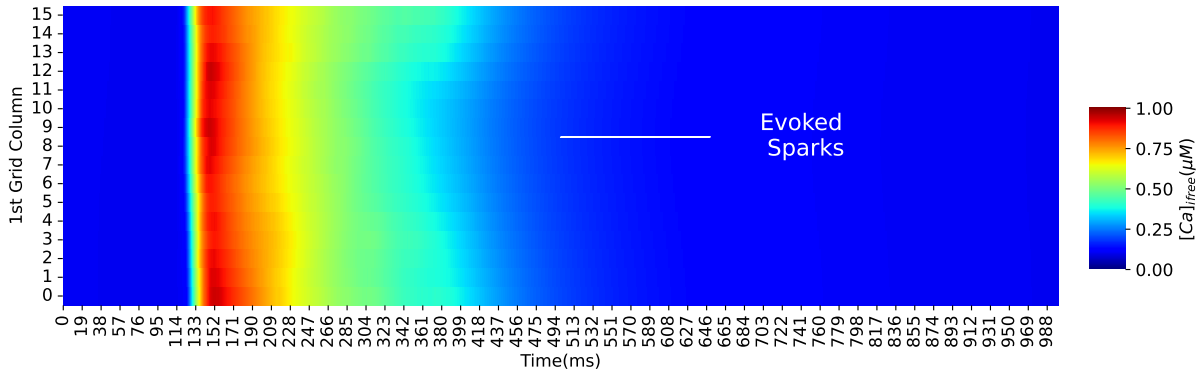


Source: Created by the author. (2023).

As shown in Figure 56, implementing the realistic values for the diffusion within the  $\bullet_{ss}$  medium improved the capacity of the NxN STP model to reproduce the macro scale. It indicates that the diffusion within the  $\bullet_{ss}$  medium is important and requires further studies.

Figure 57 presents the linescan-type image of an arbitrary row of the 16x16 CRU grid obtained by simulating of the STP model considering the diffusion in the  $\bullet_{ss}$  medium.

Figure 57 – Linescan-type image of an arbitrary row of the 16x16 CRU grid obtained by simulating of the STP model considering the diffusion in the  $\bullet_{ss}$  medium. The outputs were obtained by defining  $D_{ss} = D_i = 0.4\mu\text{m}^2/\text{ms}$  and a pacing rate of 1Hz



Source: Created by the author. (2023).

### NxN STP Model - Micro Scale

Although the initial limitation of the NxN STP model of reproducing the macro scale outputs (represented by the STP outputs), the results obtained by its simulations for the micro scale were exciting. The model could reproduce the two kinds of calcium sparks defined in literature: the Evoked and the Spontaneous Sparks(15). Besides the qualitative analyses, considering the grid size, the occurrence of the Spontaneous Sparks obtained by the 16x16 STP model realizations followed the expected values presented in the literature (25).

### Related Works

Recent studies have been developed to elucidate the mechanisms that link the two opposite scales (2, 19, 18). The study developed by Alvarez et al. (2) presents a stochastic computational model built to reproduce the intracellular  $\text{Ca}^{2+}$  dynamics, spark regulation, and frequency-dependent changes for a human ventricular myocyte. The construction of the model was also based on defining a finite number of CRUs that, in turn, were composed of nine LCCs and 49 RyRs. Similar to what was developed in this thesis, the

formulations for the  $I_{CaL}$  and  $I_{rel}$  currents were also implemented using MC formalism. In these formulations, they introduce the stochasticity feature. A considerable difference between the model presented in Alvarez et al. (2) and the model proposed in this thesis is the spatial dimensions. The model developed by Alvarez et al. (2) does not consider the spatial dimensions and, thus, the calcium diffusion. They consider only the time evolution. Comparing these two studies, from Alvarez et al. (2) and this thesis, it can be inferred that they have the same context and similar methods. Considering this thesis finding that calcium diffusion interferes in the micro scale activities, this spatial feature is important for studying the CICR and the calcium Sparks events.

A second correlated study, is the one developed by Colman et al. (19). In their study, Colman et al. (19) presented a new computational model for the human ventricle myocyte. The main feature of the proposed model is the usage of a realistic three-dimensional spatial geometry to represent the cellular domain. Besides this, in the same way, as presented by this thesis study, Colman et al. (19) also considered stochastic-differential-equation based on MC formalism to implement the randomness encountered in micro scales. According to the authors, the model presented in Colman et al. (19) provided a powerful tool for investigating the relationship between structure and function in intracellular calcium handling. It integrates high-resolution 3D images of intracellular structures with models of calcium cycling, enabling direct assessment of the impact structural remodeling has on cellular function. From the point of view of this thesis proposal, the two-dimensional STP model presents a differential when compared with Colman et al. (19) model. The presence of the parameters  $N_{LCC}$ ,  $N_{RyR}$ , and 'N' within the NxN STP model offers the possibility of doing computational experiments connecting the micro and macro scales. The unique NxN STP model can change its conformation to be adapted to perform simulations in the micro or macro scales and between these extremes. The study developed by Colman et al. (19) reproduces in detail the micro scale and, by simulating the AP, also the macro scale. However, the study does not address the pathway between these two extremes.

In summary, this thesis study can be placed in between the Alvarez et al. (2) and Colman et al. (19) studies. From Alvarez et al. (2), it presented a simplified stochastic model capable of reproducing a human ventricle myocyte's micro and macro scales without considering the diffusion factor. From Colman et al. (19), it presented a complete model based on a high-resolution three-dimensional spatial domain capable of reproducing the micro and macro scales outputs, including considering the diffusion effect. But it does not simulate the pathway between these two extremes. This thesis STP model is a third approach. It considers the spatial calcium diffusion, it is capable of simulating the two extreme scales, the subcellular and cellular levels, and it also can reproduce the cellular behavior between these two extremes.

## Limitations and Future Works

The initial assessment of the NxN STP model concerning the diffusion terms proved harmful for the model to reproduce the macro scale outputs. As a brief experiment, Figure 56 presented the improvement of the 16x16 STP outputs caused by adding the diffusion factor into the  $\bullet_{ss}$  medium. Therefore, analyzing the diffusion terms and their respective variables needs more tests to adequately replicate the effect of each of the three mediums' diffusion on the whole cell.

In future works, the main activity must adequately study the diffusion phenomena. A study analyzing the magnitude of each specific diffusion could generate important findings about the relation between the diffusion terms, the local and the global variables.

Another future work must be reimplementing the whole model code using CUDA technology(42). The original implementation used the MPI to boost the execution time. However, the MPI presents limitations due to the number of CPUs available to perform the simulation. Using CUDA technology, the execution of the code could extract even more from the parallelization technologies. Furthermore, this increase in execution capacity would enable the model to simulate higher NxN conformations.

Besides that, a study to do sensitive analyses of the main parameters of the STP model could offer a better an understanding of the main variables and parameters of the model.

## 6 CONCLUSION

Reaching this thesis's primary goal, the proposed STP model could adequately reproduce the multiscale feature considering both the subcellular and cellular levels and the pathway between these two extremes. Under a micro scale conformation, the model outputs presented the expected stochastic behavior, including the emergence of Evoked and Spontaneous calcium Sparks. On the opposite, the STP model also reproduced the expected deterministic results.

Success in the specific objectives was crucial to achieve the main goal. The generation of the MC-based  $I_{CaL}$  model propitiated the insertion of the random variables into the new model, generating, thus, a Stochastic version of the DTP model. In this step, the DE fitting algorithm effectively found the optimum set of parameters that restored the desired outputs of the new DTP model. The framework used to generate the final DTP model showed a considerable gain in the scientific community, and the whole process was published. In possession of a consolidated DTP model composed of LCC and RyR formulations based on MC formalism, combined with random variables, constructing the STP model version was a natural process. Stochastic differential equations composed of random variables replaced all the deterministic ODEs of the MC formulations. This natural replacement, combined with the  $N_{LCC}$  and  $N_{RyR}$  parameters, carried to the STP model the notable capacity to perform simulations on both subcellular and cellular scales and between these extremes. As presented in the results section, this STP model could reproduce the stochastic nature of the subcellular level. Furthermore, the same STP model could gradually replicate the deterministic behavior when simulated under higher-scale conditions. This link between the two extreme scales was the main differential of the STP model when compared with similar studies in the literature.

Going ahead with implementing the spatial CRU grid, the NxN STP acquired the possibility to consider an expressive physical condition in cellular physiology: ionic diffusion. With the two-dimensional approximation of the cellular domain achieved by implementing the NxN CRU grid, the spatial version of the STP model could also evaluate the effects of the calcium diffusion on the main phenomena of the CICR process, for instance, the calcium spontaneous sparks. Such was important the implementation of this spatial version that the initial assumption that the  $\bullet_{ss}$  calcium ions would not diffuse generated unexpected results. Combining the 1x1 STP model findings with the NxN results, it was observed that the diffusion in the  $\bullet_{ss}$  medium also plays a crucial role in the CICR process in different scales. This revision was potentialized by the STP model's capacity to simulate the same phenomena in different scales. This revision indicates the importance of future research to evaluate the expression of each calcium medium in the whole CICR process. By reproducing adequately the experiments observed in the literature, both the 1x1 and NxN STP models were shown to be promising tools to contribute to

understanding the underlying mechanisms at a subcellular level and their correlation to the whole cardiac organ. In conclusion, this thesis's initial objectives were achieved in completeness.

With the concepts and methods used to develop this study, altogether, three correlated contributions were published(41, 40, 35).

## REFERENCES

- 1 , . The top 10 causes of death — who.int. <https://www.who.int/news-room/fact-sheets/detail/the-top-10-causes-of-death>. [Accessed 20-08-2023].
- 2 Alvarez, J.A.E., Jafri, M.S., Ullah, A., 2023. Local control model of a human ventricular myocyte: An exploration of frequency-dependent changes and calcium sparks. *Biomolecules* 13. URL: <https://www.mdpi.com/2218-273X/13/8/1259>, doi:10.3390/biom13081259.
- 3 Baddeley, D., Jayasinghe, I., Lam, L., Rossberger, S., Cannell, M.B., Soeller, C., 2009. Optical single-channel resolution imaging of the ryanodine receptor distribution in rat cardiac myocytes. *Proceedings of the National Academy of Sciences* 106, 22275–22280.
- 4 Bers, D., 2001. Excitation-contraction coupling and cardiac contractile force. volume 237. Springer Science & Business Media.
- 5 Bers, D.M., 2002. Cardiac excitation–contraction coupling. *Nature* 415, 198–205.
- 6 Bers, D.M., Stiffel, V.M., 1993. Ratio of ryanodine to dihydropyridine receptors in cardiac and skeletal muscle and implications for ec coupling. *American Journal of Physiology-Cell Physiology* 264, C1587–C1593.
- 7 Best, J.M., Kamp, T.J., 2012. Different subcellular populations of l-type ca<sub>2+</sub> channels exhibit unique regulation and functional roles in cardiomyocytes. *Journal of molecular and cellular cardiology* 52, 376–387.
- 8 Biscani, F., Izzo, D., Jakob, W., GiacomoAcciarini, Märtens, M., C, M., Mereta, A., Kaldemeyer, C., Lyskov, S., Corlay, S., acxz, Pritchard, B., Manani, K., Mabille, J., Acciarini, G., Webb, O., Huebl, A., v. Looz, M., López-Ibáñez, M., jakirkham, Lee, J., hulucc, polygon, Travers, J., Jordan, J., Smirnov, I., Nguyen, H., Lema, F., O’Leary, E., Mambrini, A., 2020. esa/pagmo2: pagmo 2.15.0. URL: <https://doi.org/10.5281/zenodo.3738182>, doi:10.5281/zenodo.3738182.
- 9 Bouhlel, M.A., Hwang, J.T., Bartoli, N., Lafage, R., Morlier, J., Martins, J.R.R.A., 2019. A python surrogate modeling framework with derivatives. *Advances in Engineering Software* , 102662doi:<https://doi.org/10.1016/j.advengsoft.2019.03.005>.
- 10 Cannell, M., Cheng, H., Lederer, W., 1994. Spatial non-uniformities in [ca<sub>2+</sub>] i during excitation-contraction coupling in cardiac myocytes. *Biophysical journal* 67, 1942–1956.
- 11 Cannell, M., Crossman, D., Soeller, C., 2006. Effect of changes in action potential spike configuration, junctional sarcoplasmic reticulum micro-architecture and altered t-tubule structure in human heart failure. *Journal of Muscle Research & Cell Motility* 27, 297–306.
- 12 Caradec, P.D., Martorano, M.A., 2013. Modelo matemático determinístico-estocástico para previsão da macroestrutura bruta de solidificação sob efeito da decantação de grãos. *Tecnologia em Metalurgia, Materiais e Mineração* 9, 132–139.

- 13 CellML, 2008. The cellml model repository. URL:  
<https://models.cellml.org/exposure/de5058f16f829f91a1e4e5990a10ed71>.
- 14 CellML, I.P.P., 2015. physiomeproject.org. URL:  
[https://models.physiomeproject.org/exposure/ea62c9c8a502afe364350d353ebf4dd5/pandit\\_clark\\_giles\\_demir\\_2001\\_epicardial\\_cell.cellml/view](https://models.physiomeproject.org/exposure/ea62c9c8a502afe364350d353ebf4dd5/pandit_clark_giles_demir_2001_epicardial_cell.cellml/view).
- 15 Cheng, H., Lederer, W., 2008. Calcium sparks. *Physiological reviews* 88, 1491–1545.
- 16 Cheng, H., Lederer, W.J., Cannell, M.B., 1993. Calcium sparks: elementary events underlying excitation-contraction coupling in heart muscle. *Science* 262, 740–744.
- 17 Collier, M., Ji, G., Wang, Y.X., Kotlikoff, M., 2000. Calcium-induced calcium release in smooth muscle: loose coupling between the action potential and calcium release. *The Journal of general physiology* 115, 653–662.
- 18 Colman, M.A., Alvarez-Lacalle, E., Echebarria, B., Sato, D., Sutanto, H., Heijman, J., 2022. Multi-scale computational modeling of spatial calcium handling from nanodomain to whole-heart: Overview and perspectives. *Frontiers in physiology* 13, 278.
- 19 Colman, M.A., Pinali, C., Trafford, A.W., Zhang, H., Kitmitto, A., 2017. A computational model of spatio-temporal cardiac intracellular calcium handling with realistic structure and spatial flux distribution from sarcoplasmic reticulum and t-tubule reconstructions. *PLoS computational biology* 13, e1005714.
- 20 Courtemanche, M., Ramirez, R., Nattel, S., 1998. Ionic mechanisms underlying human atrial action potential properties: insights from a mathematical model. *Am J Physiol Heart Circ Physiol* .
- 21 Dangerfield, C., Kay, D., Burrage, K., 2010. Stochastic models and simulation of ion channel dynamics. *Procedia Computer Science* 1, 1587–1596.
- 22 Frontera, W.R., Ochala, J., 2015. Skeletal muscle: a brief review of structure and function. *Calcified tissue international* 96, 183–195.
- 23 Galice, S., Xie, Y., Yang, Y., Sato, D., Bers, D.M., 2018. Size matters: ryanodine receptor cluster size affects arrhythmogenic sarcoplasmic reticulum calcium release. *Journal of the American Heart Association* 7, e008724.
- 24 Gomes, J.M., 2019. Using delay differential equations in models of cardiac electrophysiology. Ph.D. thesis. Universidade federal de Juiz de Fora.
- 25 Guatimosim, S., Guatimosim, C., Song, L.S., 2011. Imaging calcium sparks in cardiac myocytes. *Light Microscopy: Methods and Protocols* , 205–214.
- 26 Hall, J.E., 2015. Guyton and Hall textbook of medical physiology e-Book. Elsevier Health Sciences.
- 27 Henriquez, C.S., 2014. A brief history of tissue models for cardiac electrophysiology. *IEEE Transactions on Biomedical Engineering* 61, 1457–1465.
- 28 Hoang-Trong, T.M., Ullah, A., Jafri, M.S., 2015. Calcium sparks in the heart: dynamics and regulation. *Research and reports in biology* , 203–214.

- 29 Hodgkin, A.L., Huxley, A.F., 1952. A quantitative description of membrane current and its application to conduction and excitation in nerve. *The Journal of physiology* 117, 500.
- 30 Hou, Y., Jayasinghe, I., Crossman, D.J., Baddeley, D., Soeller, C., 2015. Nanoscale analysis of ryanodine receptor clusters in dyadic couplings of rat cardiac myocytes. *Journal of molecular and cellular cardiology* 80, 45–55.
- 31 Institute for Quality and Efficiency in Health Care, 2019. How does the blood circulatory system work? URL:  
<https://www.ncbi.nlm.nih.gov/books/NBK279250/>.
- 32 Jayasinghe, I., Clowsley, A.H., De Langen, O., Sali, S.S., Crossman, D.J., Soeller, C., 2018a. Shining new light on the structural determinants of cardiac couplon function: insights from ten years of nanoscale microscopy. *Frontiers in Physiology* 9, 1472.
- 33 Jayasinghe, I., Clowsley, A.H., Lin, R., Lutz, T., Harrison, C., Green, E., Baddeley, D., Di Michele, L., Soeller, C., 2018b. True molecular scale visualization of variable clustering properties of ryanodine receptors. *Cell Reports* 22, 557–567.
- 34 Keener, J., Sneyd, J., 2009. Mathematical physiology: II: Systems physiology. Springer.
- 35 Lei, C.L., Ghosh, S., Whittaker, D.G., Aboelkassem, Y., Beattie, K.A., Cantwell, C.D., Delhaas, T., Houston, C., Novaes, G.M., Panfilov, A.V., et al., 2020. Considering discrepancy when calibrating a mechanistic electrophysiology model. *Philosophical Transactions of the Royal Society A* 378, 20190349.
- 36 Mahajan, A., Shiferaw, Y., Sato, D., Baher, A., Olcese, R., Xie, L.H., Yang, M.J., Chen, P.S., Restrepo, J.G., Karma, A., et al., 2008. A rabbit ventricular action potential model replicating cardiac dynamics at rapid heart rates. *Biophysical journal* 94, 392–410.
- 37 Moreno, C., De la Cruz, A., Valenzuela, C., 2016. In-depth study of the interaction, sensitivity, and gating modulation by pufas on k<sup>+</sup> channels; interaction and new targets. *Frontiers in Physiology* 7, 578.
- 38 NobelPrize.org, 2022. The nobel prize in physiology or medicine 1963. URL:  
<https://www.nobelprize.org/prizes/medicine/1963/summary/>.
- 39 Noble, D., 2002. Modeling the heart—from genes to cells to the whole organ. *Science* 295, 1678–1682.
- 40 Novaes, G.M., Alvarez-Lacalle, E., Muñoz, S.A., Dos Santos, R.W., 2022. An ensemble of parameters from a robust markov-based model reproduces l-type calcium currents from different human cardiac myocytes. *Plos one* 17, e0266233.
- 41 Novaes, G.M., Campos, J.O., Alvarez-Lacalle, E., Muñoz, S.A., Rocha, B.M., dos Santos, R.W., 2019. Combining polynomial chaos expansions and genetic algorithm for the coupling of electrophysiological models, in: International Conference on Computational Science, Springer. pp. 116–129.
- 42 NVIDIA, Vingelmann, P., Fitzek, F.H., 2020. Cuda, release: 10.2.89. URL:  
<https://developer.nvidia.com/cuda-toolkit>.

- 43 O'Hara, T., Virág, L., Varró, A., Rudy, Y., 2011. Simulation of the undiseased human cardiac ventricular action potential: model formulation and experimental validation. *PLoS computational biology* 7, e1002061.
- 44 de Oliveira Campos, J., 2015. Método de lattice Boltzmann para simulação da eletrofisiologia cardíaca em paralelo usando GPU. Master's thesis. Universidade Federal de Juiz Fora.
- 45 Pandit, S.V., Clark, R.B., Giles, W.R., Demir, S.S., 2001. A mathematical model of action potential heterogeneity in adult rat left ventricular myocytes. *Biophysical journal* 81, 3029–3051.
- 46 Pollard, T.D., Weihing, R.R., Adelman, M., 1974. Actin and myosin and cell movement. *CRC critical reviews in biochemistry* 2, 1–65.
- 47 Price, K.V., 2013. Differential evolution. *Handbook of Optimization: From Classical to Modern Approach* , 187–214.
- 48 Priebe, L., Beuckelmann, D., 1998. Simulation study of cellular electric properties in heart failure. *Circ Res* .
- 49 Qu, Z., Hu, G., Garfinkel, A., Weiss, J.N., 2014. Nonlinear and stochastic dynamics in the heart. *Physics reports* 543, 61–162.
- 50 Qu, Z., Yan, D., Song, Z., 2022. Modeling calcium cycling in the heart: Progress, pitfalls, and challenges. *Biomolecules* 12, 1686.
- 51 Rasband, M., 2010. Ion channels and excitable cells. *Nature Education* 3, 41.
- 52 Sachse, F.B., 2004. Computational cardiology: modeling of anatomy, electrophysiology, and mechanics. volume 2966. Springer Science & Business Media.
- 53 Sato, D., Bers, D.M., Shiferaw, Y., 2013. Formation of spatially discordant alternans due to fluctuations and diffusion of calcium. *PloS one* 8, e85365.
- 54 Shannon, T.R., Wang, F., Puglisi, J., Weber, C., Bers, D.M., 2004a. A mathematical treatment of integrated ca dynamics within the ventricular myocyte. *Biophysical journal* 87, 3351–3371.
- 55 Shannon, T.R., Wang, F., Puglisi, J., Weber, C., Bers, D.M., 2004b. A mathematical treatment of integrated ca dynamics within the ventricular myocyte. *Biophysical journal* 87, 3351–3371.
- 56 Shepardson, D., 2009. Algorithms for inverting Hodgkin-Huxley type neuron models. Ph.D. thesis.
- 57 Stern, M.D., Song, L.S., Cheng, H., Sham, J.S., Yang, H.T., Boheler, K.R., Ríos, E., 1999. Local control models of cardiac excitation–contraction coupling: a possible role for allosteric interactions between ryanodine receptors. *The Journal of general physiology* 113, 469–489.
- 58 Sundnes, J., Lee, L.C., Wall, S.T., Valdez-Jasso, D., 2023. Computational models of cardiovascular growth and remodeling. *Frontiers in Physiology* 14, 1130420.

- 59 Teichmann, L., Weise, E., 2014. Simuladores estocástico e determinístico. URL: <https://prezi.com/e6ppo-ebzsns/estocastico-x-deterministico/?frame=508916b1c9f68f5b2ac2f3a3a9ac76f6738d428e>.
- 60 Trayanova, N.A., 2011. Whole-heart modeling: applications to cardiac electrophysiology and electromechanics. *Circulation research* 108, 113–128.
- 61 ten Tusscher, K.H.W.J., Noble, D., J.Noble, P., Panfilov, A.V., 2004. A model for human ventricular tissue. *Am J Physiol Heart Circ Physiol* .
- 62 ten Tusscher, K.H.W.J., Panfilov, A.V., 2006. Alternans and spiral breakup in a human ventricular tissue model. *Am J Physiol Heart Circ Physiol* .
- 63 Warren, B., 2021. Contraction of cardiac muscle. URL: <https://teachmephysiology.com/cardiovascular-system/cardiac-cycle-2/cardiac-muscle-contraction/>.
- 64 Weinhaus, A.J., 2015. Anatomy of the Human Heart. Springer International Publishing, Cham. pp. 61–88. URL: [https://doi.org/10.1007/978-3-319-19464-6\\_5](https://doi.org/10.1007/978-3-319-19464-6_5), doi:10.1007/978-3-319-19464-6\_5.
- 65 Weiss, J.N., Karma, A., Shiferaw, Y., Chen, P.S., Garfinkel, A., Qu, Z., 2006. From pulsus to pulseless: the saga of cardiac alternans. *Circulation research* 98, 1244–1253.
- 66 Zahradníková, A., Zahradník, I., 2012. Construction of calcium release sites in cardiac myocytes. *Frontiers in physiology* 3, 322.

## APPENDIX A – Mathematical Formulation

Since this thesis assumed the ten Tusscher and Panfilov (62) model as the base model, and the main object of study is the CICR process, this section presents the mathematical formulations of the original (62) model associated with the CICR process. To see the other equations, please refer to ten Tusscher et al. (61) and ten Tusscher and Panfilov (62).

Original TP Equations

L-Type  $\text{Ca}^{2+}$  Current

$$I_{\text{Ca}L} = G_{\text{Ca}L} d f f_2 f_{\text{cass}} 4 \frac{(V - 15) F^2}{RT} \frac{0.25 [Ca]_{ss\text{free}} e^{2(V-15)F/RT} - [Ca]_o}{e^{2(V-15)F/RT} - 1} \quad (.1)$$

$$\frac{dd}{dt} = \frac{d_\infty(V) - d}{\tau_d(V)}, \quad (.2)$$

$$\beta_d = \frac{1.4}{1 + e^{(V+5)/5}} \quad (.5)$$

$$d_\infty = \frac{1}{1 + e^{(-8-V)/7.5}} \quad (.3)$$

$$\gamma_d = \frac{1.4}{1 + e^{(50-V)/20}} \quad (.6)$$

$$\alpha_d = \frac{1.4}{1 + e^{(-35-V)/13}} + 0.25 \quad (.4)$$

$$\tau_d = \alpha_d \beta_d + \gamma_d \quad (.7)$$

$$\frac{df}{dt} = \frac{f_\infty(V) - f}{\tau_f(V)}, \quad (.8)$$

$$\beta_f = \frac{200}{1 + e^{(13-V)/10}} \quad (.11)$$

$$f_\infty = \frac{1}{1 + e^{(V+20)/7}} \quad (.9)$$

$$\gamma_f = \frac{180}{1 + e^{(V+30)/10}} + 20 \quad (.12)$$

$$\alpha_f = 1102.5 e^{-(\frac{V+27}{15})^2} \quad (.10)$$

$$\tau_f = \alpha_f + \beta_f + \gamma_f \quad (.13)$$

$$\frac{df_2}{dt} = \frac{f_{2\infty}(V) - f_2}{\tau_{f_2}(V)}, \quad (.14)$$

$$\beta_{f_2} = \frac{31}{1 + e^{(25-V)/10}} \quad (.17)$$

$$f_{2\infty} = \frac{0.67}{1 + e^{(V+35)/7} + 0.33} \quad (.15)$$

$$\gamma_{f_2} = \frac{16}{1 + e^{(V+30)/10}} \quad (.18)$$

$$\alpha_{f_2} = 600 e^{-(\frac{V+25}{170})^2} \quad (.16)$$

$$\tau_{f_2} = \alpha_{f_2} + \beta_{f_2} + \gamma_{f_2} \quad (.19)$$

$$\frac{df_{\text{cass}}}{dt} = \frac{f_{\text{cass}\infty}([Ca]_{ss}) - f_{\text{cass}}}{\tau_{f_{\text{cass}}}([Ca]_{ss})}; \quad (.20)$$

$$f_{cass\infty} = \frac{80}{1 + \left(\frac{[Ca]_{ssfree}}{0.55}\right)^2} + 2 \quad (21)$$

$$\tau_{f_{cass}} = \frac{80}{1 + \left(\frac{[Ca]_{ssfree}}{0.55}\right)^2} + 2 \quad (22)$$

Ryonodine Release Current

$$I_{rel} = V_{rel}O([Ca]_{SRfree} - [Ca]_{i free}) \quad (23)$$

$$O = \frac{k_1[Ca]_{ssfree}^2 \bar{R}}{k_3 + k_1[Ca]_{ssfree}^2} \quad (24)$$

$$\frac{d\bar{R}}{dt} = -k_2[Ca]_{ssfree}\bar{R} + k_4(1 - \bar{R}) \quad (25)$$

$$k_1 = \frac{k'_1}{k_{casr}} \quad (26)$$

$$k_2 = k'_2 k_{casr} \quad (27)$$

$$k_{casr} = max_{sr} - \frac{max_{sr} - min_{sr}}{1 + (EC/[Ca]_{SRfree})^2} \quad (28)$$

Calcium Currents

$$I_{leak} = V_{leak}([Ca]_{SRfree} - [Ca]_{i free}) \quad (29)$$

$$I_{up} = \frac{V_{maxup}}{1 + K_{up}^2/[Ca]_{i free}^2} \quad (30)$$

$$I_{xfer} = V_{xfer}([Ca]_{ssfree} - [Ca]_{i free}) \quad (31)$$

$$I_{bCa} = G_{bCa}(V - E_{Ca}) \quad (32)$$

$$I_{NaCa} = k_{NaCa} \frac{e^{\gamma VF/RT} Na_i^3 [Ca]_o - e^{(\gamma-1)VF/RT} Na_o^3 [Ca]_{i free} \alpha}{(K_{mNa}^3 + Na_o^3)(K_{mCa} + [Ca]_o)(1 + k_{sat}e^{(\gamma-1)VF/RT})} \quad (33)$$

$$I_{pCa} = G_{pCa} \frac{[Ca]_{i free}}{K_{pCa}[Ca]_{i free}} \quad (34)$$

Calcium Concentrations Dynamics

$$\frac{d[Ca]_i}{dt} = -\frac{I_{bCa} + I_{pCa} - 2I_{NaCa}}{2V_c F} + \frac{V_{sr}}{V_c} (I_{leak} - I_{up}) + I_{xfer} \quad (35)$$

$$\begin{cases} [Ca]_{ibuff} = \frac{[Ca]_i \times Buf_i}{[Ca]_i + K_{bufi}}, \\ [Ca]_i = [Ca]_{i free} + [Ca]_{ibuff}, \end{cases} \quad (36)$$

$$\frac{d[Ca]_{SR}}{dt} = (I_{up} - I_{leak} - I_{rel}). \quad (37)$$

$$\begin{cases} [Ca]_{SRbuff} = \frac{[Ca]_{SR} \times Buf_{sr}}{[Ca]_{SR} + K_{bufsr}}, \\ [Ca]_{SR} = [Ca]_{SRfree} + [Ca]_{SRbuff}, \end{cases} \quad (.38)$$

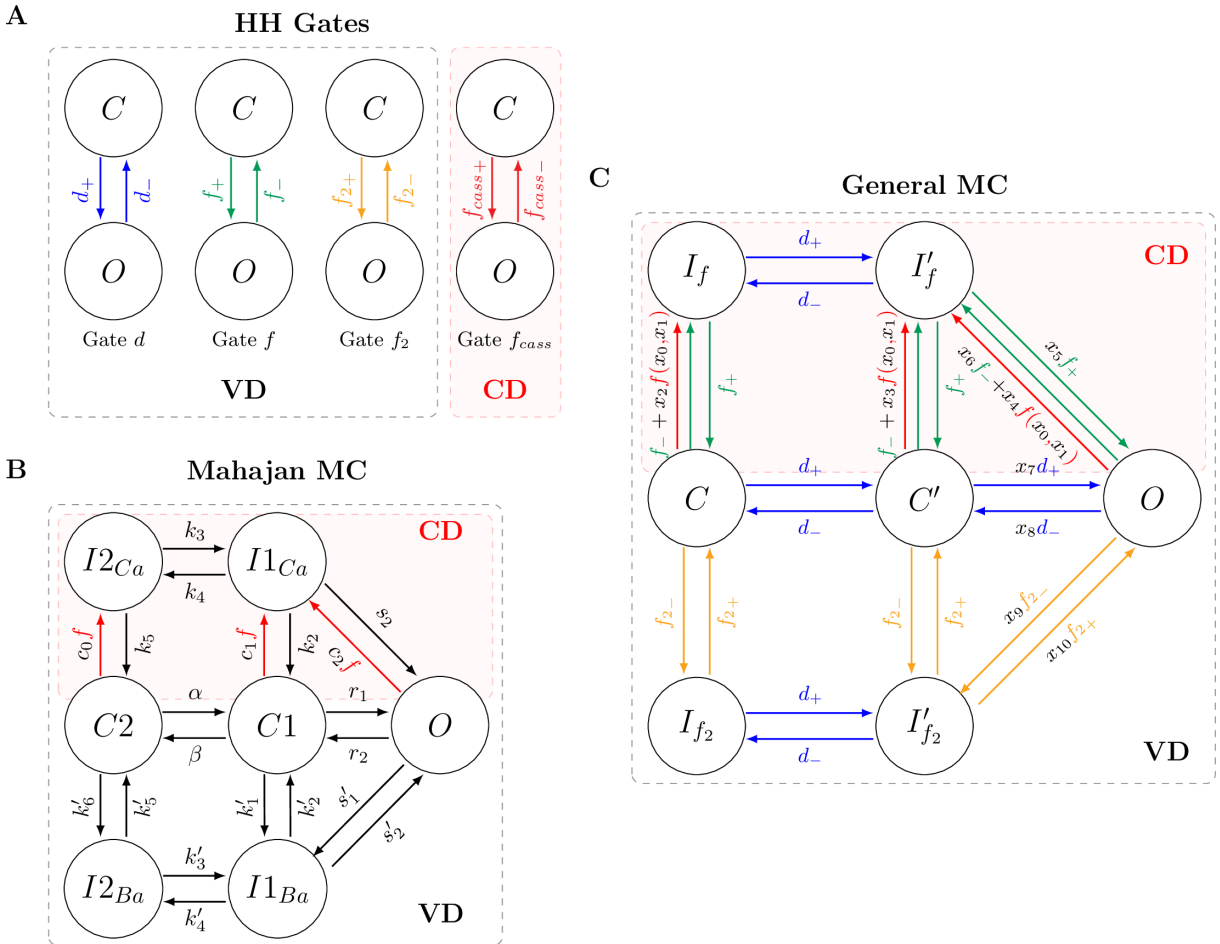
$$\frac{d[Ca]_{ss}}{dt} = -\frac{I_{CaL}}{2V_{ss}F} + \frac{V_{sr}}{V_{ss}}I_{rel} - \frac{V_c}{V_{ss}}I_{xfer} \quad (.39)$$

$$\begin{cases} [Ca]_{ssbuff} = \frac{[Ca]_{ss} \times Buf_{ss}}{[Ca]_{ss} + K_{bufss}}, \\ [Ca]_{ss} = [Ca]_{ssfree} + [Ca]_{ssbuff}. \end{cases} \quad (.40)$$

## APPENDIX B – DTP MC-Based $I_{CaL}$ Formulation

This Appendix introduces the new  $I_{CaL}$  MC-based equations and rates that compose the DTP model proposed in this thesis. It was used the same MC topology used to simulate the  $I_{CaL}$  phenomenon in MJ. They use seven states disposed of three layers being the above one layer, the Calcium Dependence layer. The other two layers are only Voltage Dependence. Fig 58 presents the new MC illustration.

Figure 58 – Schematic representations of the three markov chain structures considered in this study. A: The four independent Markov Chains for each gate of the models TP considering only two possible states, Open ( $O$ ) and Close ( $C$ ) for each one. B: The original structure of the Markov Chain used by MJ to simulate the  $I_{CaL}$  phenomenon. C: The proposed Markov Chain as a combination of the HH formalism rates and the MJ topology, to replace the gates in the TP model. The MC transitions generated considering the HH gates  $d$ ,  $f$ , and  $f_2$  are shown respectively in blue, green, and yellow. The calcium-dependent function  $f$  and the rates associated with the calcium concentration are shown in red. The set of parameters  $\mathbf{x}$  used to fit both calcium-dependent rates (parameters  $x_0$  to  $x_4$ ) and voltage-dependence rates (parameters  $x_5$  to  $x_{10}$ ) are shown in black.



Source: obtained from Novaes et al. (40).

Considering the Calcium-Dependence rate, represented by  $f = f(x_0, x_1, c)$ , it was adapted from MJ. The original  $f(c)$  function used in (36) reads

$$f(c) = \frac{1}{1 + (\bar{c}_p/c)^3}, \quad (.1)$$

where  $c$  is the subcellular calcium concentration ( $[Ca]_{ss}$ ), and  $\bar{c}_p$  is a threshold for calcium dependence.

The rates  $\bullet_+$ , and  $\bullet_-$ , that compose the MC rates, are calculated based in the HH formalism, and they were obtained from the original TP model. Table 3 presents the equations considered in the rates calculations.

### Fitting Parameters

The new Markov Chain was adapted from the HH formalism presented in the original TP model combined with the previous  $I_{CaL}$  formulation originally proposed in MJ. As an adaptation, a fitting process was necessary to adequate the novel MC-based  $I_{CaL}$  dynamics to the original values.

To introduce the adjustable capacity into the new MC, we selected the main rates associated with the channel opening dynamics. For the portion of the dynamics associated with the calcium-dependence, we introduced the adjustable feature in two ways. The first one was to add two fitting parameters,  $x_0$ , and  $x_1$ , in the original MJ  $f$  function, Eq (.1), as the simplest linear combination with the original values. Thereby, our adjustable calcium-dependence rate reads

$$f(c, x_0, x_1) = \frac{1}{1 + (x_0 \bar{c}_p/c)^{x_1 3}}. \quad (.2)$$

Furthermore, to open more possibilities for the fitting algorithm to adjust the calcium-dependence, we also added, as the simplest linear combination, one parameter multiplying the  $f$  function in each transition where it is inserted. As we have three transitions which are composed by the calcium-dependence  $f$  function,  $C \rightarrow I_f$ ,  $C' \rightarrow I'_f$ , and  $O \rightarrow I'_f$ , we added three new parameters,  $x_2$ ,  $x_3$ , and  $x_4$ . Fig 58 presents the calcium-dependence rates in red color.

For the portion of the dynamics associated with the voltage-dependence, we selected the main transitions that are directly associated with the MC opening state,  $I'_f \rightleftharpoons O$ ,  $C' \rightleftharpoons O$ , and  $I'_{f2} \rightleftharpoons O$ . For each rate which composes the transitions, we introduced a fitting parameter  $x$  as the simplest linear combination. Thus, the fitting process is capable to act directly in the main variable of interest: the MC Opening fraction. This method generated a total of seven parameters ( $x_5$  up to  $x_{10}$ ).

Therefore, to introduce the fitting possibility in the new MC, we inserted five parameters associated with the calcium-dependence, and other six parameters associated with the voltage-dependence dynamics.

Table 3 – Formulations of the DTP markov-chain rates.

Rates	TP Models		
	$\bullet_{inf}$	$\tau_{\bullet}$	$\bullet_{-}$
$d$	$d_{inf} = \frac{1}{1+e^{(-8-V)/7.5}}$	$\tau_d = A_d \times B_d + C_d$	$d_+ = d_{inf}/\tau_d$
$f$	$f_{inf} = \frac{1}{1+e^{(V+20)/7}}$	$\tau_f = A_f + B_f + C_f$	$f_+ = f_{inf}/\tau_f$
$f_2$	$f_{2inf} = \frac{0.67}{1+e^{(V+35)/7}} + 0.33$	$\tau_{f_2} = A_{f2} + B_{f2} + C_{f2}$	$f_{2+} = f_{2inf}/\tau_{f2}$
Rates	$A_{\bullet}$	$B_{\bullet}$	$C_{\bullet}$
$d$	$A_d = \frac{1.4}{1+e^{(-35-V)/13}} + 0.25$	$B_d = \frac{1.4}{1+e^{(V+5)/5}}$	$C_d = \frac{1}{1+e^{(50-V)/20}}$
$f$	$A_f = 1102.5e^{(-(V+27)^2/225)}$	$B_f = \frac{200}{1+e^{(13-V)/10}}$	$C_f = \frac{180}{1+e^{(V+30)/10}} + 20$
$f_2$	$A_{f2} = \alpha e^{-(V+\beta)^2/\gamma}$	$B_{f2} = \frac{31}{1+e^{(25-V)/10}}$	$C_{f2} = \frac{\delta}{1+e^{(V+30)/10}}$

Equations used to calculate the rates  $\bullet_+$ , and  $\bullet_-$  that compose the DTP MC-based  $I_{Cal}$  current. For that:  $\alpha = 600$ ,  $\beta = 25$ ,  $\gamma = 170$ , and  $\delta = 16$ .

Source: obtained from Novaes et al. (40).

**ANNEX A – DTP MC-Based  $I_{CaL}$  - Complete Study**

## RESEARCH ARTICLE

# An ensemble of parameters from a robust Markov-based model reproduces L-type calcium currents from different human cardiac myocytes

Gustavo Montes Novaes<sup>1,2,3\*</sup>, Enrique Alvarez-Lacalle<sup>2</sup>, Sergio Alonso Muñoz<sup>2</sup>, Rodrigo Weber dos Santos<sup>1</sup>

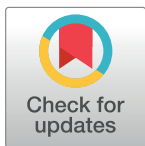
**1** Graduate Program in Computational Modeling, Federal University of Juiz de Fora, Juiz de Fora, MG, Brazil,

**2** Department of Physics, Universitat Politècnica de Catalunya-BarcelonaTech, Barcelona, Spain,

**3** Department of Computation and Mechanics, Federal Center of Technological Education of Minas Gerais, Leopoldina, MG, Brazil

● These authors contributed equally to this work.

\* [gtnmontes@cefetmg.br](mailto:gtnmontes@cefetmg.br)



## OPEN ACCESS

**Citation:** Novaes GM, Alvarez-Lacalle E, Muñoz SA, dos Santos RW (2022) An ensemble of parameters from a robust Markov-based model reproduces L-type calcium currents from different human cardiac myocytes. PLoS ONE 17(4): e0266233. <https://doi.org/10.1371/journal.pone.0266233>

**Editor:** Randall Lee Rasmusson, University at Buffalo - The State University of New York, UNITED STATES

**Received:** August 13, 2021

**Accepted:** March 16, 2022

**Published:** April 5, 2022

**Copyright:** © 2022 Novaes et al. This is an open access article distributed under the terms of the [Creative Commons Attribution License](#), which permits unrestricted use, distribution, and reproduction in any medium, provided the original author and source are credited.

**Data Availability Statement:** All relevant data are within the paper and its [Supporting information](#) files.

**Funding:** The authors received support from MICINN (Spain), and FEDER, Spain (European Union), under project PGC2018-095456-B-I00. EA-L received funding from Spanish Ministerio de Economía, Industria y Competitividad under grant number SAF2017-88019-C3-2-R. GMN was financed in part by the Coordenação de

## Abstract

The development of modeling structures at the channel level that can integrate subcellular and cell models and properly reproduce different experimental data is of utmost importance in cardiac electrophysiology. In contrast to gate-based models, Markov Chain models are well suited to promote the integration of the subcellular level of the cardiomyocyte to the whole cell. In this paper, we develop Markov Chain models for the L-type Calcium current that can reproduce the electrophysiology of two established human models for the ventricular and Purkinje cells. In addition, instead of presenting a single set of parameters, we present a collection of set of parameters employing Differential Evolution algorithms that can properly reproduce very different protocol data. We show the importance of using an ensemble of a set of parameter values to obtain proper results when considering a second protocol that suppresses calcium inactivation and mimics a pathological condition. We discuss how model discrepancy, data availability, and parameter identifiability can influence the choice of the size of the collection. In summary, we have modified two cardiac models by proposing new Markov Chain models for the L-type Calcium. We keep the original whole-cell dynamics by reproducing the same characteristic action potential and calcium dynamics, whereas the Markov chain-based description of the L-type Calcium channels allows novel small spatial scale simulations of subcellular processes. Finally, the use of collections of parameters was crucial for addressing model discrepancy, identifiability issues, and avoiding fitting parameters overly precisely, i.e., overfitting.

## Introduction

The large variability in action potential (AP) and contraction responses in cardiomyocytes not only across different species and cells [1] but also across different individuals [2], has given rise

Aperfeiçoamento de Pessoal de Nível Superior-Brasil (CAPES) - Finance Code 001. This work was partially funded by CNPq, CAPES, FAPEMIG, and UFJF, Brazil. The funders had no role in study design, datacollection and analysis, decision to publish, or preparation of the manuscript. There was no additional external funding received for this study.

**Competing interests:** The authors have declared that no competing interests exist.

to a significant effort to develop models that can properly mimic different action potential dynamics [1, 3–5].

These differences in the cell behavior can be linked with pathologies associated with Atrial Fibrillation [6], Brugada Syndrome [7], or Long-QT [8], among others. The search for these general pro-arrhythmic characteristics in computational models is directly related to the development of proper parameter estimations in order to develop a better understanding of specific channelopathies related to genetic mutations [9]. Experimental measures of the average effect of particular gene mutations such as ΔKPQ or KCNQ1 [10] or genetically modified organism [11] to study dysfunction in contraction due to problems in calcium handling can be used to find key modifications in the parameters space or the need for changes in the structural properties of channels, pumps, or receptors. Therefore, modeling structures at the channel level that can be integrated into different models and properly reproducing different experimental data is of great importance.

Modeling cardiomyocyte channels as Markov Chains presents a clear advantage compared with Hodgkin-Huxley (HH) type models, as the former allows the possibility to model intracellular dynamics. The integration of the variability to analyze cell data from subcellular calcium imaging, patch-clamp, and small tissue leads to computational cellular models that span multiple scales. Specifically, subcellular data of spark activity and structure, or spatial differences in the calcium transient behavior depending on the level of t-tubule structure, cannot be properly analyzed with a HH framework making it impossible to scale up from the micrometer to the millimeter scale. This is especially relevant in the study of excitation-contraction coupling via calcium handling. The key element of this handling is the calcium release units, where a small number of L-type Calcium Channels (LCC) face a cluster of Ryanodine Receptors [12]. A Markov Chain model structure can be used both in a subcellular model of the cardiomyocyte [13] and in a whole-cell approach where these units are coarse-grained. Similarly, the variability in parameters space needed to deal with the variability in behavior is efficiently dealt with by Markov Chain models. More importantly, the parameter space of the different populations can be directly linked with the necessary stochastic nature of calcium handling at the micrometer scale. Following this approach, the analysis of these stochastic subcellular properties have been recently employed to study large-scale organ behavior by introducing the probability distribution of subcellular models into whole-cell models [14].

The inclusion of channel variability into whole-cell organs is particularly relevant to study the effect of differences in calcium handling across animals and patients. Doing so necessarily requires introducing Markov Chain models that can properly reproduce the stochastic subcellular behavior. Different properties of the LCC, the Ryanodine Receptors, the Sodium-Calcium exchanger (NCX), and the SERCA pump have been related with calcium alternans [15, 16]. Similarly, the relevance of calcium handling on the development of Atrial Fibrillation (AF) and its direct association with Heart Failure is very well established [17, 18].

The relevance of the LCCs and the Ryanodine Receptors in calcium handling is very well-known. Calcium-Induced Calcium-Release in the calcium release unit scale is the key to understand calcium alternans [19] in ventricles. Not as a period double-bifurcation, as it is often stated in whole-cell models, but as an order-disorder Ising-like transition [19]. The Ryanodine Receptors are normally portraited as a Markov Chain model with two [20], four [21], or more states in whole-cell models. The same structure is used for subcellular and whole-cell models allowing for direct comparison between them. A whole-cell model where the Ryanodine Receptor has multiple states and its transitions are not stochastic but deterministic can be understood as the limit of having the different calcium release units tightly coupled by calcium diffusion. However, this is not the case for the LCC in most whole-cell models. This prevents

the easy comparison among different length scales and the generation of a collection of parameters that can deal with the different sources of experimental data.

There is a great interest in producing L-type Calcium models that can be integrated into subcellular, whole-cell, and tissue models. The purpose of this manuscript is the development of Markov Chain models that can reproduce AP and intracellular calcium signals both from experiments or from already established models of particular animals or cells. In addition, instead of presenting a single set of parameters for the new model, we propose the use of a collection of parameters, labeled as population, to overcome the limitations usually associated with overfitting.

The goal is to find a collection of the parameters of the L-type Calcium current ( $I_{CaL}$ ) model that can properly match very different protocol data. We show that proper penalty functions and evolutionary algorithms can generate a collection of parameters that can reproduce different protocols. We explain that the approach is sound by replacing two different HH Gate-based  $I_{CaL}$  models of the ventricle and Purkinje human cells with a Markov Chain-based (MC-based) model. We first reproduce all the original model outputs in each case, showing that the Markov Chain structure and the algorithm can match any particular data source. More importantly, we implement different experimental-like protocols to the gate-based models and show how considering a collection of sets of parameter approaches gives the system enough flexibility to fit different data. One of the protocols simulates the condition of Calmodulin mutations associated with long QT syndrome, which is known to promote proarrhythmic behavior in ventricular myocytes.

We develop a general procedure to generate a collection of parameters. We use well-established models to make the reasoning clear. However, the same method can be used to reproduce different experimental data on calcium handling, not only by measuring the interaction between calcium and voltage measures but also from single-channel data or any other type of interaction or protocol employed.

In addition, we also discuss how model discrepancy, data availability, and parameter identifiability can influence the choice of the size of the collection of parameters. By acknowledging the existence of model discrepancy and identifiability issues, the use of higher tolerances after the fitting process may avoid fitting parameters overly precisely, i.e., overfitting.

## Materials and methods

### Cardiac models

An extensively employed mathematical model based in a Markov Chain (MC) description to simulate the electrophysiology of cardiac cells is described in Mahajan et al. [22]. The main objective of the model presented in Mahajan et al. [22] is the accurately reproduction of the cardiac AP and the Intracellular Calcium Cycling at rapid heart rates. Starting from a previous rabbit cardiac model [21], Mahajan et al. [22] modified the formulation of the  $I_{CaL}$  current by replacing it with a seven-state Markovian model. The  $I_{CaL}$  equation proposed by Mahajan et al. [22] reads

$$I_{CaL} = P_o \times \bar{g}_{Ca} \frac{4P_{Ca} VF^2 c_s e^{2(VF/RT)} - 0.341 [Ca^{2+}]_o}{RT} \frac{c_s e^{2(VF/RT)} - 1}{e^{2(VF/RT)} - 1}, \quad (1)$$

where  $P_o$  is the Opening fraction of the channels (represented by the Markovian Open state),  $\bar{g}_{Ca}$  is the maximum conductivity parameter,  $V$  is the transmembrane potential, and  $c_s$  is the submembrane calcium concentration. The other terms are parameters of the model or physical constants.

However, there are also many models that use HH Gate-based descriptions for the  $I_{CaL}$  formulations. Such models have been extensively employed in the modeling of cardiac tissue at large spatial scales. We consider here two typical examples of these models: [23, 24] employed for ventricular tissue and Purkinje Fibers, respectively.

The first consolidated cardiac computational model is the Ten Tusscher and Panfilov [23]. This model, initially developed in [25], simulates the electrophysiology of the left ventricular cells of humans. Different from the description adopted by Mahajan et al. [22], the Ten Tusscher and Panfilov [23] model uses HH Gate-based structures to compose the  $I_{CaL}$  formulation. It is based in the combination of three voltage-dependent gates with another calcium-dependent gate to simulate the opening fraction of the LCC.

The second consolidated cardiac model used here is the Stewart et al. [24]. The model is based on Ten Tusscher and Panfilov [23] with modifications to simulate the electrophysiology of the human Purkinje fibers cells.

Both models, Ten Tusscher and Panfilov [23], and Stewart et al. [24], adopted the HH Gate-based approach to simulate the opening fraction dynamics of the  $I_{CaL}$  current. Rearranging the terms,  $I_{CaL}$  equation for both models reads

$$I_{CaL} = dff_2 f_{cass} \times G_{CaL} \frac{4(V - 15)F}{RT} \frac{0.25c_{ss}e^{2(V-15)F/RT} - [Ca^{2+}]_o}{e^{2(V-15)F/RT} - 1}, \quad (2)$$

where  $d, f$  and  $f_2$  are the three voltage-dependent gates, and  $f_{cass}$  is the calcium-dependent one;  $G_{CaL}$  is the maximum conductance of the current;  $V$  is the transmembrane potential; and  $c_{ss}$  is the diadic subspace calcium concentration. The other terms are model parameters or physical constants.

As can be seen, the three cited models, Mahajan et al. [22], Ten Tusscher and Panfilov [23], and Stewart et al. [24], simulate the same phenomenon, and, disregarding the parameters and the values of the physical constants, they use the same equation to simulate the  $I_{CaL}$  current. Furthermore, it is possible to read the  $I_{CaL}$  equation of the three models as a multiplication of two terms:  $I_{CaL} = O \times I_{max}$ ; where  $O$  is the channels Opening fraction and the  $I_{max}$  is the maximum current value when all channels are open. In Mahajan et al. [22] model, this opening fraction term is represented by the Markovian state  $P_o$  and reaches peak levels around 10% of opening. On the other hand, in both Ten Tusscher and Panfilov [23], and Stewart et al. [24] models, this opening fraction is represented by the multiplication of the four gates  $d, f, f_2, f_{cass}$ , and reach the peak of around 90% in the opening levels. In the first moment, this difference in the amplitude of the opening fraction values can look weird. However, it is important to highlight the different natures that each model assumes. For instance, Mahajan et al. [22] focus on models for cardiac cells of rabbits, whereas Ten Tusscher and Panfilov [23], and Stewart et al. [24] propose models for cardiac cells of humans. Therefore, the difference observed in Fig 1, showing the dynamics of the opening fraction,  $O$ , and the L-type Calcium current,  $I_{CaL}$ , over the time for the models from Mahajan et al. [22], Ten Tusscher and Panfilov [23], and Stewart et al. [24], may be due to the differences between rabbits and humans.

As stated above, we consider two different approaches to model the opening fraction dynamics. Majahan et al. [22] uses a MC-based structure, while Ten Tusscher and Panfilov [23], and Stewart et al. [24] use a Gate-based formulation. However, as discussed by Mahajan et al. [22], the use of an MC-based approach naturally models the ion channel biophysical properties in terms of molecular transitions between discrete conformation states.

The first goal of this work is to propose and test a new MC-based  $I_{CaL}$  model that can replace the opening fraction,  $O$ , composed by the four gates  $d, f, f_2, f_{cass}$ , originally used in Ten Tusscher and Panfilov [23] (TP), and Stewart et al. [24] (ST) models.

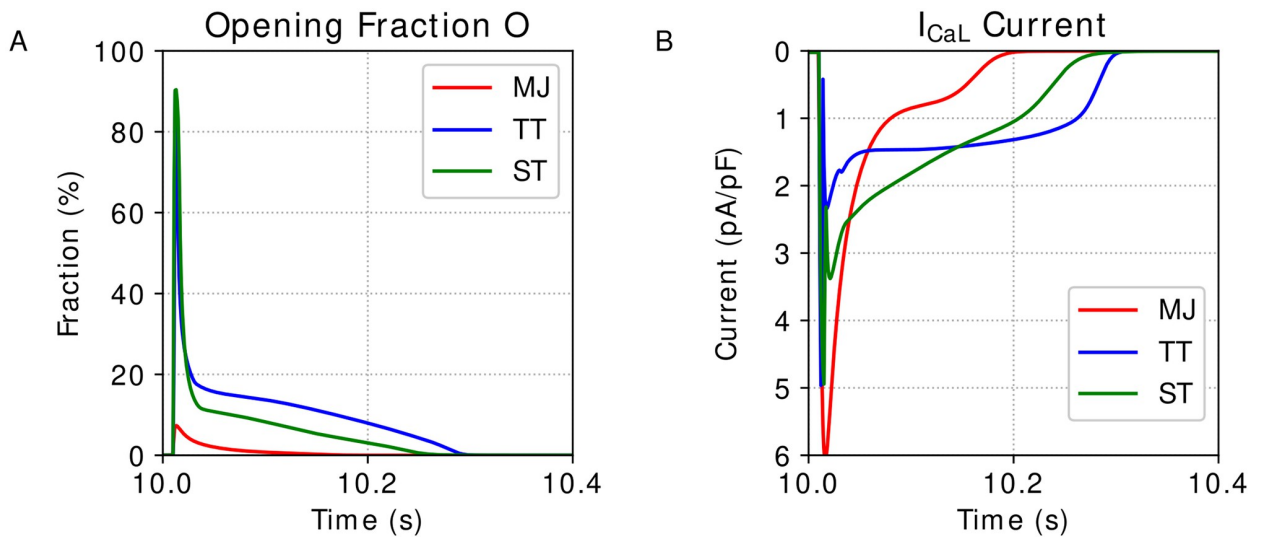


**Fig 1. Cardiac models outputs.** Output dynamics generated by the simulation of the models Mahajan et al. [22] (MJ), Ten Tusscher and Panfilov [23] (TP), and Stewart et al. [24] (ST). A: Opening Fraction, O. B: I<sub>CaL</sub> current.

<https://doi.org/10.1371/journal.pone.0266233.g001>

### Markov chain-based model

Considering that a single HH gate  $g$  can assume only two states (O—Open, and C—Close), we can generate a Markovian model for this gate, calculating the transition rates  $g_+$  (rate of the transition  $C \rightarrow O$ ) and  $g_-$  (rate of the transition  $O \rightarrow C$ ) as

$$g_+ = \frac{g_\infty}{\tau_g} \quad (3)$$

and

$$g_- = \frac{1 - g_\infty}{\tau_g}, \quad (4)$$

where  $g_\infty$  and  $\tau_g$  are equations defined by the HH Gate-based formalism [26].

Applying this analysis to the four gates of both TP, and ST models, it is possible to calculate all the rates that control the dynamics between the Open and Close states for each gate. Fig 2A illustrates these single MCs for each of the four gates and their respective transition rates. To propose a MC-based model for the cardiac models TP, and ST, we use these eight transition rates.

Once we defined the transition rates, we need to set the MC topology. Here, we adopt the minimal seven-state MC arrangement proposed by Mahajan et al. [22]. Fig 2B illustrates the original Mahajan et al. [22] MC for the I<sub>CaL</sub> formulation.

Thus, to transform the original gates from the Gate-based models into the MC-based formulation, we combine the rates of the HH formalism, Fig 2A, with the consolidated I<sub>CaL</sub> MC-based topology, Fig 2B. The result of this combination is the new proposed MC-based model presented in Fig 2C. In addition, to adjust this new MC-based model to the original human models, we introduce a set of eleven parameters that multiply some of the MC transition rates:  $x = \{x_i | x_i \in \mathbb{R} \text{ and } i = 0 - 10\}$ .

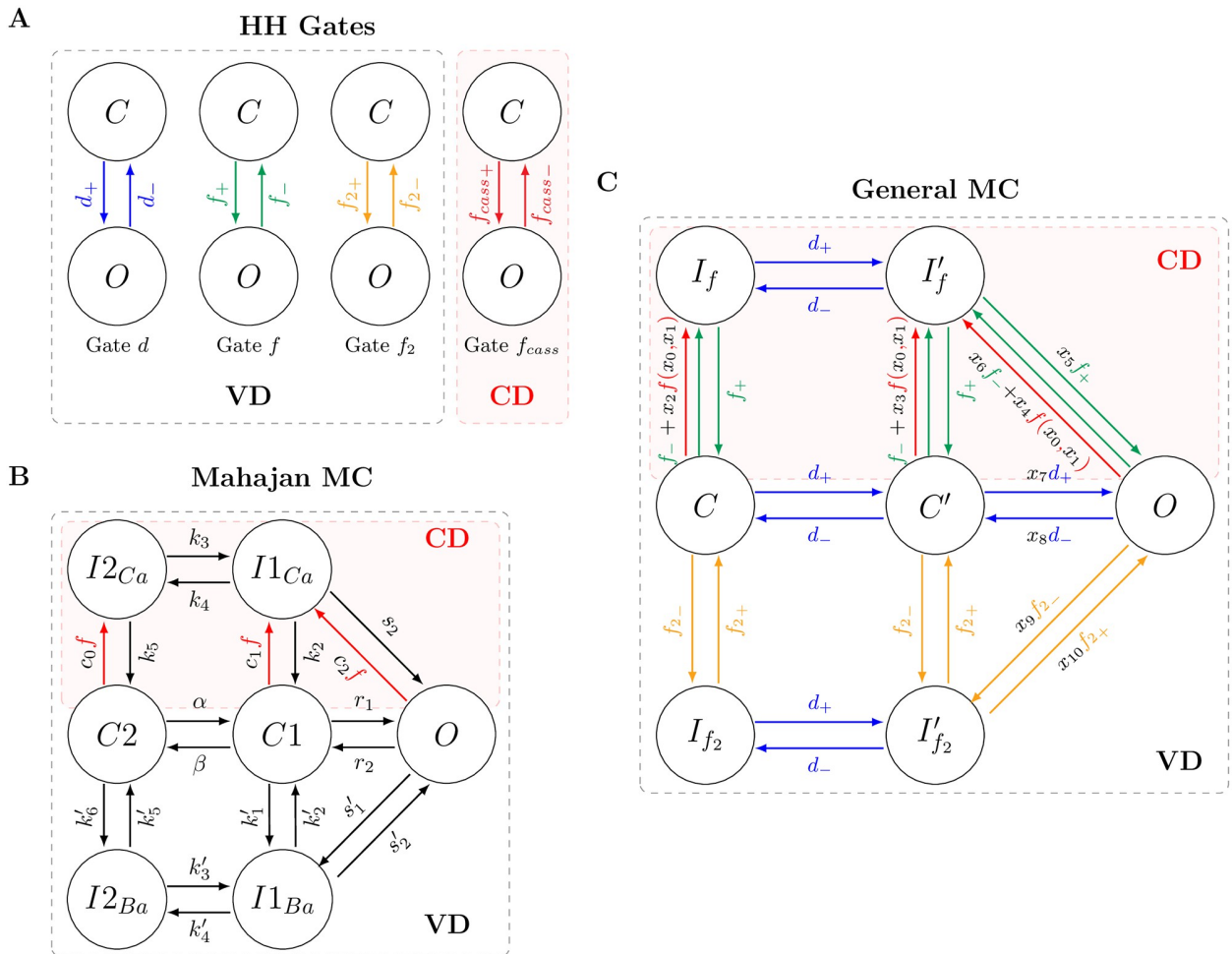


**Fig 2. Schematic representations of the three markov chain structures considered in this study.** A: The four independent Markov Chains for each gate of the models Ten Tusscher and Panfilov [23] or Stewart et al. [24] considering only two possible states, Open ( $O$ ) and Close ( $C$ ) for each one. B: The original structure of the Markov Chain used by Mahajan et al. [22] to simulate the  $I_{Cal}$  phenomenon. C: The proposed Markov Chain as a combination of the Hodgkin-Huxley formalism rates and the Mahajan et al. [22] topology, to replace the gates in the Ten Tusscher and Panfilov [23] and Stewart et al. [24] models. The MC transitions generated considering the HH gates  $d$ ,  $f$ , and  $f_2$  are shown respectively in blue, green, and yellow. The calcium-dependent function  $f$  and the rates associated with the calcium concentration are shown in red. The set of parameters  $x$  used to fit both calcium-dependent rates (parameters  $x_0$  to  $x_4$ ) and voltage-dependence rates (parameters  $x_5$  to  $x_{10}$ ) are shown in black.

<https://doi.org/10.1371/journal.pone.0266233.g002>

The first five fitting parameters,  $x_0$  up to  $x_4$ , are used to handle the MC calcium sensitivity. Considering the MC top layer, states  $I_f$  and  $I'_f$ , as the calcium-dependence layer, these five parameters are related to calcium-dependence. The first two parameters,  $x_0$  and  $x_1$ , compose the calcium-dependent equation

$$f(c, x_0, x_1) = \frac{1}{1 + (x_0 \bar{c}_p/c)^{x_1^3}}, \quad (5)$$

originally adapted from the MC proposed by Mahajan et al. [22]. The other three parameters,  $x_2$ ,  $x_3$ , and  $x_4$ , multiply, respectively, the calcium-dependent function  $f$  presented in the rates  $C \rightarrow I_f$ ,  $C' \rightarrow I'_f$ , and  $O \rightarrow I'_f$ .

On the other hand, the voltage-dependence appears in all MC states and rates. The top layer, states  $I_f$  and  $I'_f$ , and the fitting parameters  $x_5$  and  $x_6$  are associated with the voltage dependence behavior of the HH gate  $f$ ; the bottom layer, states  $I_{f2}$  and  $I'_{f2}$ , and the fitting parameters  $x_9$  and  $x_{10}$  are associated with the voltage dependence behavior of the HH gate  $f_2$ ; and the main layer, states  $C$ ,  $C'$ , and  $O$ , and the fitting parameters  $x_7$  and  $x_8$  are associated with the voltage dependence behavior of the HH gate  $d$ . Concerning the fitting process,  $x_5$  and  $x_6$  are used to fit the voltage dependence (top layer); the parameters  $x_9$  and  $x_{10}$  are used to fit the bottom layer, and  $x_7$  and  $x_8$  are used to fit the main layer. To see a more detailed description of the new MC model, please see [S1 Appendix](#).

## Fitting algorithm

In the above section, we propose a MC-based model to use in the  $I_{CaL}$  formulation for both Ten Tusscher and Panfilov [23], and Stewart et al. [24] models replacing the gate-based opening fraction equations. Next, it is necessary to adjust the MC fitting parameters set  $\mathbf{x}$  to reproduce the original outputs.

The fitting procedure has one primary objective: to find the eleven parameters  $x_i$  that make the Opening fraction of the new MC-based model able to reproduce the original Gate-based opening values. As we are only replacing the  $I_{CaL}$  opening fraction, once we recover its dynamics, we also recover the  $I_{CaL}$  current and, consequently, all the other model outputs, such as the AP and intracellular calcium.

As can be seen in [Eq \(2\)](#), for both models, TP, and ST, the multiplication  $df f_2 f_{cass}$  determines the opening fraction,  $O$ . The curves generated by the two respective models are shown in [Fig 1A](#).

The goal is to replace these opening fraction terms by our proposed MC-based open state and to find a parameter set  $\mathbf{x}$  capable to recover the original model outputs. So, we can see it as a minimization problem where we want to find the best set of parameters  $\mathbf{x}$  that minimizes the error between the new MC-based  $I_{CaL}$  curve and the original one. As a minimization problem, we have to chose the objective function, or fitness function,  $F$ . We defined as target as the  $I_{CaL}$  curve of the eleventh pulse (after a series of stimulated AP pulses). So, for the individual, or candidate set  $\mathbf{x}$ , the  $F$  function reads

$$F(\mathbf{x}) = \sqrt{\sum_{t=10s}^{11s} \frac{(I_{CaL_{MC}}(\mathbf{x}, t) - \overline{I_{CaL_{HH}}(t)})^2}{\overline{I_{CaL_{HH}}(t)}^2}}, \quad (6)$$

where  $\overline{I_{CaL_{HH}}}$  is the calcium current of the HH gate-based model and the  $I_{CaL_{MC}}$  is the calcium current generated by the new MC-based model using the parameter set  $\mathbf{x}$ . When we adjust the MC-based model to recover the TP model, our target is  $\overline{I_{CaL_{HH}}} = \overline{I_{CaL_{TP}}}$ . When adjusting to the ST model, our target is  $\overline{I_{CaL_{HH}}} = \overline{I_{CaL_{ST}}}$ . To obtain the  $I_{CaL}$  curves for the models, we simulated them using a pacing of 1Hz. We must point out, however, that we have checked the robustness of our approach to different pacing frequencies. Our best fits reproduce accurately the target data for different frequencies. These results can be found in the [S2 Appendix](#).

To solve this optimization problem, we used the Differential Evolution (DE) algorithm available in the Python library Pygmo [27]. In the DE field, each set of parameters  $\mathbf{x}$  is labeled as an individual or possible solution. Moreover, a set of individuals, or solutions, is labeled as population. The primary purpose of an evolutionary algorithm as DE is to begin from a random initial population and, generations over generations, to evolve this population

to find individuals, or solutions, that better solve the minimization problem. For more details about the DE algorithm, please see [28].

To execute the DE, we set the population size as 100 individuals, and, to generate the initial population used by the algorithm, we used the Latin Hypercube method available in Python library SMT [29]. We set the number of generations of the algorithm to 50. So, at the end of the DE execution, we will have  $50 \times 100$  possible solutions. The optimization algorithm is constrained by imposing limits for each one of the parameter. The search space  $S$  for the parameters was set as  $S = \{S \subset \mathbb{R}^{11} | 0.1 \leq s_i \leq 5.9\}$ , where  $s_i$  is the search space of the respective parameter  $x_i$ . All the other algorithm settings were adopted as the standard values implemented by the Pygmo library. To see more details about its settings, please see [27]. The cardiac models were implemented in C++. To simulate them, we used a multistep numerical method provided by C++ SUNDIALS CVODE library [30] setting the maximum time step as  $10^{-1}\text{ms}$ .

### Fitting robustness assessment

To analyze the fitting process of the new MC-based model, we considered a collection of the individuals found by the Differential Evolution algorithm, labeled as population of solutions. To compose this collection, or population,  $P$ , of the best solutions, we took into account how each solution contributes to the respective population. After sorting all the 5000 solutions from the best error  $F$  up to the worst, we could see that the relation between the individuals and their respective error could be seen as two different relations. The first one is rather a linear relation and, the second one is similar to an exponential relation. In this way, we concluded that the solutions in the exponential fraction should be discarded since the error they bring is higher than the possible quality it would aggregate.

Then, considering only the linear fraction of the ratio, we could select as many solutions as we could compute. At this point, we might also consider the computational cost. So, looking at the computational cost and driven by the acknowledgment of model discrepancy and the biological variability usually found in the experiments, 10 – 20%, from all 5000 possibilities obtained by the DE for each target model, we selected the best 300 solutions considering the fitness function error  $F$ , which was equivalent to including all solutions that satisfy  $F(\mathbf{x}) \leq 16\%$ , or 6% of the solutions (300/5000). [S1 Fig](#) in the Supporting Information presents the ratio between the sorted individuals and their respective errors  $F$ .

For each target model, TP and, ST, we generated the respective population  $P_{TP}$ , and  $P_{ST}$ . Furthermore, in the results, we highlight the best solution of the respective populations,  $P_{TP}$ , and  $P_{ST}$ , labeled as  $\mathbf{x}_{TP}^b$ , and  $\mathbf{x}_{ST}^b$ . It means the best solution which obtained the smallest error  $F(\mathbf{x}_b)$  for each respective model.

Besides the statistical analysis, we also assess the robustness of the fitting process by evaluating if the same population of solutions  $P$ , can reproduce the original model (target data) under a modified protocol. For that, we chose a protocol where the Calcium Inactivation is suppressed. This protocol simulates the condition of Calmodulin mutations associated with long QT syndrome which is known to promote proarrhythmic behavior in ventricular myocytes [31].

This protocol, Suppressed Calcium Inactivation (SCI), consists of removing the calcium sensitivity inside the Gate-based models and the MC-based models. To simulate this SCI protocol in the TP and in the ST original models, we set the gate  $f_{cass}$  equals 1. To simulate the SCI protocol in the MC-based formulation, we will set the calcium level  $c$  inside the function  $f = f(x_0, x_1, c)$ , [Eq \(5\)](#), as constant. [Fig 3](#) shows the opening fraction,  $O$ , and  $I_{CaL}$  curves for the models Mahajan et al. [22], Ten Tusscher and Panfilov [23], and Stewart et al. [24] under the SCI

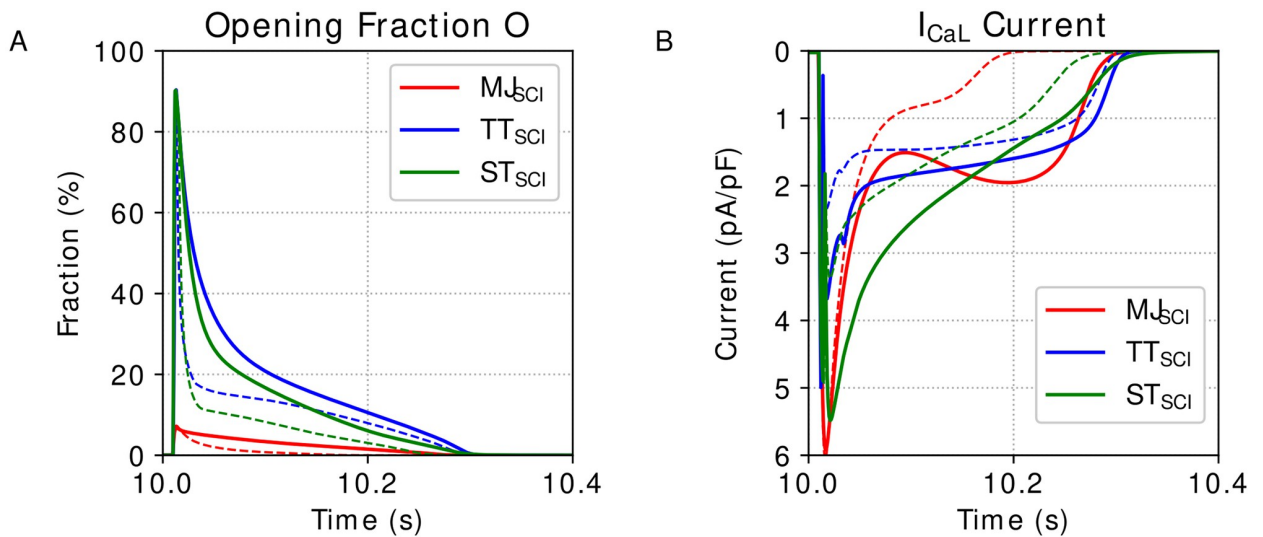


**Fig 3. Cardiac models outputs under SCI protocol.** Output dynamics of the models Mahajan et al. [22] (MJ), Ten Tusscher and Panfilov [23] (TP), and Stewart et al. [24] (ST) under Suppressed Calcium Inactivation (SCI) protocol. The dashed lines represent the same variables but in full protocol. A: Opening Fraction, O. B: I<sub>CaL</sub> current.

<https://doi.org/10.1371/journal.pone.0266233.g003>

protocol. Considering the protocol SCI, we evaluate how the population of models  $P_*$ , which was fitted using a different protocol (Full), can reproduce the experiments  $TP|_{SCI}$ , and  $ST|_{SCI}$ .

Although we only use the fitness function  $F(\mathbf{x})$  to select the parameters of the models, we also evaluate the solutions using some important biomarkers for the AP and the Intracellular Calcium concentration ( $[Ca]$ ). For the AP, we consider the features: duration from the AP peak up to 50% of decay,  $APD_{50}$ , and the duration from the AP peak up to 90% of decay,  $APD_{90}$ . For the  $[Ca]$  curve, the features are the Calcium basal level  $[Ca]_{i\min}$ , and the Calcium Peak value,  $[Ca]_{iPeak}$ .

### Multi-protocol analysis

We also evaluate the benefits from selecting a new population of 300 solutions, from the same original 5000 candidates, that takes into account both the original fitness function  $F(\mathbf{x})$  as well as a similar error function for the SCI protocol. The idea behind this exercise is to evaluate how the re-sampling of a new population of solutions can accommodate new experimental evidence.

Although we did not use a multi-objective function in any case of the DE executions, we also evaluated the capacity of all the 5000 solutions described in Section Fitting algorithm to reproduce the respective original models, TP, and ST, simulated under the SCI protocol. For each solution  $\mathbf{x}$ , now, we have two errors associated with it: the Full protocol error,  $F(\mathbf{x})|_N$ , and the SCI protocol error,  $F(\mathbf{x})|_{SCI}$ . Both,  $F(\mathbf{x})|_N$ , and  $F(\mathbf{x})|_{SCI}$  reflects the same mathematical equations presented in Eq (6), but each one considers the models simulated under the Full, and under the SCI protocols, respectively. At this moment, we can define a new population  $PO_*$ , which is composed of the best Overall solutions evaluated considering the function  $OF(\mathbf{x})$ :

$$OF(\mathbf{x}) = \sqrt{F^2(\mathbf{x})|_N + F^2(\mathbf{x})|_{SCI}}. \quad (7)$$

This new populations  $PO_{TP}$ , and  $PO_{ST}$ , obtained for the models TP, and ST, bring their respective new best solutions  $\mathbf{x}_{TP}^o$  and  $\mathbf{x}_{ST}^o$ .

In summary, we will use a color scheme to represent the main findings in Results section. The black markers presents the original TP, and ST models; the blue markers present the selected MC-based solutions which compose the population of solutions found for the TP model,  $P_{TP}$ ; the best solution of the population  $P_{TP}$ ,  $x_{TP}^b$ , is highlighted using the dark blues color; the red markers present the selected MC-based solutions which compose the population of solutions found for the ST model,  $P_{ST}$ ; the best solution of the population  $P_{ST}$ ,  $x_{ST}^b$ , is highlighted using the dark red color; the orange markers present the selected MC-based solutions which compose the population of the best overall solutions found for the TP model,  $PO_{TP}$ ; the best solution of the population  $PO_{TP}$ ,  $x_{TP}^o$ , is highlighted using the dark orange color; the green markers present the selected MC-based solutions which compose the population of the best overall solutions found for the ST model,  $PO_{ST}$ ; the best solution of the population  $PO_{ST}$ ,  $x_{ST}^o$ , is highlighted using the dark green color. The same scheme of colors are used to show the results for both, Full, and SCI protocols. Finally, the notation  $\bullet|_{SCI}$  represents the simulation under the SCI protocol.

## Statistical and sensitivity analysis

The fitting process involves a set of parameters and objective targets. However, as soon as the size of the parameter set increases, it becomes more complicated to understand the correlation between each parameter and the target outputs. Sensitivity Analysis is a tool that improves this understanding. This process consists of checking how each parameter influences the outputs.

In this study, we perform a Sensitivity Analysis based on variances to understand how each one of the 11 parameters ( $x_0$  up to  $x_{10}$ ) influences the fitness error  $F(\mathbf{x})$ . For that, we calculate the 1<sup>st</sup>-order, and the Total-order Sobol Sensitivity Index. The 1<sup>st</sup>-order sensitivity index quantifies only the portion that an input parameter contributes directly to the total variance of the quantity of interest. The Total-order index also considers the sensitivity generated by the interaction between the parameters. For more details see [32]. To calculate these sensitivity indexes, we used the Python library ChaosPy [33].

## Results

### Successful fitting of the new markov chain-based under full protocol—Training

We proceed to show how the MC-framework explained in Section Markov chain-based model can properly fit the output of the two models selected as guiding examples in our study: Ten Tusscher and Panfilov [23] (TP model), and Stewart et al. [24] (ST model).

We perform a single execution of the DE algorithm (see Section Fitting algorithm) for each of the two target models. We plot in Figs 4 and 5 the original traces for the Opening fraction of the LCC, the  $I_{CaL}$  current, the AP and the Calcium transient  $[Ca]$ , for the TP and the ST model respectively. In each panel, the original output (black line) is plotted together with the results of the population selection of the algorithm together with the best global fit of this population (blue lines for the TP model, and red lines for the ST model). The parameter values obtained from the optimization correctly reproduce the action potentials under normal (1 Hz) and faster pacings. See [S2 Appendix](#).

The selection of the population made by the DE execution is very good for both TP, and ST cases. The key is not that there is a particular solution that fits almost perfectly the outcome, but that the population spans remarkably the general surroundings of the model-space. We can see in [Table 1](#) a comparison of the key properties of the AP and  $[Ca]$ , for each original model with the average and standard deviation values obtained from the selected populations

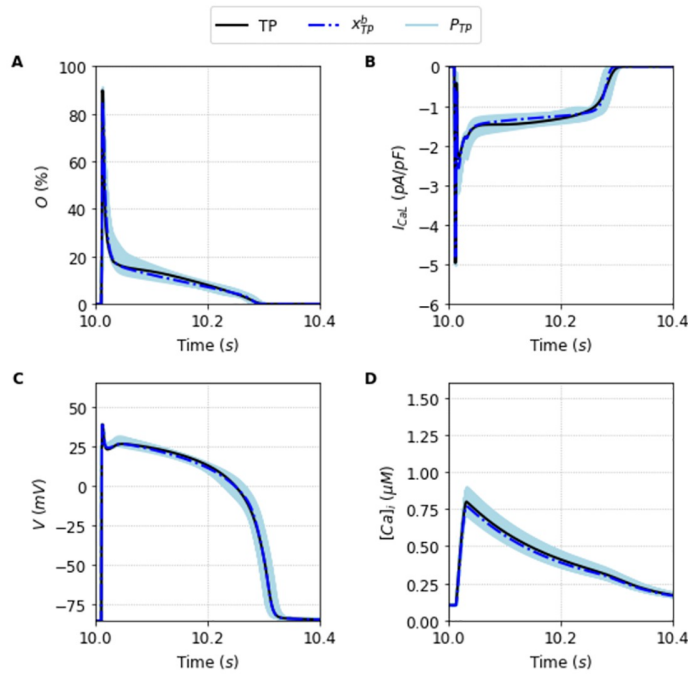


**Fig 4. Outputs generated by the population of solutions  $P_{TP}$  simulated under the Full protocol.** Traces obtained using the best solution of the population  $P_{TP}$ ,  $x_{TP}^b$  (dashed blue line), alongside the traces obtained using the other solutions that compose the population (light blue lines) compared with the original Ten Tusscher and Panfilov [23] model (black line) simulated under the Full protocol. A: Opening fraction,  $O$ . B:  $I_{CaL}$  current. C: Action Potential. D: Intracellular Calcium concentration,  $[Ca]_i$ .

<https://doi.org/10.1371/journal.pone.0266233.g004>

$P_{\bullet}$ . These populations of solutions  $P_{\bullet}$  found under the Full protocol are perfectly fit with typical errors around 0–1% except for the error in the peak of calcium of the ST model where it reaches values close to 4%.

Another important fact is that the values achieved by the objective fitness function to minimize Eq (6) are not close to zero. The best parameter fit for each model was  $F(x_{TP}^b) = 9\%$  and  $F(x_{ST}^b) = 13\%$  for the TP and ST model, respectively. This indicates that the best parameters cannot exactly reproduce the Full  $I_{CaL}$  current. This is a typical case of model discrepancy, as described before in [34]. In this case, a good practice is to accept solutions with a higher tolerance for the fitness value. In this direction, the average value of the objective function of the  $I_{CaL}$  current obtained by the solutions that compose the population  $P_{TP}$  is around  $F = 13\% \pm 1$ , and  $F = 15\% \pm 1$  for the solutions that compose the population  $P_{ST}$ . It is the whole population that is capable of providing a good ensemble. They are good enough to be in the population as they reasonably fit the model outcome and, as we will see, give us the flexibility to fit intercellular or intermodel differences in the outcome. We proceed to show its usefulness discussing first the limitation of taking only the best fit,  $x_{\bullet}^b$ .

### Limitation of the best fit in a protocol with suppression of the calcium inactivation in the LCC

We proceed now to implement a protocol where we suppress all calcium dependence in the LCCs. Now, the two models produce not only different  $I_{CaL}$  currents but also slightly different APD and very different calcium transient given the well-known effects of calcium transient in

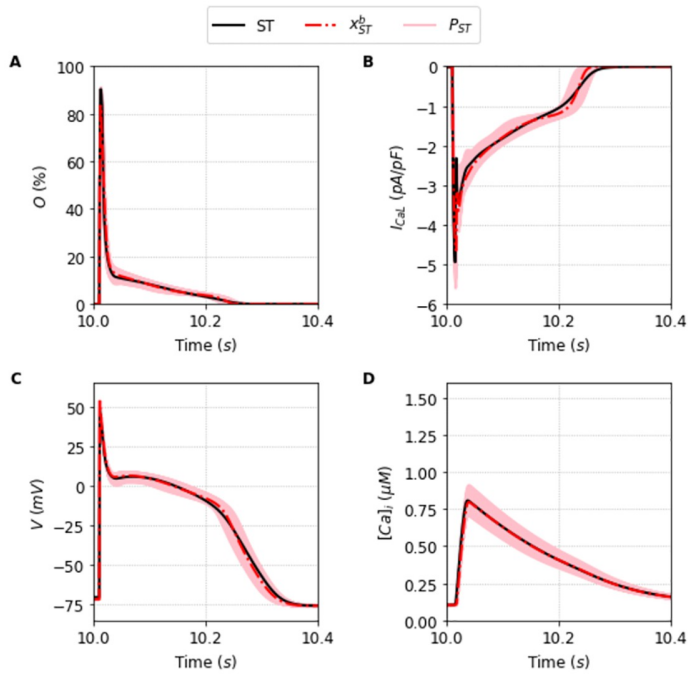


**Fig 5. Outputs generated by the population of solutions  $P_{ST}$  simulated under the Full protocol.** Traces obtained using the best solution of the population  $P_{ST}$ ,  $x_{ST}^b$  (dashed red line), alongside the traces obtained using the other solutions of the population (light red lines) compared with the original Stewart et al. [24] model (black line) simulated under the Full protocol. A: Opening fraction,  $O$ . B:  $I_{CaL}$  current. C: Action Potential. D: Intracellular Calcium concentration,  $[Ca]_i$ .

<https://doi.org/10.1371/journal.pone.0266233.g005>

the inactivation of the  $I_{CaL}$  current. More specifically, the output gives larger currents and larger calcium transients with the new protocol. The aim of this suppression of the calcium inactivation (SCI protocol) is to mimic the results of an pathological condition associated with proarrhythmic behavior. There were many options available but we think that a short-circuit

**Table 1. Features for the AP and  $[Ca]_i$  traces obtained by the simulations under Full protocol.**

Features	Full Protocol			ST Model		
	$P_{TP}$	TP	MAPE <sup>a</sup>	$P_{ST}$	ST	MAPE <sup>a</sup>
$APD_{50}^b$	$275.2 \pm 4.9$	273	1.62%	$197.6 \pm 9.3$	195	4.03%
$APD_{90}^b$	$301.8 \pm 4.8$	301	1.33%	$286.5 \pm 7.0$	292	2.53%
$[Ca]_{iMin}^c$	$0.1 \pm 0.001$	0.1	1.04%	$0.1 \pm 0.002$	0.1	1.86%
$[Ca]_{iPeak}^c$	$0.8 \pm 0.04$	0.81	4.02%	$0.79 \pm 0.04$	0.81	5.09%

Values of the features for the Action Potential (AP) and Intracellular Calcium concentration ( $[Ca]_i$ ) for the respective populations of solutions  $P_{TP}$  found for the TP model [23], and  $P_{ST}$  found for the ST model [24] in comparison with respective original models values simulated under Full protocol.

<sup>a</sup>The errors are expressed as the Mean Absolute Percentage Error (MAPE) of the population. It can be computed as  $MAPE = \frac{100}{n} \sum^x |Feature_x - Feature_m| / Feature_m$ , where  $Feature_x$  is the value of the feature obtained using the solution  $x$ , and  $Feature_m$  is the value of the same feature obtained simulating the respective original model  $m$ . The summation is calculated over all the  $n$  solutions that compose the population  $P$ .

<sup>b</sup>Values are expressed in ms.

<sup>c</sup>Values are expressed in  $\mu M$ .

<https://doi.org/10.1371/journal.pone.0266233.t001>

**Table 2.** Features for the AP and  $[Ca]$ , traces obtained by the simulations under the SCI protocol.

Features	SCI Protocol			ST Model		
	$P_{TP SCI}$	$TP SCI$	MAPE <sup>a</sup>	$P_{ST SCI}$	$ST SCI$	MAPE <sup>a</sup>
$APD_{50}^b$	$279.9 \pm 5.4$	282	1.62%	$221.4 \pm 29.1$	248	13.56%
$APD_{90}^b$	$306.6 \pm 5.3$	311	1.78%	$308.8 \pm 28.3$	343	11.52%
$[Ca]_{iMin}^c$	$0.11 \pm 0.002$	0.11	5.47%	$0.11 \pm 0.006$	0.12	9.74%
$[Ca]_{iPeak}^c$	$0.86 \pm 0.05$	1.08	20.05%	$1.0 \pm 0.28$	1.45	33.81%

Values of the features for the Action Potential (AP) and Intracellular Calcium concentration ( $[Ca]$ ) for the respective populations of solutions  $P_{TP}$  found for the TP model [23], and  $P_{ST}$  found for the ST model [24] in comparison with respective original models values simulated under SCI protocol.

<sup>a</sup>The errors are expressed as the Mean Absolute Percentage Error (MAPE) of the population. It can be computed as  $MAPE = \frac{100}{n} \sum^x |Feature_x - Feature_m| / Feature_m$ , where  $Feature_x$  is the value of the feature obtained using the solution  $x$ , and  $Feature_m$  is the value of the same feature obtained simulating the respective original model  $m$ . The summation is calculated over all the  $n$  solutions that compose the population  $P$ .

<sup>b</sup>Values are expressed in ms.

<sup>c</sup>Values are expressed in  $\mu M$ .

<https://doi.org/10.1371/journal.pone.0266233.t002>

of the calcium inactivation of the LCC is a perfect computational example of a pseudo-experiment.

We can now compare how the average population behaves with the new protocol. We check how our former best parameter fit solution, that we call  $x_{TP}^b$  for the TP model and  $x_{ST}^b$  for the ST model, fits the outcome of the new APD and calcium transients under the new protocol that suppresses calcium inactivation of the LCC. Table 2 shows the performance of the average of the population for respective models for the same benchmarks used in the Full protocol. We can see how the average errors are larger. This makes perfect sense, since the population  $P$  was obtained using a different protocol (Full protocol). However, it is quite impressive that these errors are not very large for APD and the minimum calcium level. The most relevant differences appear in the calcium peak, where typical 20–30% errors are present. The reason is clear: differences in the  $I_{CaL}$  current do not affect the APD if they are not rather large, given the presence of other currents that do not provide a significant feedback into the voltage-dependence nature of the LCC. On the other hand, there is a strong feedback between the transient of calcium and the inactivation of the LCC, precisely because of the Calcium-Induced Calcium-Release nature of the calcium release trigger.

In the SCI case, the population of solutions  $P_{TP|SCI}$  gave an error of roughly  $21\% \pm 3$ , while the population of solutions  $P_{ST|SCI}$  obtained an error of  $29\% \pm 7$  when compared with the respective original  $TP|SCI$ , and  $ST|SCI$  under the same conditions. So we can easily see that the errors are more prominent for the SCI protocol when compared to the control or full protocol. We must emphasize again that we are not finding a new population to fit the new protocol data. We are just testing how the population we found in the previous section behaves when the inactivation dependence of the LCC is suppressed.

In this sense, Figs 6 and 7 are particularly relevant. They show, respectively, the new traces of the outputs generated using the population of solutions  $P_{TP|SCI}$  compared to the model  $TP|SCI$ , and the new traces of the outputs generated using the population  $P_{ST|SCI}$  compared with the model  $ST|SCI$ . The blue dashed lines, and the red dashed lines highlight how the best solutions,  $x_{TP|SCI}^b$ , and  $x_{ST|SCI}^b$  are clearly not the best solutions of each respective populations now.

We can observe in Figs 6 and 7 the relevance of having a broad population that can encompass different experimental data or different protocol data. The population in the new protocol

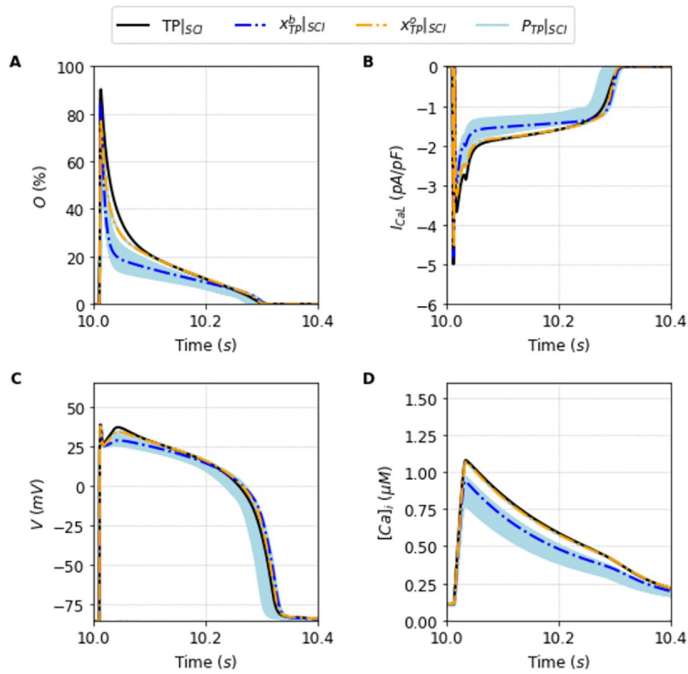


**Fig 6. Outputs generated by the population of solutions  $P_{TP}$  simulated under the SCI protocol.** Traces of the best solution of the population  $P_{TP}$  simulated under SCI protocol,  $x_{TP}^b$  (dashed blue line), and the best overall solution  $x_{TP}^o$  (dashed orange line) simulated under SCI protocol, alongside the traces generated by the simulation of the population of solutions  $P_{TP}|SCI$  (light blue lines) compared with the original Ten Tusscher and Panfilov [23] model (black line) under the SCI protocol. A: Opening fraction,  $O$ . B:  $I_{CaL}$  current. C: Action Potential. D: Intracellular Calcium concentration,  $[Ca]_i$ .

<https://doi.org/10.1371/journal.pone.0266233.g006>

generally shifts on average away from the new outcome, but it is broad enough, as we will see now, to be able to find a new best fit solution that encompasses the new input data.

### Robustness of the population of solutions—generalization

We proceed to analyze whether the original populations  $P_\bullet$  were flexible enough to find a set of parameters that can properly fit both the initial data and the new data obtained with the SCI protocol. In the previous section we have shown how the best solutions for the models outcome are not the most robust solutions under the addition of data from a new protocol. To select the best overall solution for each target model, we considered the overall fit  $OF(\mathbf{x})$  as described in Eq (7).

We calculate this overall fit for all the solutions that were already present in the population selected in Section Successful fitting of the new markov chain-based under full protocol—training. This is an important point. We do not need to go back and re-obtain a population around this new minimization with a new objective function. If the population is robust and broad enough, analyzing it should provide a reasonably good solution with a small overall error. This is indeed the case. The new best solutions,  $x_{TP}^o$ , and  $x_{ST}^o$ , are plotted respectively as a orange dashed line in Fig 6, and as a green dashed line in Fig 7. It is remarkably good.

Fig 8 shows the idea behind this selection. We do a scatter plot where each solution in the population is placed with its two fitness functions, one for the normal output (X-Axis) and one for the SCI protocol (Y-Axis). We can see the cloud of points indicating how the population properly spans reasonable errors. However, the best fit of the full protocol (blue dot for the TP

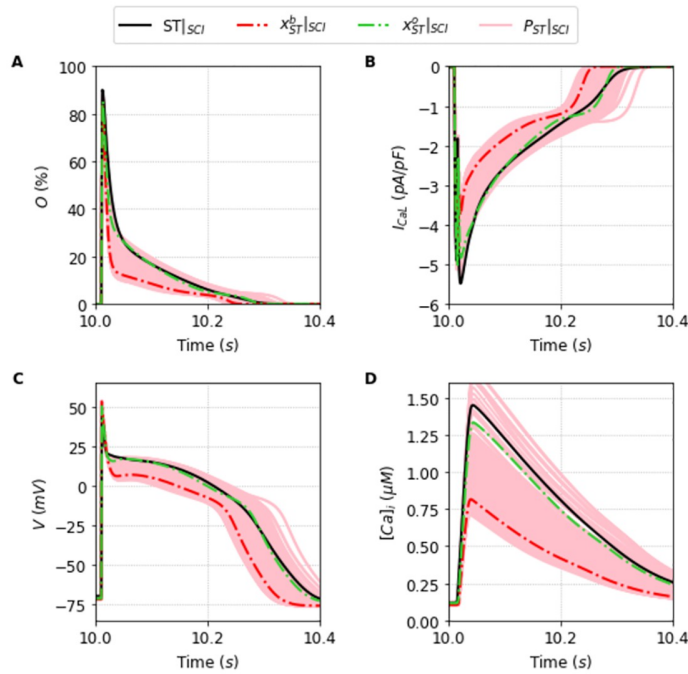


**Fig 7. Outputs generated by the population of solutions  $P_{ST}$  simulated under the SCI protocol.** Traces of the best solution of the population  $P_{ST}$  simulated under SCI protocol,  $x_{ST}^b$  (dashed red line), and the best overall solution  $x_{ST}^o$  (dashed green line) simulated under SCI protocol found for the [24] model, alongside the traces generated by the simulation of the population of solutions  $P_{ST|SCI}$  (light red lines) compared with the original Stewart et al. [24] model (black line) under the SCI protocol. A: Opening fraction,  $O$ . B:  $I_{CaL}$  current. C: Action Potential. D: Intracellular Calcium concentration,  $[Ca]_i$ .

<https://doi.org/10.1371/journal.pone.0266233.g007>

Model, and red dot for the ST Model) are not the best overall fit (orange dot for the TP Model, and green dot for the ST Model). For example, in the TP model the best overall fit has a value of  $OF(x_{TP}^o) = 18\%$  with  $F(x_{TP}^o)|_N$  around 15% and  $F(x_{TP}^o)|_{SCI}$  around 10%. This is a clear improvement from the best solution when the new protocol was not taken into consideration.

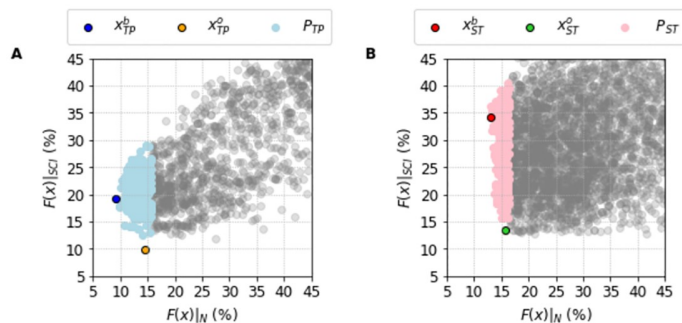


**Fig 8. Correlation between the Full and SCI protocols errors of the population  $P$ .** Values of the Full protocol and SCI protocols errors, respectively  $F(x)|_N$  and  $F(x)|_{SCI}$ . A: The best Full protocol solution,  $x_{TP}^b$  (blue dot), the best Overall solution  $x_{TP}^o$  (orange dot) alongside all the solutions that compose the population  $P_{TP}$  (light blue dots) found for the Ten Tusscher and Panfilov [23] model. B: The best Full protocol solution,  $x_{ST}^b$  (red dot), the best Overall solution  $x_{ST}^o$  (green dot) alongside all the solutions that compose the population  $P_{ST}$  (light red dots) found for the Stewart et al. [24] model. The other representations (gray dots) are the solutions that became out of the respective population  $P$ .

<https://doi.org/10.1371/journal.pone.0266233.g008>

The  $\mathbf{x}_{TP}^b$  solution has  $F(\mathbf{x}_{TP}^b)|_N$  at 9% as indicated previously, but with the new protocol  $F(\mathbf{x}_{TP}^b)|_{SCI}$  is around 20%.

Remarkably, we observe exactly the same structure for the population obtained for the ST data/model. We again find that the population is very robust and can produce an overall best fit without the need of retraining. In this model, the penalty we encounter in order to move from the original model output to the inclusion of the new protocol is way smaller than in the TP model but we cannot achieve the same very low values of  $F(\mathbf{x})|_{SCI}$ .

The clouds presented in Fig 8 also show that the selected populations of solutions  $P_\bullet$  have a narrow range for  $F(\mathbf{x})|_N$ , but spans a wider range for  $F(\mathbf{x})|_{SCI}$ . This clearly reflects that the individuals of the populations  $P_\bullet$  were selected to account only for the smallest values of  $F(\mathbf{x})|_N$ .

The characteristics of the population can be better understood in Fig 9 where we highlight the different properties of the clouds in terms of the errors in AP and  $[Ca]_i$  features for both models. Once again, the clouds occupy more space in the upper side of the SCI protocol since the objective function was to minimize the distance to the  $I_{CaL}$  current between the model output and our MC-based model. Nevertheless, we see that our population is flexible and robust enough to find a subset of solutions that clearly manage to provide good values for the benchmarks. Indeed, the best overall fits provide rather low errors for  $I_{CaL}$ , AP and  $[Ca]_i$ . In addition, once we have the populations selected, we might focus on the  $I_{CaL}$  current to obtain the best overall fit as we have done until now and shown in Figs 6–9, or we can focus on any other particular feature that we might find more important or relevant, whether it is  $I_{CaL}$ , AP or  $[Ca]_i$  related.

### Learning from new data—Sensitivity analysis, identifiability, and multi-objective function

So far we have performed the traditional steps of machine learning: 1) training a population of solutions; and 2) testing how it generalizes to new data (SCI protocol). Fig 10 shows the case where we assimilate the new data to create a new populations of solutions  $PO_\bullet$ , that comprises the 300 solutions with smallest overall fitness, see Eq (7). A Pareto front [35] can be easily spotted highlighting the compromise between the two different datasets. Figs 11 and 12 show how these new populations evaluated under the SCI protocol,  $PO_{TP}|_{SCI}$ , and  $PO_{ST}|_{SCI}$ , can better reproduce the two different data for the  $TP|_{SCI}$  and  $ST|_{SCI}$  cases, respectively.

Fig 13 presents the parameter ranges of the two populations of solutions  $P_\bullet$  and  $PO_\bullet$  for the TP and ST cases. Some parameters have wide ranges of values, or high variances, such as  $x_2$ ,  $x_3$ , and  $x_7$ . Others have small variances, such as  $x_6$ , and  $x_8$ . Furthermore, Fig 14 presents a Sensitivity Analysis done to check how each parameter influences the error function  $F(\mathbf{x})$ . In this case, we can see how the parameter  $x_8$ , besides having a small variance, also produces a high sensitivity in the MC-based model. So, these variances combined with the sensitivity analysis, can clarify how each parameter is associated with the fitting process. High variances combined with small sensitivity indices may indicate the parameters that have low influence on  $I_{CaL}$ , whereas small variances combined with high sensitivity indices may highlight the most important parameters that affect the  $I_{CaL}$  dynamics.

When we move from the control populations,  $P_{TP}$  (blue bars), and  $P_{ST}$  (orange bars), to the overall populations,  $PO_{TP}$  (red bars), and  $PO_{ST}$  (green bars), we can observe what we have learned with the assimilation of new data. For instance, for parameter  $x_8$  the new data shifted its mean value and reduced its variance. In this case, the new data filtered or rejected some solutions that belonged to  $P_\bullet$ . However, the new data also expanded the original population  $P_\bullet$  with new solutions. This is the case for instance, for parameters  $x_6$  and  $x_9$ . For these, the new

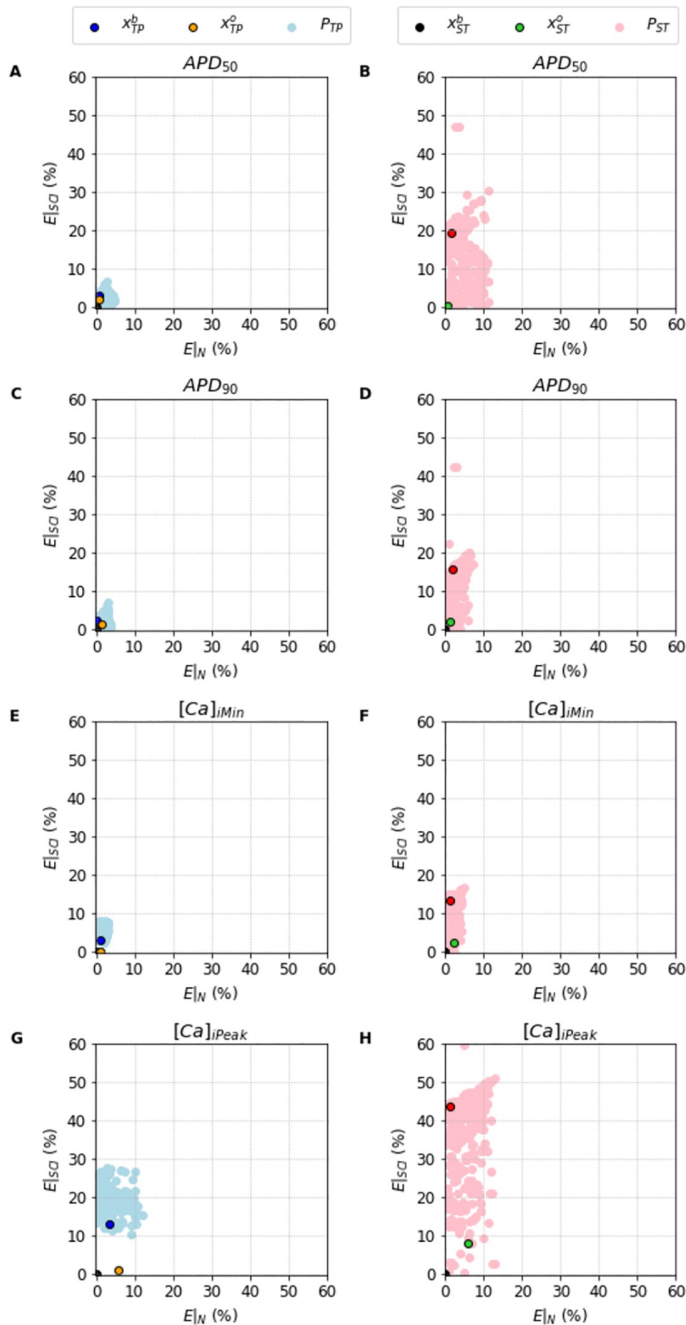


**Fig 9. Errors of the features of the AP and [Ca], traces obtained by the population of solutions  $P_*$ .** The left column shows the population of feasible solutions  $P_{TP}$  (light blue dots) found for the Ten Tusscher and Panfilov [23], and highlights the best solution  $x_{TP}^b$  (blue dot) alongside the best Overall solution  $x_{TP}^o$  (orange dots) found for the same model. The right column shows the population of feasible solutions  $P_{ST}$  (gray dots) found for the Stewart et al. [24], and highlights the best solution  $x_{ST}^b$  (red dot) alongside the best Overall solution  $x_{ST}^o$  (green dots) found for the same model. A: TP Model APD<sub>50</sub>. B: ST Model APD<sub>50</sub>. C: TP Model APD<sub>90</sub>. D: ST Model APD<sub>90</sub>. E: TP Model [Ca]<sub>iMin</sub>. F: ST Model [Ca]<sub>iMin</sub>. G: TP Model [Ca]<sub>iPeak</sub>. H: ST Model [Ca]<sub>iPeak</sub>. The errors were calculated using  $E_*(x) = |\text{Feature}_x - \text{Feature}_{m*}| / \text{Feature}_{m*}$ , where Feature<sub>x</sub> is the value of the respective features obtained simulating the solution  $x$ , and Feature<sub>m\*</sub> is the value of the respective features obtained simulating the original models (or target models).

<https://doi.org/10.1371/journal.pone.0266233.g009>

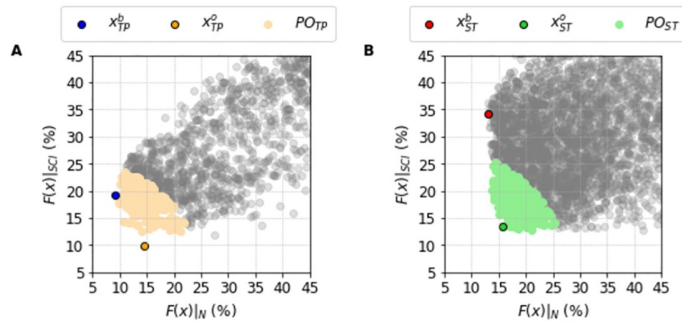


**Fig 10. Correlation between the Full and SCI protocols errors of the population of solutions  $PO_{\cdot}$ .** Values of the Full and SCI protocols errors, respectively  $F(x)|_N$  and  $F(x)|_{SCI}$ . A: The best Full protocol solution  $x_{TP}^b$  (blue dot), the best Overall solution  $x_{TP}^o$  (orange dot) alongside all the solutions that compose the population  $PO_{TP}$  (light orange dots) selected for the Ten Tusscher and Panfilov [23] model. B: The best Full protocol solution  $x_{ST}^b$  (red dot), the best Overall solution  $x_{ST}^o$  (green dot) alongside all the solutions that compose the population  $PO_{ST}$  (light green dots) selected for the Stewart et al. [24] model. The other representations (gray dots) are the solutions that became out of the respective populations  $PO_{\cdot}$ .

<https://doi.org/10.1371/journal.pone.0266233.g010>

data shifted their mean values but rather increased their variances, i.e., wider parameter ranges were needed to accommodate the two different datasets.

Therefore, there is no question we are really learning and improving our solutions by assimilating the new dataset from the SCI protocol. Unfortunately, some parameters have not

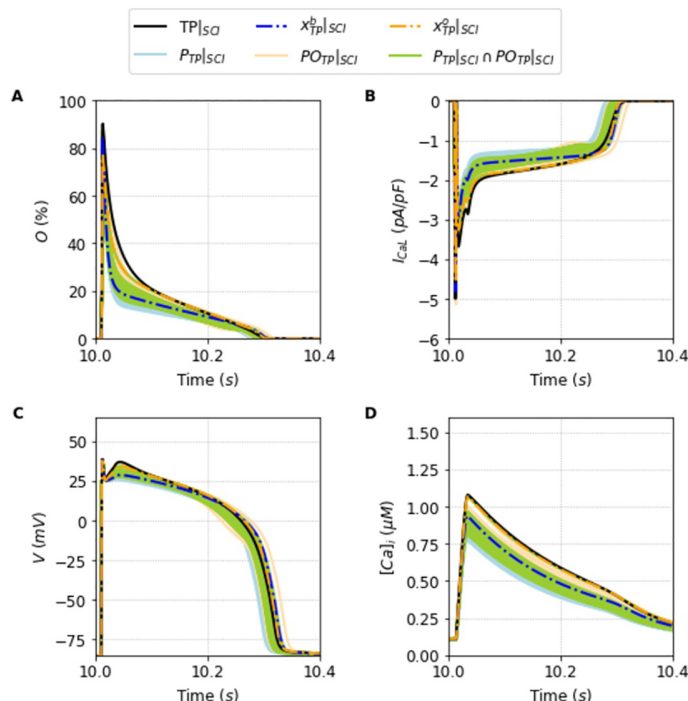


**Fig 11. Traces of the populations of fitting solutions  $P_{TP}$  and  $PO_{TP}$  under SCI protocol.** The light blue lines are the 300 best solutions considering the objective function  $F$  which compose the population  $P_{TP}$ . The light orange lines are the 300 best solutions considering the overall fit  $OF$  which compose the population  $PO_{TP}$ . Naturally, the solutions that are present in both populations are shown as light green lines. Furthermore, the two dashed lines, the blue and the orange one, represent the best solution  $x_{TP}^b$  and the solution  $x_{TP}^o$  respectively. The black line represents the Ten Tusscher and Panfilov [23] model. A: Opening fraction,  $O$ . B:  $I_{CaL}$  current. C: Action Potential. D: Intracellular Calcium concentration  $[Ca]_i$ .

<https://doi.org/10.1371/journal.pone.0266233.g011>

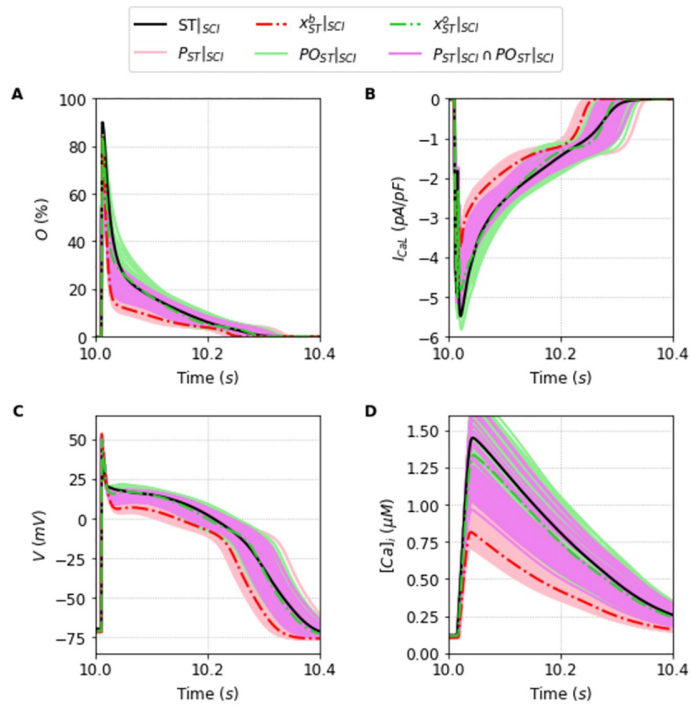


**Fig 12. Traces of the populations of fitting solutions  $P_{ST}$  and  $PO_{ST}$  under SCI protocol.** The light red lines are the 300 best solutions considering the objective function  $F$  which compose the population  $P_{ST}$ . The light green lines are the 300 best solutions considering the overall fit  $OF$  which compose the population  $PO_{ST}$ . Naturally, the solutions that are present in both populations are shown as purple lines. Furthermore, the two dashed lines, the red and the green one, represent the best solution  $x_{ST}^b$  and the solution  $x_{ST}^o$  respectively. The black line represents the Stewart et al. [24] model. A: Opening fraction, O. B:  $I_{CaL}$  current. C: Action Potential. D: Intracellular Calcium concentration  $[Ca]_i$ .

<https://doi.org/10.1371/journal.pone.0266233.g012>

changed when moving from  $P_{\cdot}$  to the  $PO_{\cdot}$  populations. See, for instance, the cases of parameters  $x_2$  and  $x_3$ . Together with the fact they have very large variances, these parameters are likely to be unidentifiable. At least, if we use only the  $I_{CaL}$  curve as data. However, it is worth noting from Figs 11 and 12 that the propagation of the uncertainties in the parameters [36] have a high impact on the waveforms of  $[Ca]_i$ . Since both  $x_2$  and  $x_3$  are related to calcium-dependent inactivation, it is worth including both  $I_{CaL}$  and  $[Ca]_i$  in a future work that uses multi-objective optimization tools, such as those described in [35, 37].

## Discussion

We have employed DE algorithms to replace the HH Gate-based description of the channels of two electrophysiology models of human cardiac cells Ten Tusscher and Panfilov [23], and Stewart et al. [24], by a new MC-based model. We selected the new parameters to mimic the dynamics of the original cardiac models, giving rise to two new models that fit the original AP and calcium concentrations, among other model characteristics. We show the importance of using the best fitting and an ensemble of a set of parameter values to reproduce a different scenario that considers the suppression of the calcium inactivation.

The presence of MC structures in the cardiac models brings several possibilities of studies capable of generating simulations over different scales, from subcellular up to tissue scale. This possibility allows computational models to help investigate pathologies that have their cause in the subcellular scale but can affect whole-cell and AP propagation. The use of MC-based

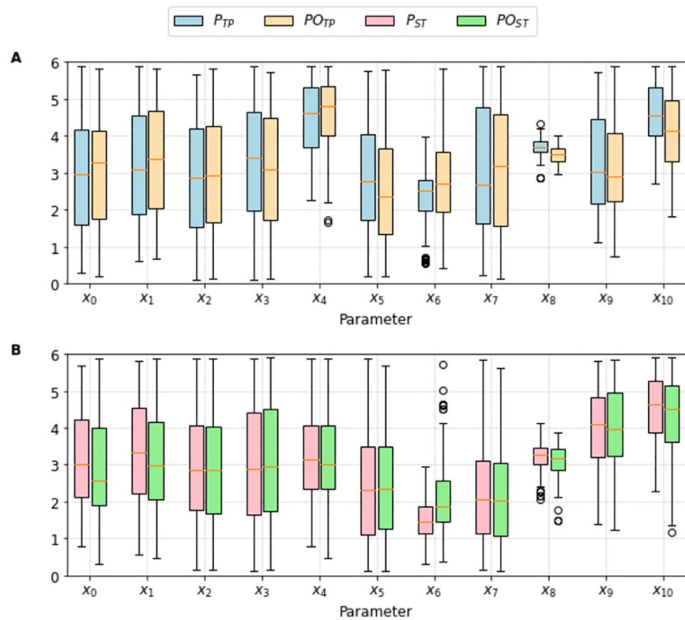


**Fig 13. Parameter ranges of the two populations of solutions  $P$ , and  $PO$ .** Descriptive measures of the values that each fitting parameter assumed among the best feasible solutions for each respective model. The light blue and light orange bars present, respectively, the solutions which compose the populations  $P_{TP}$  and  $PO_{TP}$ . The light red and light green bars present, respectively, the solutions which compose the populations  $P_{ST}$  and  $PO_{ST}$ . A: Descriptive measures obtained for the Ten Tusscher and Panfilov [23] fitting process. B: Descriptive measures obtained for the Stewart et al. [24] fitting process.

<https://doi.org/10.1371/journal.pone.0266233.g013>

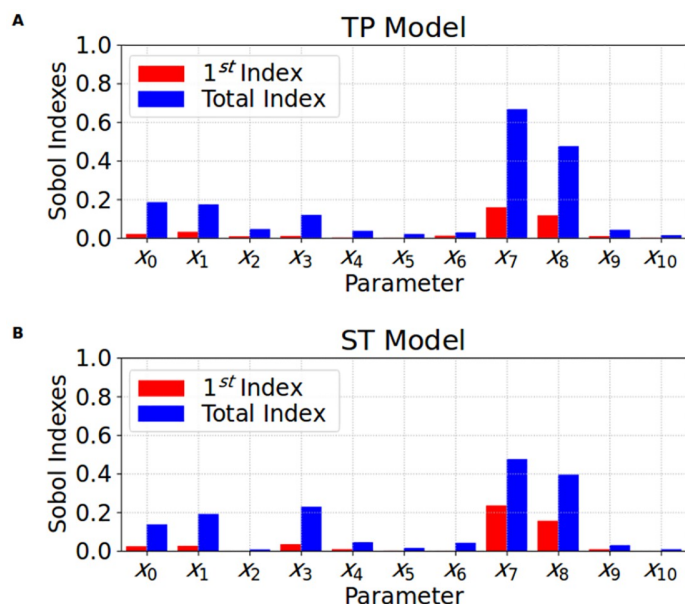


**Fig 14. Sensitivity analysis.** The Sobol 1<sup>st</sup> (red bar), and Total (blue bar) order sensitivity indexes calculated for the 11 fitting parameters ( $x_0$  up to  $x_{10}$ ) when analyzed the influence in the fitness function  $F(x)$ . A: Sensitivity indexes obtained for the Ten Tusscher and Panfilov [23] fitting process. B: Sensitivity indexes obtained for the Stewart et al. [24] fitting process.

<https://doi.org/10.1371/journal.pone.0266233.g014>

formulations has been widespread to simulate Ryanodine Receptors dynamics of different cells and species. However, this approach was not too common for the  $I_{CaL}$  dynamics, particularly with respect to human cardiac models. In this direction, this study presented a new MC-based  $I_{CaL}$  model for two consolidated cardiac models for humans, Ten Tusscher and Panfilov [23], and Stewart et al. [24]. The computational approach employed to generate the MC-based models is based on an Evolutionary and Population-based algorithm. From the fitting results, we check that the newly proposed models, based on the fitting solutions, reproduce the Gate-based original outputs properly. This means that the new MC-based models maintained the original cell scale simulations. Furthermore, using the MC in the  $I_{CaL}$  formulations opens the possibility of simulating subcellular conditions and checking the response of the whole cell and, eventually, cardiac tissue. Using a multi-objective algorithm combined with Uncertainty Quantification analysis may improve our first findings and generate more reliable and consistent models.

Standard electrophysiological models, for example Ten Tusscher and Panfilov [23] and Stewart et al. [24], are usually fitted to a particular set of experiments. The resulting parameter values of such models may not be robust to changes due to a particular pathological condition. To overcome this issue, here we fit a population of Markov Chain-based models that conveniently fit the original experiments within a given tolerance that reflects both model discrepancy and biological variability. We have shown that the same population of solutions encountered by the DE was robust enough to reproduce a new set of experimental data associated with the SCI protocol. One may consider the SCI protocol discussed above as one limit condition and analyze intermediate situations as presented in [38].

Populations of models have been successfully used to represent inter-patient variability of cardiac electrophysiological data [3]. However, it is worth highlighting that the goals and tools used here are different ones. Our main goal is to acknowledge the existence of model discrepancy and identifiability issues, and use higher tolerances after the fitting process to avoid fitting parameters overly precisely, i.e., overfitting. Moreover, the tool used for this was a Differential Evolution algorithm based on evolutionary processes to select a population of parameters that satisfy our error tolerance. It is worth mentioning that considering a sample of best solutions instead of selecting only the best single one does not define a consolidated optimization technique to suppress the overfitting issue. In our study, we did not apply any consolidated technique during the DE process. Instead, we simply selected more solutions than the best one found by the algorithm; then we analyzed how these samples of solutions performed when we applied in a different condition. It is the simplest and computationally cheapest way to avoid one overfitted solution in the possible solutions. Probably, using a consolidated technique such as Early-stopping or Expansion of the set of data [39] in the evolutionary algorithm process will provide more reliable no-overfitted solutions.

One limitation of our method is related to the size of the population of solutions. The choice of the population size was arbitrary but driven by the acknowledgment of model discrepancy [34] and the seek of model generalization. Therefore, we include all solutions with errors below a certain level within the biological variability found in the experiments, 10 – 20%.

For the study presented here, the derived calibrated population was able to replicate new experimental data. The population was calibrated with control data and reproduced different data from pathological conditions (SCI protocol). Nevertheless, the population's average error of some biomarkers (see Table 1) increased from 4–5%, for the control case (or training data), to 20–30%, for the new data (test data). In the case this new level of error is unacceptable, the solution would be to repeat the calibration process including the new data via multi-objective optimization tools, such as those described in [35, 37], and further speedup up the process with emulators as described in [40].

Our method allows us to relate any animal model with a Markov chain of the LCC that can then be fitted to new experimental data with the limitation that possible structural intrinsic differences between the HH Gate-based, used to generate the training and test data, and the MC-based description of the channels can be present. Nevertheless, this difference generates a model discrepancy that is very likely to happen in real-life experimental data. Therefore, we believe this structural difference between the models has positively contributed to the study and further supports our conclusions. It is also important to clarify that the use of our method to link experimental and whole-cell models is restricted to those models where the  $I_{CaL}$  formulation can be arranged as  $I_{CaL} = I_{max} \times O$ , where  $I_{max}$  is the maximum current conductance; and  $O$  represents the portion of the opening fraction of the ionic channels. Besides the TP and ST models, the method can be applied in the models described in [41, 42]. On the other hand, we can not apply the proposed methods in the models presented in [38, 43].

Besides the possibility of directly relating new experimental calcium whole-cell data with a Markov model of the LCC, our method also opens a new line of research where direct links between whole-cell model data and subcellular mechanism can be investigated. It is important to remember that calcium is driven by subcellular interactions at the micron level where LCC and RyR form couplings with different cluster size and important heterogeneity [44]. This means that each coupling will have different probabilistic openings. The relation between the local parameters of the Markov-chain that could reproduce the coupling behavior and the parameters of the single Markov-model found with whole-cell data can now be addressed. Analyzing how a single set of parameters in the Markov-model affects the probabilities of openings depending on cluster size should be the focus of future investigations to entangle how the local release probabilities affect the global calcium cycling of the cell.

In summary, we developed novel Markov Chain models for the L-type Calcium current that reproduced the electrophysiology of two human models for the ventricular and Purkinje cells. In addition, instead of presenting a single model, we presented a population of models based on different solutions found by a robust fitting process. These models could properly reproduce very different protocol data. In particular, we show the importance of using a population of models to obtain proper results when considering a second protocol that mimics the condition of Calmodulin mutations associated with long QT syndrome. The use of populations of solutions was crucial for addressing model discrepancy, identifiability issues, and avoiding fitting parameters overly precisely, i.e., overfitting.

## Supporting information

**S1 Fig. Threshold used for the selection of the individuals.** Representation of the threshold (red dashed line) considered to select the individuals to be part of the population  $P$ , for the respective (A) TP Model, and (B) ST Model. For both models, we selected the best 300 from the 5000 possibilities (or 6% of all the individuals). The worst individual selected to compose the population  $P_{TP}$ ,  $x_{TP}^w$ , obtained  $F(x_{TP}^w) = 15.1\%$ . The worst individual selected to compose the population  $P_{ST}$ ,  $x_{ST}^w$ , obtained  $F(x_{ST}^w) = 16\%$ . The light red area represents the solutions in the rather linear relation. The light blue area represents the solutions in the rather exponential relation.

(TIF)

**S1 Appendix. New Markov chain-based rates.** This appendix introduces the new  $I_{CaL}$  MC-based equations and rates.

(PDF)

**S2 Appendix. Frequency rate robustness.** This appendix presents the outputs of the MC-based versions of the TP and ST models simulated under different pacing rates. (PDF)

**S3 Appendix. Model robustness.** This appendix presents an analysis of robustness the MC-based versions of the TP and ST models. (PDF)

**S1 Data.**

(ZIP)

## Author Contributions

**Conceptualization:** Gustavo Montes Novaes, Enrique Alvarez-Lacalle, Sergio Alonso Muñoz, Rodrigo Weber dos Santos.

**Formal analysis:** Gustavo Montes Novaes, Enrique Alvarez-Lacalle, Sergio Alonso Muñoz, Rodrigo Weber dos Santos.

**Funding acquisition:** Gustavo Montes Novaes, Enrique Alvarez-Lacalle, Sergio Alonso Muñoz, Rodrigo Weber dos Santos.

**Investigation:** Gustavo Montes Novaes, Enrique Alvarez-Lacalle, Sergio Alonso Muñoz, Rodrigo Weber dos Santos.

**Methodology:** Gustavo Montes Novaes, Enrique Alvarez-Lacalle, Sergio Alonso Muñoz, Rodrigo Weber dos Santos.

**Software:** Gustavo Montes Novaes.

**Supervision:** Enrique Alvarez-Lacalle, Sergio Alonso Muñoz, Rodrigo Weber dos Santos.

**Validation:** Gustavo Montes Novaes, Enrique Alvarez-Lacalle, Sergio Alonso Muñoz, Rodrigo Weber dos Santos.

**Writing – original draft:** Gustavo Montes Novaes, Enrique Alvarez-Lacalle, Sergio Alonso Muñoz, Rodrigo Weber dos Santos.

**Writing – review & editing:** Gustavo Montes Novaes, Enrique Alvarez-Lacalle, Sergio Alonso Muñoz, Rodrigo Weber dos Santos.

## References

1. Muszkiewicz A, Britton OJ, Gemmell P, Passini E, Sánchez C, Zhou X, et al. Variability in cardiac electrophysiology: using experimentally-calibrated populations of models to move beyond the single virtual physiological human paradigm. *Progress in biophysics and molecular biology*. 2016; 120(1-3):115–127. <https://doi.org/10.1016/j.pbiomolbio.2015.12.002> PMID: 26701222
2. Clayton R, Bernus O, Cherry E, Dierckx H, Fenton FH, Mirabella L, et al. Models of cardiac tissue electrophysiology: progress, challenges and open questions. *Progress in biophysics and molecular biology*. 2011; 104(1-3):22–48. <https://doi.org/10.1016/j.pbiomolbio.2010.05.008> PMID: 20553746
3. Britton OJ, Bueno-Orovio A, Van Ammel K, Lu HR, Towart R, Gallacher DJ, et al. Experimentally calibrated population of models predicts and explains intersubject variability in cardiac cellular electrophysiology. *Proceedings of the National Academy of Sciences*. 2013; 110(23):E2098–E2105. <https://doi.org/10.1073/pnas.1304382110> PMID: 23690584
4. Groenendaal W, Ortega FA, Kherlopian AR, Zygmunt AC, Krogh-Madsen T, Christini DJ. Cell-specific cardiac electrophysiology models. *PLoS Comput Biol*. 2015; 11(4):e1004242. <https://doi.org/10.1371/journal.pcbi.1004242> PMID: 25928268
5. Colman MA, Saxena P, Kettlewell S, Workman AJ. Description of the human atrial action potential derived from a single, congruent data source: novel computational models for integrated experimental-

- numerical study of atrial arrhythmia mechanisms. *Frontiers in physiology*. 2018; 9:1211. <https://doi.org/10.3389/fphys.2018.01211> PMID: 30245635
- 6. Hove-Madsen L, Llach A, Bayes-Genís A, Roura S, Font ER, Arís A, et al. Atrial fibrillation is associated with increased spontaneous calcium release from the sarcoplasmic reticulum in human atrial myocytes. *Circulation*. 2004; 110(11):1358–1363. <https://doi.org/10.1161/01.CIR.0000141296.59876.87> PMID: 15313939
  - 7. Antzelevitch C, Brugada P, Brugada J, Brugada R. Brugada syndrome: from cell to bedside. *Current problems in cardiology*. 2005; 30(1):9–54. <https://doi.org/10.1016/j.cpcardiol.2004.04.005> PMID: 15627121
  - 8. Saucerman JJ, Healy SN, Belik ME, Puglisi JL, McCulloch AD. Proarrhythmic consequences of a KCNQ1 AKAP-binding domain mutation: computational models of whole cells and heterogeneous tissue. *Circulation research*. 2004; 95(12):1216–1224. <https://doi.org/10.1161/01.RES.0000150055.06226.4e> PMID: 15528464
  - 9. Splawski I, Timothy KW, Decher N, Kumar P, Sachse FB, Beggs AH, et al. Severe arrhythmia disorder caused by cardiac L-type calcium channel mutations. *Proceedings of the National Academy of Sciences*. 2005; 102(23):8089–8096. <https://doi.org/10.1073/pnas.0502506102> PMID: 15863612
  - 10. Yuniarti AR, Setianto F, Marcellinus A, Hwang HJ, Choi SW, Trayanova N, et al. Effect of KCNQ1 G229D mutation on cardiac pumping efficacy and reentrant dynamics in ventricles: computational study. *International journal for numerical methods in biomedical engineering*. 2018; 34(6):e2970. <https://doi.org/10.1002/cnm.2970> PMID: 29488358
  - 11. Wei J, Yao J, Belke D, Guo W, Zhong X, Sun B, et al. Ca<sup>2+</sup>-CaM Dependent Inactivation of RyR2 Underlies Ca<sup>2+</sup> Alternans in Intact Heart. *Circulation Research*. 2021; 128(4):e63–e83. <https://doi.org/10.1161/CIRCRESAHA.120.318429> PMID: 33375811
  - 12. Baddeley D, Jayasinghe ID, Lam L, Rossberger S, Cannell MB, Soeller C. Optical single-channel resolution imaging of the ryanodine receptor distribution in rat cardiac myocytes. *Proceedings of the National Academy of Sciences*. 2009; 106(52):22275–22280. <https://doi.org/10.1073/pnas.0908971106> PMID: 20018773
  - 13. Marchena M, Echebarria B. Computational model of calcium signaling in cardiac atrial cells at the sub-micron scale. *Frontiers in physiology*. 2018; 9:1760. <https://doi.org/10.3389/fphys.2018.01760> PMID: 30618786
  - 14. Colman MA, Holmes M, Whittaker DG, Jayasinghe I, Benson AP. Multi-scale approaches for the simulation of cardiac electrophysiology: I—Sub-cellular and stochastic calcium dynamics from cell to organ. *Methods*. 2020;. PMID: 32126258
  - 15. Qu Z, Liu MB, Nivala M. A unified theory of calcium alternans in ventricular myocytes. *Scientific reports*. 2016; 6(1):1–14. <https://doi.org/10.1038/srep35625> PMID: 27762397
  - 16. Nivala M, Qu Z. Calcium alternans in a couplon network model of ventricular myocytes: role of sarcoplasmic reticulum load. *American Journal of Physiology-Heart and Circulatory Physiology*. 2012; 303(3):H341–H352. <https://doi.org/10.1152/ajpheart.00302.2012> PMID: 22661509
  - 17. Denham NC, Pearman CM, Caldwell JL, Madders GW, Eisner DA, Trafford AW, et al. Calcium in the pathophysiology of atrial fibrillation and heart failure. *Frontiers in physiology*. 2018; 9:1380. <https://doi.org/10.3389/fphys.2018.01380> PMID: 30337881
  - 18. Heijman J, Voigt N, Nattel S, Dobrev D. Cellular and molecular electrophysiology of atrial fibrillation initiation, maintenance, and progression. *Circulation research*. 2014; 114(9):1483–1499. <https://doi.org/10.1161/CIRCRESAHA.114.302226> PMID: 24763466
  - 19. Alvarez-Lacalle E, Echebarria B, Spalding J, Shiferaw Y. Calcium alternans is due to an order-disorder phase transition in cardiac cells. *Physical review letters*. 2015; 114(10):108101. <https://doi.org/10.1103/PhysRevLett.114.108101> PMID: 25815968
  - 20. Stern MD, Ríos E, Maltsev VA. Life and death of a cardiac calcium spark. *Journal of General Physiology*. 2013; 142(3):257–274. <https://doi.org/10.1085/jgp.201311034> PMID: 23980195
  - 21. Shannon TR, Wang F, Puglisi J, Weber C, Bers DM. A mathematical treatment of integrated Ca dynamics within the ventricular myocyte. *Biophysical journal*. 2004; 87(5):3351–3371. <https://doi.org/10.1529/biophysj.104.047449> PMID: 15347581
  - 22. Mahajan A, Shiferaw Y, Sato D, Baher A, Olcese R, Xie LH, et al. A rabbit ventricular action potential model replicating cardiac dynamics at rapid heart rates. *Biophysical journal*. 2008; 94(2):392–410. <https://doi.org/10.1529/biophysj.106.98160> PMID: 18160660
  - 23. Ten Tusscher KH, Panfilov AV. Alternans and spiral breakup in a human ventricular tissue model. *American Journal of Physiology-Heart and Circulatory Physiology*. 2006; 291(3):H1088–H1100. <https://doi.org/10.1152/ajpheart.00109.2006> PMID: 16565318

24. Stewart P, Aslanidi OV, Noble D, Noble PJ, Boyett MR, Zhang H. Mathematical models of the electrical action potential of Purkinje fibre cells. *Philosophical Transactions of the Royal Society A: Mathematical, Physical and Engineering Sciences*. 2009; 367(1896):2225–2255. <https://doi.org/10.1098/rsta.2008.0283> PMID: 19414454
25. Ten Tusscher KH, Noble D, Noble PJ, Panfilov AV. A model for human ventricular tissue. *American Journal of Physiology-Heart and Circulatory Physiology*. 2004; 286(4):H1573–H1589. <https://doi.org/10.1152/ajpheart.00794.2003> PMID: 14656705
26. Hodgkin AL, Huxley AF. A quantitative description of membrane current and its application to conduction and excitation in nerve. *The Journal of physiology*. 1952; 117(4):500–544. <https://doi.org/10.1113/jphysiol.1952.sp004764> PMID: 12991237
27. Biscani F, Izzo D, Jakob W, GiacomoAcciarini, Märtens M, C M, et al. esa/pagmo2: pagmo 2.15.0; 2020. Available from: <https://doi.org/10.5281/zenodo.3738182>.
28. Price, K. Differential evolution. *Handbook Of Optimization*. pp. 187–214 (2013)
29. Bouhlel MA, Hwang JT, Bartoli N, Lafage R, Morlier J, Martins JRRA. A Python surrogate modeling framework with derivatives. *Advances in Engineering Software*. 2019; p. 102662. <https://doi.org/10.1016/j.advengsoft.2019.03.005>
30. Hindmarsh AC, Brown PN, Grant KE, Lee SL, Serban R, Shumaker DE, et al. SUNDIALS: Suite of nonlinear and differential/algebraic equation solvers. *ACM Transactions on Mathematical Software (TOMS)*. 2005; 31(3):363–396. <https://doi.org/10.1145/1089014.1089020>
31. Limpitikul WB, Dick IE, Joshi-Mukherjee R, Overgaard MT, George AL Jr, Yue DT. Calmodulin mutations associated with long QT syndrome prevent inactivation of cardiac L-type Ca<sup>2+</sup> currents and promote proarrhythmic behavior in ventricular myocytes. *Journal of molecular and cellular cardiology*. 2014; 74:115–124. <https://doi.org/10.1016/j.yjmcc.2014.04.022> PMID: 24816216
32. Eck VG, Donders WP, Sturdy J, Feinberg J, Delhaas T, Hellevik LR, et al. A guide to uncertainty quantification and sensitivity analysis for cardiovascular applications. *International journal for numerical methods in biomedical engineering*. 2016; 32(8):e02755. <https://doi.org/10.1002/cnm.2755> PMID: 26475178
33. Feinberg J, Langtangen HP. Chaospy: An open source tool for designing methods of uncertainty quantification. *Journal of Computational Science*. 2015; 11:46–57. <https://doi.org/10.1016/j.jocs.2015.08.008>
34. Lei CL, Ghosh S, Whittaker DG, Aboelkassem Y, Beattie KA, Cantwell CD, et al. Considering discrepancy when calibrating a mechanistic electrophysiology model. *Philosophical Transactions of the Royal Society A*. 2020;this issue. <https://doi.org/10.1098/rsta.2019.0349> PMID: 32448065
35. Pouranbarani E, Berg LA, Oliveira RS, dos Santos RW, Nygren A. Calibration of single-cell model parameters based on membrane resistance improves the accuracy of cardiac tissue simulations. *Journal of Computational Science*. 2021; p. 101375. <https://doi.org/10.1016/j.jocs.2021.101375>
36. Clayton RH, Aboelkassem Y, Cantwell CD, Corrado C, Delhaas T, Huberts W, et al. An audit of uncertainty in multi-scale cardiac electrophysiology models. *Philosophical Transactions of the Royal Society A: Mathematical, Physical and Engineering Sciences*. 2020; 378(2173):20190335. <https://doi.org/10.1098/rsta.2019.0335> PMID: 32448070
37. Pouranbarani E, Weber dos Santos R, Nygren A. A robust multi-objective optimization framework to capture both cellular and intercellular properties in cardiac cellular model tuning: Analyzing different regions of membrane resistance profile in parameter fitting. *PLoS one*. 2019; 14(11):e0225245. <https://doi.org/10.1371/journal.pone.0225245> PMID: 31730631
38. O'Hara T, Virág L, Varró A, Rudy Y. Simulation of the undiseased human cardiac ventricular action potential: model formulation and experimental validation. *PLoS Comput Biol*. 2011; 7(5):e1002061. <https://doi.org/10.1371/journal.pcbi.1002061> PMID: 21637795
39. Ying, X. An overview of overfitting and its solutions. *Journal Of Physics: Conference Series*. 1168, 022022 (2019)
40. Novaes GM, Campos JO, Alvarez-Lacalle E, Muñoz SA, Rocha BM, dos Santos RW. Combining polynomial chaos expansions and genetic algorithm for the coupling of electrophysiological models. In: *International Conference on Computational Science*. Springer; 2019. p. 116–129.
41. Kurata Y., Hisatome I., Imanishi S. & Shibamoto T. Dynamical description of sinoatrial node pacemaking: improved mathematical model for primary pacemaker cell. *American Journal Of Physiology-Heart And Circulatory Physiology*. 283, H2074–H2101 (2002) <https://doi.org/10.1152/ajpheart.00900.2001> PMID: 12384487
42. Hund T. & Rudy Y. Rate dependence and regulation of action potential and calcium transient in a canine cardiac ventricular cell model. *Circulation*. 110, 3168–3174 (2004) <https://doi.org/10.1161/01.CIR.0000147231.69595.D3> PMID: 15505083

43. Shannon T., Wang F., Puglisi J., Weber C. & Bers D. A mathematical treatment of integrated Ca dynamics within the ventricular myocyte. *Biophysical Journal.* 87, 3351–3371 (2004) <https://doi.org/10.1529/biophysj.104.047449> PMID: 15347581
44. Weiss J., Nivala M., Garfinkel A. & Qu Z. Alternans and arrhythmias: from cell to heart. *Circulation Research.* 108, 98–112 (2011) <https://doi.org/10.1161/CIRCRESAHA.110.223586> PMID: 21212392